ADAPTIVE KALMAN FILTERING FOR SMALL SATELLITE ATTITUDE ESTIMATION

BRUNO TUNES DE MELLO

DISSERTAÇÃO DE MESTRADO
EM ENGENHARIA ELÉTRICA

DEPARTAMENTO DE ENGENHARIA ELÉTRICA

FACULDADE DE TECNOLOGIA

UNIVERSIDADE DE BRASÍLIA

Universidade de Brasília
Faculdade de Tecnologia
Departamento de Engenharia Elétrica

Adaptive Kalman Filtering for Small Satellite Attitude Estimation

Bruno Tunes de Mello

DISSERTAÇÃO DE MESTRADO SUBMETIDA AO PROGRAMA DE PÓS-GRADUAÇÃO EM ENGENHARIA ELÉTRICA DA UNIVERSIDADE DE BRASÍLIA COMO PARTE DOS REQUISITOS NECESSÁRIOS PARA A OBTENÇÃO DO GRAU DE MESTRE.

APROVADA POR:

Renato Alves Borges, Dr. (Universidade de Brasília)
(Orientador)

Valdemir Carrara, Dr. (Instituto Nacional de Pesquisas Espaciais)
(Examinador Externo)

Geovany Araújo Borges, Dr. (Universidade de Brasília)
(Examinador Interno)

Brasília/DF, 30 de novembro de 2023.

FICHA CATALOGRÁFICA

TUNES DE MELLO, BRUNO

Adaptive Kalman Filtering for Small Satellite Attitude Estimation. [Brasília/DF] 2023.

xvii, 98p., 210 x 297 mm (ENE/FT/UnB, Mestre, Dissertação de Mestrado, 2023).

Universidade de Brasília, Faculdade de Tecnologia, Departamento de Engenharia Elétrica.

Departamento de Engenharia Elétrica

1. small satellites
2. spacecraft dynamics
3. attitude estimation
4. Kalman filter
5. sensor fusion
6. adaptive Kalman filter

I. ENE/FT/UnB
II. Título (série)

REFERÊNCIA BIBLIOGRÁFICA

TUNES DE MELLO, BRUNO (2023). Adaptive Kalman Filtering for Small Satellite Attitude Estimation. Dissertação de Mestrado, Publicação PPGEE.DM-808/23, Departamento de Engenharia Elétrica, Universidade de Brasília, Brasília, DF, 98p.

CESSÃO DE DIREITOS

AUTOR: Bruno Tunes de Mello

TÍTULO: Adaptive Kalman Filtering for Small Satellite Attitude Estimation.

GRAU: Mestre ANO: 2023

Bruno Tunes de Mello

Universidade de Brasília (UnB)

Campus Darcy Ribeiro

Faculdade de Tecnologia - FT

Departamento de Engenharia Elétrica(ENE)

Brasília - DF CEP 70919-970

To my family and friends that encouraged me during this journey

ACKNOWLEDGEMENTS

First, I thank the Lord for all blessings in my life that allowed me to reach a Master's Degree, for all opportunities to study and work, and for His Grace that sustained me.

I would like to express my sincere gratitude to my family for all the support in my life. My mother, Sueli, for always motivating me to develop myself as a person and as professional, for all sacrifice that made this possible. Also, my sister, Ana Karla, for all advices and talks that encouraged me to keep studying and facing the challenges of life.

To my Advisor, Professor Dr. Renato, I would like to thank for the opportunity in this graduate program, to participate in the AlfaCrux's CubeSat project and for the instructions along this work. I would like to express my gratitude to Dr. Danil Ivanov and Dr. Mikhail Ovchinnikov, both from Keldysh Institute of Applied Mathematics, for the collaboration in the attitude estimation researches in which I could learn important insights used in this work.

I am also thankful to the staff of the Space Operations Center (COPE), in Brasília, which made possible for me to pursue a Master's degree. I would like to thank my friends from COPE for the conversations and good moments that motivated me during this journey. I also wish to thank Emanuel and Matheus from the Laboratory of Simulation and Control of Aerospace Systems (LODESTAR) of UnB for their support in the AlfaCrux's data processing.

I also would like to thank the Brazilian Space Agency (AEB), the National Council for Scientific and Technological Development (CNPq) and the Federal District Research Support Foundation (FAP–DF) that supported and financed the AlfaCrux mission, allowing the University of Brasília (UnB) the conduction and operation of a CubeSat satellite, which allow the development of research in the aerospace field.

ABSTRACT

Due to the technology progress, particularly in electronics the satellite development has become more accessible, allowing its manufacturing by startup companies and universities. Such satellites use low cost components, for general purpose, where one seeks for exchanging a high cost and high reliability platform for a low cost vehicle constellation, less reliable, more advanced technologically and with easy replacement. In this context, an adaptive attitude determination system is an alternative to deal with sensors that have time-varying statistics or they are not completely known. An adaptive ADCS grants more reliability to the platform, increasing its life-cycle and reducing the replacement cost. Taking it as a motivation, the work presents the analysis of algorithms for adapting the filtering method in sensor measurements in the attitude estimation of a small satellite. It is limited to the study of stochastic methods for such goal, as the estimation of the process and observation noise covariance matrices, along with the hypothesis test regarding the fault occurrence and the adaptation of matrices by multiple scale factors. The results obtained show that the adaptation of covariance matrices allows the faulty measurements to be accommodated, reducing their influence in the filter and providing the attitude accuracy preservation for the satellite when comparing with the estimator without the fault detection and isolation mechanism.

Keywords: small satellites; spacecraft dynamics; attitude estimation; Kalman filter; sensor fusion; adaptive Kalman filter.

RESUMO

Título: Filtragem de Kalman Adaptativa para Estimação de Atitude de Pequeno Satélite

Devido à evolução da tecnologia, particularmente a eletrônica, o desenvolvimento de satélites tornou-se mais acessível, permitindo sua construção por empresas *startups* e universidades. Tais satélites utilizam componentes de baixo custo, de uso geral, no qual busca-se trocar uma plataforma de alto custo, e confiabilidade, por uma constelação de veículos de baixo custo, menos confiáveis, mais avançados tecnologicamente, e de fácil reposição. Neste contexto, um sistema de determinação de atitude adaptativo é uma alternativa para lidar com sensores que possuem estatísticas que variam ao longo do tempo ou que não são completamente conhecidas. Um ADCS adaptável garantiria maior confiabilidade à plataforma, aumentando a vida útil e reduzindo o custo de reposição. Tendo isto como motivação, o presente trabalho apresenta a análise de algoritmos para adaptação do método de filtragem em medições de sensores na estimação da atitude de um pequeno satélite. Limita-se ao estudo de métodos estocásticos para tal fim, como a estimação das matrizes de covariância dos ruídos do processo e observação, e a adaptação de tais matrizes por múltiplos fatores de escala. Os resultados obtidos mostram que a adaptação das matrizes de covariância permite acomodar as medidas degradadas, diminuindo a sua influência no filtro e proporcionando a manutenção da precisão da atitude do satélite em relação ao estimador sem mecanismo de adaptação.

Palavras-chave: pequenos satélites; dinâmica de veículos espaciais; estimação de atitude; filtro de Kalman; fusão sensorial; filtro de Kalman adaptativo.

TABLE OF CONTENTS

LIST OF FIGURES

LIST OF TABLES

LIST OF SYMBOLS

$\mathbf{q}$	unit quaternion	-
$\boldsymbol{\varrho}$	quaternion vector part	-
$\mathbf{p}$	Generalized Rodrigues Parameters	-
$\|\cdot\|$	Euclidean norm	-
ϑ	rotation angle	[rad]
$\mathbf{A}_{GF}$	Attitude matrix related to the rotation from frame F to frame G	-
$\tilde{\boldsymbol{\omega}}$	measured angular velocity vector	[rad/s]
$\tilde{\mathbf{B}}$	measured magnetic field vector	[nT]
$\mathbf{B}^{true}$	magnetic field vector computed by IGRF	[nT]
$\hat{\mathbf{x}}$	estimated state vector	-
$\mathbf{X}^k$	Sequence of state vectors $\{\mathbf{x}_0, \mathbf{x}_1, \ldots, \mathbf{x}_k\}$	-
$\tilde{\mathbf{y}}$	sensor observations vector	-
$\hat{\mathbf{y}}$	predicted output or observation vector	-
$\mathbf{Y}^k$	Sequence of observations vectors $\{\mathbf{y}_0, \mathbf{y}_1, \ldots, \mathbf{y}_k\}$	–
$\mathbb{R}^n$	real number vector space of dimension n	–
$\lambda_{M_{Sun}}$	Mean Longitude of the Sun	[°]
M_{Sun}	Mean anomaly of the Sun	[°]
$\lambda_{ecliptic}$	Ecliptic longitude of the Sun	[°]
ε	Ecliptic of the Sun	[°]
T_{UT1}	Julian centuries	[centuries]

JD_{UT1}	Julian date	[days]
$\mathbf{S}_{ECI}$	Sun direction unit vector in ECI	[−]
ϕ_g	Latitude of a surface cell center point	[°]
θ_g	Longitude of a surface cell center point	[°]
$\rho(\phi_g, \theta_g)$	Reflectivity index as function of the latitude and longitude	[-]
$\rho(\phi_g, \theta_g)$	Earth surface cell area as function of the latitude	[-]
E_{AM0}	Solar intensity at air mass zero	[W/m^2]
$E_c(\phi_g, \theta_g)$	Solar radiation reflected by a surface cell	[W/m^2]
$\mathbf{P}_k^-$	Predicted State error covariance matrix at time instant k	–
$\mathbf{P}_k^+$	State error covariance matrix at time instant k	–
$\mathbf{Q}_k$	Process error covariance matrix at time instant k	–
$\mathbf{R}_k$	Observation error covariance matrix at time instant k	–
$\boldsymbol{\upsilon}_k$	innovation vector at time instant k	–
$\mathbf{P}_k^{yy}$	Output covariance matrix at time instant k	–
$\mathbf{P}_k^{\upsilon\upsilon}$	Innovation covariance matrix at time instant k	–
$\mathbf{P}_k^{xy}$	State-output cross-covariance matrix at time instant k	–
$\omega_\oplus$	Earth's rotation angular velocity	[rad/s]
ω_o	Orbital angular velocity	[rad/s]

GLOSSARY

ADCS	Attitude Determination and Control System
AEB	Brazilian Space Agency, in portuguese
AKF	Adaptive Kalman Filtering
AU	Astronomic Unit
CM	Covariance Matching
COTS	Commercial off-the-shelf
CSS	Coarse Sun Sensor
ECEF	Earth Centered Earth-Fixed Frame
ECI	Earth Centered Inertial Frame
EOP	Earth Orientation Parameters
EKF	Extended Kalman Filter
FDIR	Failure Detection, Isolation and Recovery
GMST	Greenwich Mean Sideral Time
GRP	Generalized Rodrigues Parameters
IGRF	International Geomagnetic Reference Field
KF	Kalman Filter
LEO	Low Earth Orbit
LOD	Length of Day
LODESTAR	Laboratório de Simulação e Controle de Sistemas Aeroespaciais
LVLH	Local-Vertical Local-Horizontal

MEKF	Multiplicative Extended Kalman Filter
MEMS	Micro-Electro-Mechanical Systems
MMSE	Minimum Mean Square Error
MRP	Modified Rodrigues Parameters
p.d.f	Probability Density Function
rms	Root Mean Squared
SGP4	Simplified General Perturbations Model 4
Smallsat	Small Satellite
TLE	Two-line Elements
UKF	Unscented Kalman Filter
UnB	University of Brasília
USQUE	Unscented Quaternion Estimator
UT	Unscented Transform

CHAPTER 1

INTRODUCTION

1.1 CONTEXTUALIZATION

The rapid growth of electronic systems technologies, specifically the consumer electronics devices, allowed the development of spacecrafts and instruments by universities and research institutions. Furthermore, the evolution of space launch vehicles provided the reduction of the cost related to such services and the access to space, once restricted to government organizations and large corporations, now became affordable for innovative business (WESTON; YOST, 2023).

Small satellites (smallsat) has became one drive factor of the called *New Space*, which is a paradigm defined by the vast commercialization of space services by start-up companies, technology innovation and short development cycles. Currently, such spacecrafts are used by emerging business for optical and synthetic aperture radar (SAR), remote sensing imagery acquisition, telecommunications, radiofrequency-based geolocation and even deep-space missions. The low-cost and fast manufacturing also allowed the implementation of satellite constellations, with hundred of platforms covering the Earth and providing services with high quality and availability.

The traditional space market is characterized by highly reliable vehicles designed in a long development cycle, in complex verification and validation (V&V) architecture, using legacy technologies, with redundant subsystems and specific devices for space environments, in order to reduce the risk of failure. All those aspects generates high-cost missions in which only governments and big companies were able to implement.

In contrast, small satellites utilizes components with less rigorous process of manufacturing and certification for space applications. Such vehicles rely on miniaturized technologies, as the Micro-Electro-Mechanical Systems (MEMS) sensors. In educational and scientific missions,

commercial off-the-shelf (COTS) devices can be considered in the satellite design which may increases the risk of failure. Besides, cutting-edge technologies are also used in spacecrafts for research applications. Table 1.1 presents the spacecraft classification by weight and the categories which are considered small satellites.

Table 1.1. Satellite classification by weight.

	Class name	**Weight range (kg)**
	Large	≥ 1000
	Medium	$500 - 1000$
Smallsats	Mini	100 - 500
	Micro	10 - 100
	Nano	1 - 10
	Pico	0.1 - 1
	Femto	< 0.1

An important class of smallsat is the CubeSat standard which was created for universities and colleges educational programs to provide training in the field of space sciences and technologies. Such standard specifies platform of sizes multiple of 1U ($10 \times 10 \times 10$ cm) and the possible configurations are shown in Table 1.2. CubeSats are also adopted for science missions and experiments, technology demonstrations and even commercial applications.

Table 1.2. Cubesats size.

Cubesat configuration	**Dimensions (cm)**	**Maximum Weight(kg)**
1U	10×10×10	2.00
3U	10×10×30	6.00
6U	20×10×30	12.00
12U	20×20×30	24.00

Within this scenario, Brazil, as a country of vast extensions, has an increasing demand and potential opportunities in the space market. Applications such as communications for remote areas, remote sensing towards to environment and natural resources monitoring, surveillance and weather research can bring economics and social benefits along with the technological development. This range of applications and the pursue for the aerospace industry's growth have promoted Cubesat missions initiatives by Brazilian educational and research institutions.

One of the most recent missions is the AlfaCrux CubeSat, launched in 2022 as a project of the University of Brasília (UnB) for radio amateur and educational purposes, where the

learning was focused in project management, risk analysis and space operations (BORGES *et al.*, 2022).

1.2 MOTIVATION

Attitude Determination and Control Systems (ADCS) perform a very important role in spacecraft navigation, once the satellite orientation is substantial for both the mission and the safe operation. The ADCS enables the pointing of antennas and cameras to the desired position, also providing means to rotates the solar panels direction for electrical energy generation. The system performance will depend on the sensor's quality and the estimation algorithm design. Figure 1.1 shows the block diagram of a typical ADCS components in which the attitude estimation problem is represented by the feedback flow.

Figure 1.1. Attitude Determination and Control System.

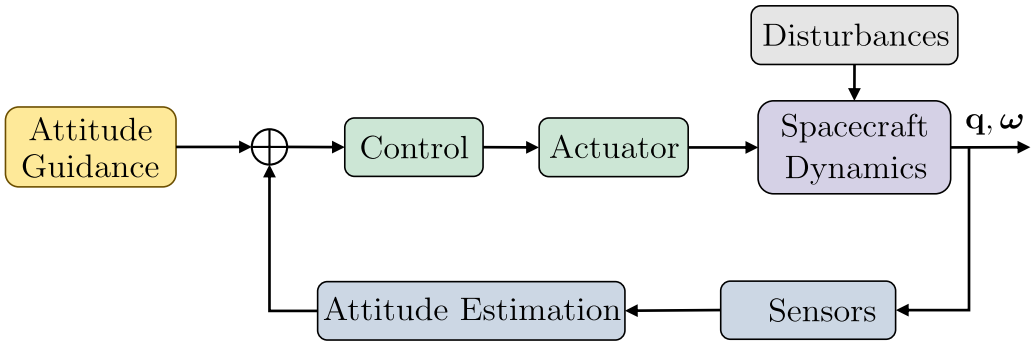

Source: Author.

In inertial navigation the sensors can be divided in grades according to their measurement accuracy, stability and noise levels. Space-grade and military-grade components have high reliability level, but the cost is also high. The automotive-grade and industrial-grade elements have a moderate reliability level enough to work in harsh environments. Small satellites commonly use low-cost components, like the ones for general-purpose market which are the COTS products.

In this conception, the small satellite manufacturers seek to change high-cost and reliable platforms for reduced cost, less reliable spacecraft constellations, but more advanced technologically with fast replacement. Therefore, the use of techniques that mitigates the system failure

risk is fundamental for the mission success.

For that reason, a fault-tolerant attitude determination system is an approach for the detection of sensor measurements faults and adaptation mean against induced errors. A robust and adaptive ADCS will grant more reliability to the satellite, increasing the lifespan and reducing the replacement cost. Also, the fault tolerance feature will improve the mission availability and the products delivery.

1.3 LITERATURE REVIEW

The attitude estimation is an important research field concerning space vehicles design and a problem that draw attention of others areas that work with navigation, as robotics, and the fusion of inertial and Global Navigation Satellite System (GNSS). Currently, with the advent of small satellites, the development of spacecraft ADCS had reached the universities and the academy, where thousands of vehicles were launched until now (WESTON; YOST, 2023).

In the beginning of the space exploration, attitude determination systems were based on static or deterministic methods (MARKLEY; CRASSIDIS, 2014). However, algorithms which consider the stochastic nature of the measurements are the most used today due to their performance. In this approach, the Kalman filtering is the main technique for vehicles pose estimation and the study of new variations are in the recent advances in technology.

The commonly used methods for small satellites are the Extended Kalman Filter (EKF) and the Unscented Kalman Filter (UKF) (CRASSIDIS *et al.*, 2007). In Ivanov *et al.* (2015) a study of attitude determination algorithms using the EKF is presented, where a series different sensors set and state vectors were compared in terms of estimation accuracy. Esit *et al.* (2021) presented several filtering configurations, such as the dynamics-based and gyro-based process model, in the EKF and UKF filters also with integration of the static method Quaternion Estimator (QUEST) algorithm.

Ovchinnikov & Ivanov (2014) presented a performance analysis of the EKF using a magnetometer and Sun sensors. The asymptotic estimated error is derived in a analytical approach for a quasi-stationary motion. Soken & Hacizade (2019) discuss the problem of Kalman filter tuning, where the empirical and adaptive approaches are used in the noise covariance matrices

values in order to improve the filter accuracy.

In Battistini *et al.* (2016) a variation of the UKF is used for the attitude reconstruction of a small satellite and its performance is proved through an onboard camera imaging the Earth. Also about the attitude reconstruction problem, Ivanov *et al.* (2021) considered a magnetometer-only and dynamics-based EKF for the sensor bias estimation and rotational motion analysis. The initial state is found through a least squares problem.

Soken & Sakai (2020) used the Triaxial Attitude Determination (TRIAD) algorithm for a coarse orientation acquisition and the UKF for a fine attitude estimation and magnetometer calibration with the aid of a gyroscope. When the parameters meet the steady-state, a UKF is executed just for the attitude estimation. A statistical test is applied to verify if a change occurred on the parameters, so the parameter estimation is run again. Chagas *et al.* (2021) applied the EKF to calibrate attitude sensors considering the presence of bias, misalignment and non-orthogonality. It showed that the attitude estimation accuracy is improved with the calibration process.

One approach for attitude estimation is the particle filtering which considers the propagation of several state vector samples under different assumptions (CHENG; CRASSIDIS, 2004). In Silva *et al.* (2022) a Rao-Blackwellized particle filtering is used for attitude and gyroscope bias estimation, where this method reduces the number of particles and keep the re-sampling consistent. Garcia *et al.* (2019) evaluates the EKF, UKF and the Cubature Kalman Filter with real sensors data and compare each approach performance.

Mesquita *et al.* (2017) applies the State-Dependent Riccati Equation (SDRE) for a Cubesat attitude estimation problem, in which the system is linearized through matrices of state-dependent coefficient. Besides the spacecraft, in (GUIMARãES *et al.*, 2017) the EKF is used for the pose estimation of a testbed platform intended for attitude determination and control experiments of nano-satellites.

1.3.1 Adaptive Attitude Estimation

Due to the reliability issue concerning the attitude sensors in small satellites, which are low-cost sensors in general, the adaptive Kalman filtering is solution to deal with external

disturbances, time-varying parameters and faulty measurements (HAJIYEV; SOKEN, 2020). This approach allow the noise covariance matrices to be estimated in order to keep the filter capabilities.

In Hajiyev *et al.* (2019) a Singular Value Decomposition (SVD)- aided UFK is used for attitude estimation. Also, both process and measurement noise covariance matrices are adapted simultaneously while noise increment and bias were added to the sensors measurements. Soken & Sakai (2015) used the adaptation in the process noise covariance matrix in order to improve the UKF performance for attitude and sensor biases estimation.

(CHIELLA *et al.*, 2019) proposed a robust adaptive UKF which is able to estimate the attitude of a robotic manipulator in the presence of fast and slow variations of external perturbation. The algorithm contains an outlier detection scheme which provides an abrupt disturbance change rejection. In the work of Soken & Hajiyev (2014) a robust EKF and a robust UKF are compared in situations of sensor measurement faults, where both filters are adaptive and have the capability of fault detection.

(NARASIMHAPPA *et al.*, 2020) developed a robust version of the Sage-Husa Adaptive Kalman Filter for the drift minimization in a Inertial Measurement Unit (IMU). The work showed that the algorithm deal with time-varying noise of a MEMS gyroscope and accelerometer, also the uncertainty in the measurements. In Cilden-Guler *et al.* (2019) several adaptive Kalman filters configurations were compared in a system with a magnetometer heavy-tailed noise and sensor fault.

1.4 OBJECTIVE

The main objective of this work is to provide a detailed analysis of attitude estimation algorithms that can provide robustness against sensor failures for small satellite applications. For that, adaptive Kalman filter are used in the sensor fusion and stochastic methods are applied for the measurement fault detection and isolation.

1.5 CONTRIBUTIONS

This work concerns the attitude estimation of small satellites with a sensor fault tolerant technique in order to the spacecraft to become more robust and reliable. Furthermore, the proposed approach combines physics-based and data-driven models, numerical simulations, sensor updates, and historical data. Two case studies are considered, a numerical one for comparison and validation of the methods, and a real application to the AlfaCrux CubeSat. The environment models concerning the spacecraft dynamics were implemented and will be used in the Laboratório de Simulação e Controle de Sistemas Aeroespaciais (LODESTAR), UnB, for the AlfaCrux mission control platform and future missions simulations.

Regarding the academic production, the following articles were published:

- MELLO, B. T. de; BORGES, R. A.; BATTISTINI, S. Attitude reconstruction of the AlfaCrux CubeSat using onboard sensors and solar panels in-orbit data. In: *Proceedings of the Joint 5th IAA Latin American CubeSat Workshop and 3rd IAA Latin American Symposium on Small Satellites*. [S.l.]: International Adademy of Astronautics, 2022.

- BORGES, R. A.; SANTOS, A. C. dos; SILVA, W. R.; AGUAYO, L.; BORGES, G. A.; KARAM, M. M.; SOUSA, R. B. de; GARCíA, B. F.-A.; BOTELHO, V. M. de S.; FERNáNDEZ-CARRILLO, J. M.; AGRA, J. M. L.; AGELET, F. A.; BORGES, J. V. Q. S.; OLIVEIRA, A. C. A. de; MELLO, B. T. de; AVELINO, Y. da C. F.; MODESTO, V. F.; BRENAG, E. C. The AlfaCrux CubeSat mission description and early results. *Applied Sciences*, v. 12, p. 9764, 9 2022. ISSN 2076-3417.

- BRENAG, E. C.; MELLO, B. T. de; ARRUDA, M. L.; BORGES, R. A.; IVANOV, D.; MONAKHOVA, U.; MASHTAKOV, Y.; OVCHINNIKOV, M. Magnetic parameters estimation and attitude motion reconstruction using in-flight magnetometer measurements of the AlfaCrux CubeSat. In: *Proceedings of the Joint 5th IAA Latin American CubeSat Workshop and 3rd IAA Latin American Symposium on Small Satellites*. [S.l.]: International Academy of Astronautics, 2022.

- BRENAG, E. C.; ARRUDA, M. L.; MELLO, B. T. de; BORGES, R. A.; OVCHINNIKOV, M.; IVANOV, D. AlfaCrux CubeSat magnetic dipole determination and atti-

tude motion estimation using magnetometer measurements only. In: *Proceedings of the 74th International Astronautical Congress*. [S.l.]: International Astronautical Federation (IAF), 2023.

1.6 WORK STRUCTURE

The work is organized as the following structure:

- In the Chapter 2, the fundamentals of space related mathematical models are presented. The concepts of rigid-body kinematics and dynamics are discussed along with the sensors and environment models.
- The Chapter 3 presents the theoretical formulation of the Kalman filtering and state estimation, also with its application in sensor fusion towards attitude estimation for spacecrafts.
- In the Chapter 4, sensor faults detection methods are discussed and measurement anomalies accommodation techniques in state estimation are presented. The covariance matching approach is explained and its application to the noise covariance matrix adaptation is developed.
- In the Chapter 5, the main results and computational simulations are presented discussed. All parameters and implementation details are presented along with the technologies used.
- The Chapter 6 presents the conclusions obtained from the simulation analysis and the result performance, along with the proposal of future works.

CHAPTER 2

SPACECRAFT ATTITUDE DYNAMICS

This chapter presents the mathematical models involved in the spacecraft dynamics and control analysis. First, the coordinate systems used in space navigation are defined. Then, the attitude representations and the rotational motion of satellites are discussed. Next, the models related to the space environment are explained and the sensor models accounted for the filtering problem are presented.

2.1 COORDINATE FRAMES

For the study and analysis of vehicles navigation in the physical three-dimensional space, the associated vector quantities must be described in reference coordinates systems. Such vectors considered in this work are described in four different reference frames common to the spaceflight dynamics.

2.1.1 Earth-Centered Inertial Frame (ECI)

The inertial frame is considered fixed with respect to distant stars, but its axes moves slightly over time. The system's origin is located in the Earth's center (geocentric), the x axis points towards the vernal equinox, the y axis lies in the equatorial plane and the z axis points toward the North pole (MARKLEY; CRASSIDIS, 2014; VALLADO; WERTZ, 2013). The frame is called Earth-Centered Inertial Frame (ECI) and it is shown in Figure 2.1.

Figure 2.1. Inertial and orbital frames.

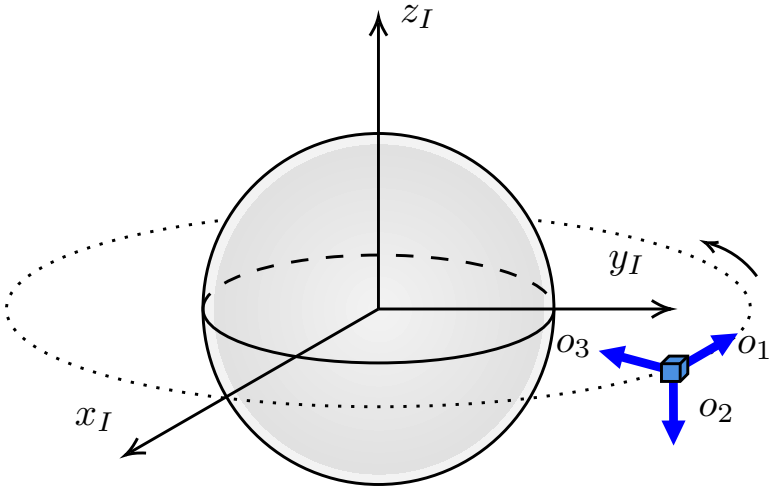

Source: Author.

The ECI frame is commonly used in spacecraft orbit propagation models and also in celestial bodies position calculation, as in the Sun model.

2.1.2 Earth-Centered Earth-Fixed Frame (ECEF)

The Earth-Centered Earth-Fixed Frame (ECEF) is a geocentric equatorial reference system which rotates with the Earth, unlike the ECI frame. In this frame one axis points towards the Greenwich meridian direction, the second axis is perpendicular to the first and the last points towards to the North Pole (VALLADO; WERTZ, 2013).

The Earth rotation motion has the effects of precession and nutation. First, for the coordinates conversion, one needs to account the Greenwich Mean Sidereal Time (GMST) as a reference of the Earth's rotation. The relation between ECI and ECEF frames is given by the rotation matrix as(VALLADO; WERTZ, 2013)

$$R(\theta_{GAST1982}) = \begin{bmatrix} \cos\theta_{GAST1982} & \sin\theta_{GAST1982} & 0 \\ -\sin\theta_{GAST1982} & \cos\theta_{GAST1982} & 0 \\ 0 & 0 & 1 \end{bmatrix}, \tag{2.1}$$

in which $\theta_{GAST1982}$ is the Greenwich angle defined as

$$\theta_{GAST1982} = \theta_{GSMT1982} + Eq_{equinox1982}, \tag{2.2}$$

with $\theta_{GSMT1982}$ computed by

$$\begin{aligned}\theta_{GSMT1982} =& 67{,}310.54841^s + (876{,}600^h + 8{,}640{,}184.812866^s)T_{UT1} \\ &+ 0.093104T_{UT1}^2 - 6.2 \times 10^{-6}T_{UT1}^3,\end{aligned} \tag{2.3}$$

and the Equinox determined by

$$Eq_{equinox1982} = \Delta\Psi_{1980}\cos(\bar{\epsilon}_{1980}) + 0.00264''\cos(\Omega_{Moon}) + 0.000063''\sin(2\Omega_{Moon}). \tag{2.4}$$

In the previous equation, $\Delta\Psi_{1980}$ is the nutation of the longitude and $\bar{\epsilon}_{1980}$ is the obliquity of the ecliptic central angle. For simplicity, such terms can be neglected once $\Delta\Psi_{1980} \approx 0$. In addition, Ω_{Moon} is the Moon longitude defined as

$$\Omega_{Moon} = 125.04452222^\circ + (-6962890.5390''T_{TT} + 7.455''T_{TT}^2 + 0.008''T_{TT}^3)/3600''. \tag{2.5}$$

Besides the aforementioned phenomena, in order to get a more precise spacecraft position, the Earth's polar motion must be accounted as given by

$$W = \begin{bmatrix} \cos x_p \cos s' & -\cos y_p \sin s' + \sin y_p \sin x_p \cos s' & -\sin y_p \sin s' - \cos y_p \sin x_p \cos s' \\ \cos x_p \sin s' & \cos y_p \cos s' + \sin y_p \sin x_p \sin s' & \sin y_p \cos s' - \cos y_p \sin x_p \sin s' \\ \sin x_p & -\sin y_p \cos x_p & \cos y_p \cos x_p \end{bmatrix}, \tag{2.6}$$

in which x_p and y_p are the Earth's pole axis displacement and s' is a correction term given by $s' = -0.000047''T_{TT}$ in which T_{TT} is the Terrestrial Time obtained as the sum of $UT1$ and the Lenght of Day (LOD) (VALLADO; WERTZ, 2013).

Finally, the coordinates conversion is defined by

$$\mathbf{r}_E = W^T(x_p, y_p, LOD)R^T(\theta_{GSMT1982})\mathbf{r}_I. \tag{2.7}$$

The polar motion and the LOD data are part of the Earth Orientation Parameters (EOP). The values of such parameters can be retrieved from the United States Naval Observatory (USNO) or the International Earth Rotation and Reference Systems Service (IERS).

Due to the fact that the ECEF rotates with the Earth, the position vector can be specified also as the radial distance, longitude and latitude, that is, a point with coordinates (x_E, y_E, z_E) can be described also in terms of geodetic coordinates according to a set of conversion equations, as described in Markley & Crassidis (2014).

2.1.3 Orbital Local-Vertical/Local-Horizontal Frame (LVLH)

The orbital frame is dependent of the satellite position in the orbit trajectory and allows vectors to be described in relation to the orbit plane (MARKLEY; CRASSIDIS, 2014). This frame is centered in the spacecraft center-of-mass, with components in radial direction, normal to the orbital plane and tangential to the trajectory, which results in the Local Vertical Local Horizontal Frame (LVLH). Figure 2.1 shows the orbital frame.

The third orthonormal vector is the radial component, defined as

$$\mathbf{o}_{3I} = -\frac{\mathbf{r}_I}{\|\mathbf{r}_I\|}, \tag{2.8}$$

in which $\mathbf{r}_I$ is the spacecraft center-of-mass position in the ECI frame. The second vector has its direction normal to the orbital plane, that is

$$\mathbf{o}_{2I} = -\frac{\mathbf{r}_I \times \mathbf{v}_I}{\|\mathbf{r}_I \times \mathbf{v}_I\|}, \tag{2.9}$$

in which $\mathbf{v}_I$ as the spacecraft velocity in the ECI frame. The first vector form an orthonormal basis, which is

$$\mathbf{o}_{1I} = \mathbf{o}_{2I} \times \mathbf{o}_{3I}. \tag{2.10}$$

The attitude matrix which transforms a vector from the LVLH frame to the ECI is given by

$$A_{IO} = \begin{bmatrix} \mathbf{o}_{1I} & \mathbf{o}_{2I} & \mathbf{o}_{3I} \end{bmatrix}. \tag{2.11}$$

The LVLH frame is important for Earth pointing spacecrafts once it allows the computing of off-nadir angles and the line-of-sight direction to determined ground positions (MARKLEY; CRASSIDIS, 2014).

2.1.4 Spacecraft Body Frame

The spacecraft body frame has its origin in the vehicle center-of-mass and its basis vectors are the structure axes. This reference frame is important for the subsystems assembly and also for the inertial matrix determination. Figure 2.2 illustrates the reference system.

Figure 2.2. Spacecraft body frame.

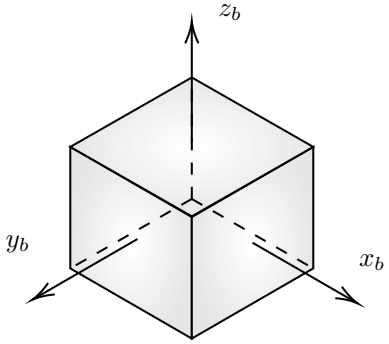

Source: Author.

Components such as thrusters, solar panels, antennas and the payload are mounted following the spacecraft body frame axes in order to work properly. Besides, the attitude control system considers this frame for the spacecraft pointing.

2.2 ATTITUDE REPRESENTATIONS

The space vehicle orientation at any time instant can be represented by a set of parameters. There are several attitude representation parameters in which some of them have singularities and others have constrains (SHUSTER, 1993; MARKLEY; CRASSIDIS, 2014). In this work, the most common parameters set used for the mathematical models are presented next.

2.2.1 Euler Axis/Angle

The Euler's Rotation Theorem (MARKLEY; CRASSIDIS, 2014) states that any rotation can be represented by an axis of rotation given by an unit vector and an angle value (MARKLEY; CRASSIDIS, 2014). That is, an arbitrary rotational motion is equivalent to a rotation about an axis $\mathbf{e} \in \mathbb{R}^3$ by an angle ϑ and it can be represented as a rotation vector by

$$\boldsymbol{\vartheta} = \mathbf{e}\vartheta. \tag{2.12}$$

Although the Euler axis/angle is not used in dynamics systems modeling, others representations can be related to presented definition.

2.2.2 Quaternions

For the filtering problem, a common used representation is the quaternion $\mathbf{q}$, an extension of the complex number described by four components where the first three ones constitutes a vector and the last one is a scalar (CRASSIDIS *et al.*, 2007). The quaternion formulation is given by

$$\mathbf{q} = \begin{bmatrix} \mathbf{e}sin(\vartheta/2) \\ cos(\vartheta/2) \end{bmatrix} = \begin{bmatrix} \boldsymbol{\varrho} \\ q_4 \end{bmatrix} = \begin{bmatrix} q_1 & q_2 & q_3 & q_4 \end{bmatrix}^T, \tag{2.13}$$

in which $\mathbf{e}$ is the rotation vector, ϑ is the rotation angle and q_i, $i = 1, \ldots 4$ are the four components. Also, $\boldsymbol{\varrho}$ is the vector part of the quaternion.

An advantage of these parameters is that the only constraint regarding the quaternion attitude representation is the unit norm, that is

$$\mathbf{q}^T\mathbf{q} = 1. \tag{2.14}$$

The unit norm quaternion has no singularity region and the rotational motion equations have a close form (SHUSTER, 1993). Furthermore, a rotation can be described as a sequence of rotations through the quaternion multiplication operation as

$$\mathbf{q} = \bar{\mathbf{q}} \otimes \breve{\mathbf{q}}, \tag{2.15}$$

in which $\mathbf{q}$ is the resulting quaternion, $\breve{\mathbf{q}}$ is the first rotation quaternion and $\bar{\mathbf{q}}$ represents the second rotation. The multiplication between two quaternions is defined as (MARKLEY; CRASSIDIS, 2014)

$$\bar{\mathbf{q}} \otimes \mathbf{q} = \begin{bmatrix} q_4\bar{\boldsymbol{\varrho}} + \bar{q}_4\boldsymbol{\varrho} - \bar{\boldsymbol{\varrho}} \times \boldsymbol{\varrho} \\ \bar{q}_4 q_4 - \bar{\boldsymbol{\varrho}} \cdot \boldsymbol{\varrho} \end{bmatrix}. \tag{2.16}$$

Finally, the attitude matrix is computed from the quaternion using the following relation

$$A(\mathbf{q}) = (q_4^2 - \|\boldsymbol{\varrho}\|^2)\mathbf{I}_{3\times 3} - 2q_4\left[\boldsymbol{\varrho}\times\right] + 2\boldsymbol{\varrho}\boldsymbol{\varrho}^T, \tag{2.17}$$

in which $[\boldsymbol{\varrho}\times]$ is the skew-symmetric matrix from the cross-product (MARKLEY; CRASSIDIS, 2014).

2.2.3 Generalized Rodrigues Parameters

Besides the quaternion, another parameterization that will be considered in the filtering problem is the called Generalized Rodrigues Parameters (GRP) (SCHAUB; JUNKINS, 1996),

$\mathbf{p} \in \mathbb{R}^3$, a three-component vector related to the quaternion by

$$\mathbf{p} = f\frac{\boldsymbol{\varrho}}{(a+q_4)}, \tag{2.18}$$

in which f and a are scalars that can be arbitrarily chosen. Attitude parameters express the satellite orientation in one frame with respect to a reference system.

For $f = 1$ and $a = 0$, the representation is called Gibbs vector, considered another set of parameters and denoted by $\mathbf{g}$. When $f = 1$ and $a = 1$ then one gets the Modified Rodrigues Parameters (MRPs), which is also another representation (SHUSTER, 1993). Finally, when $f = 2(a+1)$ the GRP is approximately equivalent to the rotation angle for small rotations (CRASSIDIS; MARKLEY, 2003).

2.2.4 Euler Angles

Let two reference frames, $\mathcal{F}$ and $\mathcal{G}$, both defined in the three-dimensional Euclidean space. Any rotation between such frames can be decomposed into a sequence of rotations along three orthogonal directions, that is, a orthonormal basis $\{\mathbf{e}_1, \mathbf{e}_2, \mathbf{e}_3\}$ (MARKLEY; CRASSIDIS, 2014). The attitude matrices that describe the rotation along each direction are

$$A_1(\alpha) = \begin{bmatrix} 1 & 0 & 0 \\ 0 & \cos\alpha & -\sin\alpha \\ 0 & \sin\alpha & \cos\alpha \end{bmatrix}, \; A_2(\alpha) = \begin{bmatrix} \cos\alpha & 0 & \sin\alpha \\ 0 & 1 & 0 \\ -\sin\alpha & 0 & \cos\alpha \end{bmatrix}, \; A_3(\alpha) = \begin{bmatrix} \cos\alpha & \sin\alpha & 0 \\ -\sin\alpha & \cos\alpha & 0 \\ 0 & 0 & 1 \end{bmatrix}.$$

Markley & Crassidis (2014) states that for spacecraft attitude analysis, the $3-2-1$ sequence is commonly used. Defining three rotation angles ϕ, θ and ψ, a rotation can be described as

$$A_{321}(\phi, \theta, \psi) = A_1(\psi)A_2(\theta)A_3(\phi). \tag{2.19}$$

Such angles are also called *roll*, *pitch* and *yaw*, for asymmetric sequences and this terminology is used for rotations specified in vehicles' body frame (MARKLEY; CRASSIDIS, 2014).

2.3 RIGID-BODY KINEMATICS EQUATION

Given a rigid body with rotational motion in the physical (three-dimensional) space, the kinematics of the body's attitude parameterized in quaternions is given by

$$\dot{\mathbf{q}}(t) = \frac{1}{2}\Xi[\mathbf{q}(t)]\boldsymbol{\omega}(t) = \frac{1}{2}\Omega(\boldsymbol{\omega}(t))\mathbf{q}(t), \tag{2.20}$$

where $\boldsymbol{\omega}(t) \in \mathbb{R}^3$ is a vector composed by the angular velocity in each dimension with

$$\Xi(\mathbf{q}) = \begin{bmatrix} q_4 I_{3\times 3} + [\boldsymbol{\varrho}\times] \\ -\boldsymbol{\varrho}^T \end{bmatrix}, \tag{2.21}$$

and

$$\Omega(\boldsymbol{\omega}) = [\boldsymbol{\omega}\otimes] = \begin{bmatrix} -[\boldsymbol{\omega}\times] & \boldsymbol{\omega} \\ -\boldsymbol{\omega}^T & 0 \end{bmatrix}, \tag{2.22}$$

in which $[\boldsymbol{\varrho}\times]$ represents the cross-product matrix of $\boldsymbol{\varrho}$, defined for any three-dimensional vector by

$$[\mathbf{x}\times] \equiv \begin{bmatrix} 0 & -x_3 & x_2 \\ x_3 & 0 & -x_1 \\ -x_2 & x_1 & 0 \end{bmatrix}. \tag{2.23}$$

2.4 RIGID-BODY DYNAMICS EQUATION

The dynamics equation considers the torques acting over the rigid body that produce the motion described by the kinematics equation. For the spacecraft rotational motion, the equation is as follows (MARKLEY; CRASSIDIS, 2014)

$$\mathbf{J}\dot{\boldsymbol{\omega}} + \boldsymbol{\omega} \times (\mathbf{J}\boldsymbol{\omega}) = \mathbf{T}_{\boldsymbol{net}}, \tag{2.24}$$

where $\mathbf{T}_{net}$ is the sum of all torques acting over the body, which are divided as

$$\mathbf{T}_{net} = \mathbf{T}_{ctrl} + \mathbf{T}_{dist}, \tag{2.25}$$

with $\mathbf{T}_{ctrl}$ as the control torque generated by internal devices, such as magnetorquers and reaction wheels, and $\mathbf{T}_{dist}$ is the disturbance torques from the environment (MARKLEY; CRASSIDIS, 2014). And the term $\mathbf{J}$ is the spacecraft inertia tensor given by

$$\mathbf{J} = \begin{bmatrix} I_{xx} & -I_{xy} & -I_{xz} \\ -I_{yx} & I_{yy} & -I_{yz} \\ -I_{zx} & -I_{zy} & I_{zz} \end{bmatrix}, \tag{2.26}$$

in which I_{ij} are the moments of inertia for $i = j$ or products of inertia if $i \neq j$, with respect to i and j axes. The inertia tensor is defined in the spacecraft body frame.

As the attitude control subsystem is not considered in this work, the analysis will be based on a small satellite in free movement, that is, there is no internal equipment generating torque on the spacecraft. There is no loss of generality in this approach.

In the case of free rotational motion, the only torques acting over the spacecraft are the disturbing ones (WERTZ, 1978). For a small spacecraft in Low Earth Orbit (LEO), the most significant disturbing torques are the gravity-gradient, aerodynamic drag and the residual magnetic moment dipole, which will be presented next (WERTZ, 1978; MARKLEY; CRASSIDIS, 2014).

2.4.1 Gravity-Gradient Torque

On a rigid body subject to a gravitational field, variable Earth's gravitational forces will act over the object point masses due to the field's non-uniformity and its inverse square law (WERTZ, 1978). The gravitational force on the i-th mass element if given by

$$\mathbf{F}_g^i = -m_i \mu_\oplus \frac{\mathbf{r}_{oi}}{r_{oi}^3}, \tag{2.27}$$

in which $\mu_\oplus$ is the Earth's gravitational constant and $\mathbf{r}_{oi}$ is the mass element distance to the Earth's center. The torque produced by such point mass is

$$\mathbf{T}_{gg}^i = \mathbf{r}_{ic} \times \mathbf{F}_g^i, \tag{2.28}$$

with $\mathbf{r}_{ic}$ being the distance between the body center-of-mass and the mass element.

Through the integration of infinitesimal point masses or the sum of discrete mass elements, the resulting gravity-gradient torque is given by

$$\mathbf{T}_{gg} = 3\frac{\mu_\oplus}{r_{oc}^5}(\mathbf{r}_{oc} \times \mathbf{J}\mathbf{r}_{oc}), \tag{2.29}$$

with $\mathbf{r}_{oc}$ being the distance between the body center-of-mass and the center of Earth. Equivalently (WERTZ, 1978),

$$\mathbf{T}_{gg} = 3\omega_o^2(A_{BI}\mathbf{o}_{3I}) \times \mathbf{J}(A_{BI}\mathbf{o}_{3I}), \tag{2.30}$$

in which $\mathbf{o}_{3I}$ is the radial LVLH vector in nadir direction and ω_0 is the angular orbital velocity, given by

$$\omega_o = \frac{2\pi}{T_o} = \sqrt{\frac{\mu_\oplus}{r^2}}, \tag{2.31}$$

with T_o as the satellite orbital period. For more details, see (WERTZ, 1978).

2.4.2 Aerodynamic Torque

Satellites in Low Earth Orbits (LEO) may interact with the atmosphere, which is considered to exists up to 10,000 km. A rigid body moving in this conditions will suffer a drag force due to the contact between the air particles and the vehicle. The drag force computation needs an atmospheric model (MARKLEY; CRASSIDIS, 2014).

The basic assumption is that the atmosphere is rotating with the Earth. Also, the air density is simplified through an exponential function of the altitude (MARKLEY; CRASSIDIS, 2014). The relative velocity between the satellite and the air flow is given by

$$\mathbf{v}_{rel} = \mathbf{v}_{ECI} + \boldsymbol{\omega}_{\oplus} \times \mathbf{r}_{ECI}, \tag{2.32}$$

in which $\boldsymbol{\omega}_{\oplus}$ is the Earth's rotation angular velocity

$$\boldsymbol{\omega}_{\oplus} = 0.000072921158553 \cdot \begin{bmatrix} 0 \\ 0 \\ 1 \end{bmatrix} \quad [rad/s]. \tag{2.33}$$

Transforming the relative velocity from the inertial frame to the body frame will leads to

$$\mathbf{v}_{aero} = \mathbf{A}_{BI}\mathbf{v}_{rel}. \tag{2.34}$$

The spacecraft's body surface can be considered as a set of planar faces (MARKLEY; CRASSIDIS, 2014). The air flowing trough a face will produce a aerodynamic drag force given by

$$\mathbf{F}_{drag} = \frac{1}{2}\rho C_D \|\mathbf{v}_{aero}\|^2 S_i \hat{\mathbf{v}}_{aero} \max\{(\hat{\mathbf{n}}_i \cdot \hat{\mathbf{v}}_{aero}), 0\}, \tag{2.35}$$

in which S_i is the spacecraft i-th face area, $\hat{\mathbf{v}}_{aero}$ is the relative velocity unit vector and $\mathbf{n}_i \cdot \hat{\mathbf{v}}_{aero}$ is the cosine of the angle between such face normal vector and the air flux velocity. The terms above inform the effective face area that is perpendicular to the air.

The total drag force acting on the vehicle will be the sum of the forces on all spacecraft's faces. The point in the body where one considers the resulting force is applied is called Center of Pressure (CoP) (MARKLEY; CRASSIDIS, 2014). Once the Center of Mass (CoM) and the CoP may be different locations, the drag force will produce a torque over the CoM given by

$$\mathbf{T}_{aero} = \mathbf{r}_{aero} \times \mathbf{F}_{drag}, \tag{2.36}$$

with $\mathbf{r}_{aero}$ given by

$$\mathbf{r}_{aero} = \mathbf{r}_{CoM} - \mathbf{r}_{CoP}, \tag{2.37}$$

in which $\mathbf{r}_{CoM}$ is the center of mass location and $\mathbf{r}_{CoP}$ is the center of pressure, both described in the body frame (MARKLEY; CRASSIDIS, 2014). Finally, the aerodynamic torque is given by

$$\mathbf{T}_{aero} = -\frac{1}{2}\rho C_D V^2 S_i(\mathbf{v}_{aero} \times \mathbf{r}_{aero}) \max\{(\mathbf{n}_i \cdot \mathbf{v}_{aero}), 0\}, \tag{2.38}$$

in which ρ is the atmospheric air density, C_D is the dimensionless drag coefficient, $\mathbf{r}_{aero}$ is the distance between the spacecraft center of mass and the center of pressure.

2.4.3 Residual Magnetic Dipole Torque

Electric current loops and magnetized materials produce a magnetic field, acting as a magnet, what is called magnetic dipole moment (IVANOV *et al.*, 2018). The generated field interacts with the external magnetic field resulting in a torque that seeks to align both fields. The magnetic torque is given by

$$\mathbf{T}_{rm} = \mathbf{m} \times \mathbf{B}, \tag{2.39}$$

where $\mathbf{T}_{rm}$ is the torque, $\mathbf{m}$ is the magnetic moment and $\mathbf{B}$ is the external magnetic field. For spacecrafts orbiting the Earth, the external field is the geomagnetic one.

The magnetic dipole generated by a current loop I in a wire forming a circular enclosed area of radius R is given by

$$\mathbf{m} = I \cdot \mathbf{A}_{loop}, \tag{2.40}$$

in which $\mathbf{A}_{loop} = \pi R^2 \ \hat{\mathbf{n}}_A$ is the enclosed area and $\hat{\mathbf{n}}_A$ is the associated normal vector.

Such current loop produces a magnetic flux density given by:

$$\mathbf{B} = \frac{\mu_0}{4\pi} \frac{2\pi I R^2}{(d_m^2 + R^2)^{3/2}} \hat{\mathbf{n}}_A, \tag{2.41}$$

in which d_m is the distance of an arbitrary point related to the center of the wire loop area, in the normal vector direction.

For simulation purposes, the distance of the magnetic dipole to the spacecraft devices can be neglected, that is, $d_m \ll R$, and the relation between the magnetic dipole and the magnetic

flux density is given by

$$\mathbf{B} = \frac{\mu_0}{2\pi}\frac{\mathbf{m}}{R^3}. \tag{2.42}$$

Once the magnetic dipole vector and the generated magnetic field vector are aligned on the same axes, there is no contribution to the torque. The additional field will only interfere in the magnetometers measurements.

The residual magnetic moment is the dominant source of disturbance torque for small satellites in LEO orbit, since its magnitude is higher than the others torques (HAJIYEV; SOKEN, 2020).

2.4.4 Solar Radiation Pressure Torque

The solar radiation when falls over satellites bodies will produce a force on the illuminated area due to the exchange of momentum with the radiation. Such force may generate a torque on the spacecraft with respect to its center-of-mass. Both the force and torque will disturb the orbit and attitude, respectively. Vehicle with high area-to-mass ratio will be more affected by this phenomena.

The solar radiation pressure (SRP) force is given by (MARKLEY; CRASSIDIS, 2014)

$$\mathbf{F}_{SRP} = -P_{\odot}S_i\left[2\left(\frac{R_{diff}}{3} + R_{spec}(\hat{\mathbf{n}}_i \cdot \hat{\mathbf{r}}_{sat\odot})\right)\hat{\mathbf{n}}_i + (1 - R_{spec})\hat{\mathbf{r}}_{sat\odot}\right]\max\{(\hat{\mathbf{n}}_i \cdot \hat{\mathbf{r}}_{sat\odot}), 0\}, \tag{2.43}$$

in which $P_{\odot}$ is the solar radiation power density, R_{diff} is the diffuse reflectivity coefficient, R_{spec} is the specular reflectivity coefficient, S_i is the i-th face area and $\hat{\mathbf{n}}_i$ is the related normal vector.

Analogous to the aerodynamic torque, the SRP torque is given by

$$\mathbf{T}_{SRP} = \mathbf{r}_{SRP} \times \mathbf{F}_{SRP}, \tag{2.44}$$

with $\mathbf{r}_{SRP}$ as

$$\mathbf{r}_{SRP} = \mathbf{r}_{CoM} - \mathbf{r}_{CoP-S}, \tag{2.45}$$

where $\mathbf{r}_{CoM}$ is the center of mass location and $\mathbf{r}_{CoP-S}$ is the center of solar radiation pressure, both described in the body frame.

Due to the reduced dimensions of small satellites, the SRP toque is less significant than the other disturbance sources. In this work this disturbance will not be accounted for the simulations with no loss of reliability in the results.

2.5 ENVIRONMENT MODELS

2.5.1 Satellite Orbital Motion Propagation

For the mission analysis, the spacecraft motion is one of the primaries concern. The formulation considered in this work is the Simplified General Perturbations-4 (SGP4) model, which uses the Two-line Elements (TLE) file as the only orbital data source and provide a prediction for the satellite position and velocity over time (HOOTS; ROEHRICH, 1980). TLE files are daily published by the United States Aerospace Defense Command.

The SGP4 propagator considers secular, short-periodic and long-periodic effects of perturbations on the mean motion through simplified models. The coordinate reference system is the True Equator Mean Equinox (TEME), which is a kind of ECI frame with a simplification related to the uniform equinox (VALLADO *et al.*, 2006; MEEUS, 1991).

It considers the zonal harmonic of the Earth gravitational field, J_2, J_3 and J_4. The model includes the third-body influence (Sun and Moon) in secular, long-period and short-period periodic effects. Also, the secular effects of the atmospheric drag is taken into account for LEO satellites (VALLADO; WERTZ, 2013).

2.5.2 Earth Magnetic Field

As described in Vallado & Wertz (2013), the Earth Magnetic Field is modeled as the gradient of the magnetic potential, which is approximated by a spherical harmonic series expansion. One of the standard models is called International Geomagnetic Reference Field (IGRF) and it consists of the mathematical description along with the coefficient values for the series expansion (ALKEN *et al.*, 2021). The model allows computing the geomagnetic field at any point in space given its spherical coordinates. Furthermore, it allows not only computational simulations but

also serves as input data for laboratory experiments in Helmholtz cages.

The magnetic field is defined as (ALKEN *et al.*, 2021)

$$\mathbf{B}(r,\theta,\phi,t) = -\nabla V(r,\theta,\phi,t), \tag{2.46}$$

in which $V(r,\theta,\phi,t)$ is the magnetic potential as given by

$$V(r,\theta,\phi,t) = a\sum_{n=1}^{N}\sum_{m=0}^{n}\left(\frac{a}{r}\right)^{n+1}\left[{g_n}^m(t)\cos m\phi + {h_n}^m(t)\sin m\phi\right]P_n^m(\cos\theta) \tag{2.47}$$

with r being the distance from the Earth's center, θ the geocentric co-latitude, ϕ the geocentric longitude and $a = 6371.2$ km the mean Earth's radius. The terms $P_n^m(\cos\theta)$ are Schmidt semi-normalized associated Legendre functions of degree n and order m.

The current available model is the IGRF-13 (ALKEN *et al.*, 2021), which means the model order is $N = 13$. For any time instant t, the related coefficients can be computed as

$$g_n^m(t) = g_n^m(T_t) + (t - T_t)\dot{g}_n^m(T_t), \tag{2.48a}$$

$$h_n^m(t) = h_n^m(T_t) + (t - T_t)\dot{h}_n^m(T_t), \tag{2.48b}$$

with T_t being the time instant in which the coefficients are provided by the model. The time derivatives are computed as follow (ALKEN *et al.*, 2021)

$$\dot{g}_n^m(T_t) = \frac{1}{5}\left(g_n^m(T_t + 5) - g_n^m(T_t)\right), \tag{2.49a}$$

$$\dot{h}_n^m(T_t) = \frac{1}{5}\left(h_n^m(T_t + 5) - h_n^m(T_t)\right). \tag{2.49b}$$

The magnetic field components in geodetic coordinates then can be obtained from the gradient operator and are given by (WERTZ, 1978)

$$\mathbf{B}_r = -\frac{\partial V}{\partial r} = \sum_{n=0}^{N}(n+1)\left(\frac{a}{r}\right)^{n+2}\sum_{m=0}^{n}\left[{g_n}^m(t)\cos m\phi + {h_n}^m(t)\sin m\phi\right]P_n^m(\cos\theta), \tag{2.50a}$$

$$\mathbf{B}_\theta = -\frac{1}{r}\frac{\partial V}{\partial \theta} = -\sum_{n=0}^{N}\left(\frac{a}{r}\right)^{n+2}\sum_{m=0}^{n}\left[{g_n}^m(t)\cos m\phi + {h_n}^m(t)\sin m\phi\right]\frac{\partial P_n^m(\cos\theta)}{\partial\theta}, \tag{2.50b}$$

$$\mathbf{B}_\phi = -\frac{1}{r\sin(\theta)}\frac{\partial V}{\partial \phi} = -\sum_{n=0}^{N}\left(\frac{a}{r}\right)^{n+2}\sum_{m=0}^{n} m\left[-{g_n}^m g_n^m(t)\sin m\phi + {h_n}^m(t)\cos m\phi\right]P_n^m(\cos\theta), \tag{2.50c}$$

The Schmidt semi-normalized Legendre polynomials must be computed for obtaining the full model. They can be defined through the Legendre polynomials, $P_n(x)$, which are the solution for the Legendre differential equation and are given by (WERTZ, 1978)

$$P_n(x) = \frac{1}{2^n n!}\left(\frac{d}{dx}\right)^n (x^2-1)^n. \tag{2.51}$$

The associated Legendre polynomials have the following definition

$$P_{n,m}(x) = (1-x^2)^{m/2}\frac{d^m}{dx^m}(P_n(x)). \tag{2.52}$$

The Gaussian normalized Legendre polynomials are defined as functions of the associated polynomials by

$$P^{n,m} = \frac{2^n!(n-m)!}{(2n)!}P_{n,m}. \tag{2.53}$$

Finally, the Schmidt and Gaussian normalized polynomials are related by

$$P_n^m = S_{n,m}P^{n,m}, \tag{2.54}$$

with

$$S_{n,m} = \left[\frac{(2-\delta_m^0)(n-m)!}{(n+m)!}\right]^2 \frac{(2n-1)!!}{(n-m)!} \tag{2.55}$$

in which $n!!$ is the double factorial and $\delta_j^i = 1$ if $i = j$ and $\delta_j^i = 0$, if $i \neq j$ (Kronecker delta).

In order to compute efficiently the polynomials, a recursive form is considered where the Schmidt functions are obtained from the Gaussian polynomials calculated as (WERTZ, 1978)

$$P^{0,0} = 1, \tag{2.56a}$$

$$P^{n,n} = \sin\theta P^{n-1,m-1}, \tag{2.56b}$$

$$P^{n,m} = \cos\theta P^{n-1,m} - K^{n,m}P^{n-2,m}, \tag{2.56c}$$

with

$$K^{n,m} = \frac{(n-1)^2-m^2}{(2n-1)(2n-3)}, \quad n>1 \quad \text{and} \quad K^{n,m} = 0, \quad n = 1. \tag{2.57}$$

The recursive solution for the factor $S_{n,m}$ is given by

$$S_{0,0} = 1, \tag{2.58a}$$

$$S_{n,0} = S_{n-1,0}\frac{2n-1}{n}, \tag{2.58b}$$

$$S_{n,m} = S_{n,m-1}\sqrt{\frac{(n-m+1)(\delta_m^1+1)}{n+m}}. \tag{2.58c}$$

Finally, the recursive form of the polynomials derivatives is given by

$$\frac{\partial P^{0,0}}{\partial \theta} = 0, \tag{2.59a}$$

$$\frac{\partial P^{n,n}}{\partial \theta} = \sin\theta \frac{\partial P^{n-1,n-1}}{\partial \theta} + \cos\theta P^{n-1,n-1}, \quad n \geq 1, \tag{2.59b}$$

$$\frac{\partial P^{n,m}}{\partial \theta} = \cos\theta \frac{\partial P^{n-1,m}}{\partial \theta} - \sin\theta P^{n-1,m} - K^{n,m} \frac{\partial P^{n-2,m}}{\partial \theta}. \tag{2.59c}$$

The IGRF-13 code used in this work is provided by the British Geological Survey (BGS) [1] with modifications made by the author for the spacecraft attitude simulation purposes.

2.5.3 Sun Inertial Position

The Sun position is another fundamental model, since it is the primary power source for the most of the spacecrafts. According to Vallado & Wertz (2013), a more precise approach to determine the position is through the data set DE430, a set of celestial bodies' ephemerides provided by the Jet Propulsion Laboratory (JPL) and generated by laser observations and the numerical integration of a dynamic system. However, this model requires the access to the data and the need of numerical methods. A simpler and less precise model is based on analytical equations that may be considered in simulations and is also useful for implementing in the onboard software. This model considers the Sun elliptic motion, containing polynomials and trigonometric terms only (MEEUS, 1991; URBAN; SEIDELMANN, 2013).

In order to compute the Sun position, the date must be converted to Julian date, JD_{UT1}, as follow

$$\begin{aligned} JD_{UT1} = 367y - \text{INT}\left\{\frac{7\left\{y + \text{INT}[(m+9)/12]\right\}}{4}\right\} + \text{INT}\left\{\frac{275m}{9}\right\} \\ + \frac{h + min/60 + s/3600}{24} + d + 1721013.5, \end{aligned} \tag{2.60}$$

where the date is a set of $\{y, m, d, h, min, s\}$ and $INT\{\cdot\}$ is the function that return the integer part of a number.

The Julian centuries is given by

$$T_{UT1} = \frac{JD_{UT1} - 2451545.0}{36525}. \tag{2.61}$$

[1] available on <https://www.ngdc.noaa.gov/IAGA/vmod/pyIGRF.zip>

The Sun mean longitude is computed by (VALLADO; WERTZ, 2013)

$$\lambda_{M_\odot} = 280.460^\circ + 36000.770\ T_{UT1}, \tag{2.62}$$

and the mean anomaly by

$$M_\odot = 357.5277233^\circ + 35999.05034\ T_{UT1}. \tag{2.63}$$

Then, the longitude of the ecliptic is defined as

$$\lambda_{ecliptic} = \lambda_{M_\odot} + 1.914666471^\circ\ \sin(M_\odot) + 0.019994643^\circ\ \sin(2M_\odot). \tag{2.64}$$

Next, the ecliptic obliquity is computed by

$$\varepsilon = 23.439291^\circ - 0.0130042\ T_{UT1}. \tag{2.65}$$

The Sun distance to the Earth in Astronomic Unit (AU) is given by the following equation

$$\mathbf{r}_\odot = 1.000140612 - 0.016708617\cos(M_\odot) - 0.000139589\cos(2M_\odot) \qquad [AU]\,. \tag{2.66}$$

The Sun direction with respect to the Earth in the ECI frame is given by

$$\mathbf{S}_{ECI} = \begin{bmatrix} \cos(\lambda_{ecliptic}) \\ \sin(\lambda_{ecliptic})\cos(\varepsilon) \\ \sin(\lambda_{ecliptic})\sin(\varepsilon) \end{bmatrix}. \tag{2.67}$$

Finally, given the Sun and the satellite inertial positions computed with the presented models, it is possible to determine the Sun direction with respect to the spacecraft as $\mathbf{S}_{sat} = \mathbf{r}_\odot - \mathbf{r}_{sat}$.

2.5.4 Earth's Albedo

An important phenomenona that affects the Sun sensor accuracy is the Earth albedo, which is the solar radiation reflected by the planet surface. When such energy is captured by the onboard sensors, it can interfere in the Sun direction estimation (CILDEN-GULER *et al.*, 2021). In order to estimate such index, Bhanderi & Bak (2005) presents a source of measurements constituting a grid of data points, an 180×288 matrix, dividing the Earth surface into cells.

Albedo is measured as the reflectivity index, which vary according to the cloud coverage, geographic location, season of the year and type of surface. In (BHANDERI; BAK, 2005) the reflectivity index is provided by NASA's Total Ozone Mapping Spectrometer (TOMS) satellite, which recorded the measurements observations constituting a grid of data points.

The energy reflected by a surface area cell located at latitude and longitude (ϕ_g, θ_g) that is perceived by the spacecraft is given by the equation

$$E_c(\phi_g, \theta_g) = \begin{cases} \dfrac{\rho(\phi_g, \theta_g) E_{AM0} A_c(\phi_g) \hat{\mathbf{r}}_{Sun}^T \hat{\mathbf{n}}_c \hat{\mathbf{r}}_{sat}^T \hat{\mathbf{n}}_c}{\pi \|\mathbf{r}_{sat}\|^2} & \text{if } (\phi_g, \theta_g) \in \mathbf{V}_{Sun} \cap \mathbf{V}_{sat} \\ 0 & \text{otherwise} \end{cases}, \tag{2.68}$$

in which $\rho(\phi_g, \theta_g)$ is the reflectivity index, $A_c(\phi_g)$ is the cell area size, $\hat{\mathbf{n}}_c$ is the cell normal vector, $\hat{\mathbf{r}}_{Sun}$ is the Sun direction vector with respect to the cell and $\hat{\mathbf{r}}_{sat}$ is the satellite line of sight also with respect to the same cell. The set $\mathbf{V}_{Sun} \cap \mathbf{V}_{sat}$ is formed by all surface cells illuminated by the Sun and visible by the satellite. The scalar E_{AM0} is the solar intensity at air mass zero, which means the flux density upper the atmosphere, where the value is $1367 W/m^2$. Figure 2.3 illustrates the geometry related to the Albedo model.

The total energy, E_a, that reaches the satellite is the sum of the radiation from all cells in the set, that is

$$E_a = \sum_{\mathbf{V}_{Sun} \cap \mathbf{V}_{sat}} E_c(\phi_g, \theta_g). \tag{2.69}$$

Figure 2.3. Solar radiation reflection geometry(left) and effective area(right).

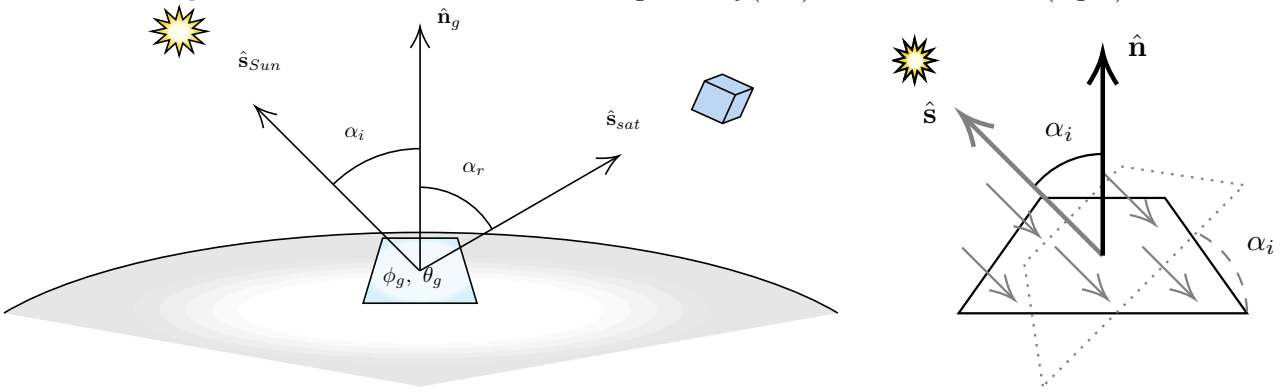

Source: Author.

Finally, the Earth albedo resulting direction can be approximated as the radial vector according to the satellite's orbit position, that is, the satellite's nadir opposite direction (BHANDERI, 2006).

2.6 SENSORS MODELS

The attitude determination problem consists in the processing of sensor observations in order to compute the spacecraft pose. For that purpose the correct sensor model must be considered to obtain a reliable result. There are vector measurement sensors, such as magnetometers, Sun sensors, Earth horizon sensors and star trackers, and there are the rate of change sensors, as gyroscopes.

Each sensor of the satellite is modeled as a true measurement corrupted by noise and the error components are treated as random processes. The sensor noise features are considered in the filtering process for optimizing the solution. A more complete model also includes misalignment, scale factors and non-orthogonality. In this work, the attitude determination and control system will have a tri-axial gyroscope, a tri-axial magnetometer and Sun sensors, which is a broadly used set of sensors concerning small satellites.

2.6.1 Gyroscopes

The rate gyroscope measures the angular velocity of a rigid body relative to the inertial frame. The integration of the observations over time will result in the body's angular displacement, hence its orientation (MARKLEY; CRASSIDIS, 2014). The model consist of a true angular velocity vector along with a bias value and a noise signal as in the following equations

$$\tilde{\boldsymbol{\omega}}(t) = \boldsymbol{\omega}^{true}(t) + \boldsymbol{\beta}(t) + \boldsymbol{\eta}_v(t), \tag{2.70a}$$

$$\dot{\boldsymbol{\beta}}(t) = \boldsymbol{\eta}_u(t), \tag{2.70b}$$

in which $\boldsymbol{\omega}^{true}(t)$ is the unknown true angular velocity vector, $\boldsymbol{\beta}(t)$ is the sensor bias, the $\boldsymbol{\eta}_v(t)$ and $\boldsymbol{\eta}_u(t)$ are uncorrelated zero-mean Gaussian white-noise processes with variance, respectively, given by

$$E\{\boldsymbol{\eta}_v(t)\boldsymbol{\eta}_v^T(\tau)\} = \sigma_v^2\mathbf{I}_{3\times3}\delta(t-\tau), \tag{2.71a}$$

$$E\{\boldsymbol{\eta}_u(t)\boldsymbol{\eta}_u^T(\tau)\} = \sigma_u^2\mathbf{I}_{3\times3}\delta(t-\tau), \tag{2.71b}$$

in which $\delta(t-\tau)$ is the Kronecker delta defined as

$$\delta(t-\tau) = \begin{cases} 1, & \text{if } t = \tau, \\ 0, & \text{if } t \neq \tau. \end{cases} \tag{2.72}$$

For simulations purposes, in (MARKLEY; CRASSIDIS, 2014) is developed a gyroscope model which generates discrete-time observations. This solution considers the trapezoidal rule for integration. As result, the sensor measurements will be given by

$$\tilde{\boldsymbol{\omega}}_k = \boldsymbol{\omega}_k^{true} + \frac{1}{2}(\boldsymbol{\beta}_k^{true} + \boldsymbol{\beta}_{k-1}^{true}) + \left(\frac{\sigma_v^2}{\Delta t} + \frac{1}{12}\sigma_u^2 \Delta t\right)^{1/2} \mathbf{N}_{vk}, \tag{2.73a}$$

$$\boldsymbol{\beta}_k^{true} = \boldsymbol{\beta}_{k-1}^{true} + \sigma_u \Delta t^{1/2} \mathbf{N}_{uk}, \tag{2.73b}$$

in which $\mathbf{N}_u \sim \mathcal{N}(0,1)$ and $\mathbf{N}_v \sim \mathcal{N}(0,1)$ are zero-mean Gaussian processes with unit variance.

2.6.2 Magnetometer

The magnetometer measures the magnetic field where the sensor is immersed in, as the geomagnetic field and electric current generated fields. Such instrument is one of the most common ones in Low Earth Orbit (LEO) vehicles due to its simplicity, low cost, low power consumption and availability in any condition (like eclipses). Furthermore, there are many magnetometer-only attitude determination algorithms. The observation model is given by

$$\tilde{\mathbf{B}}_B(t) = \mathbf{A}_{BR}\mathbf{B}_R^{true}(t) + \boldsymbol{\eta}_m(t), \tag{2.74}$$

where $\tilde{\mathbf{B}}(t)$ is the sensor output reading, $\mathbf{B}^{true}(t)$ is the true field value and $\boldsymbol{\eta}_m(t)$ is a zero-mean Gaussian random process with variance

$$E\{\boldsymbol{\eta}_m(t)\boldsymbol{\eta}_m^T(\tau)\} = \sigma_m^2 \mathbf{I}_{3\times 3}\delta(t-\tau), \tag{2.75}$$

the true quantity can be considered as the observation computed through the environment model rotated to the sensor body frame (HAJIYEV; SOKEN, 2020).

Attitude determination algorithms makes use of the Earth's magnetic field model as the IGRF already mentioned. In this context, the magnetic field generated by other sources constitutes disturbances in the sensor measurements (HAJIYEV; SOKEN, 2020). Spacecrafts have electronics circuits working in different levels of electric current, which produces magnetic fluxes according to the Àmpere's Law. Some LEO vehicles may employ permanent magnets for passive attitude stabilization methods. Besides, metallic materials in the satellite structure can suffer the process of magnetization, acting also as magnets.

The effects in the magnetometer readings can be divided into two categories of distortions, that is hard iron and soft iron. The first type is characterized as a constant bias in the observations.The second one is characterized as deformations or deflections in the measured magnetic field.

In this scenario, a more complete model considers a constant bias vector, $\mathbf{b}_m$, in the observations resulting in the following equation

$$\tilde{\mathbf{B}}_B(t) = \mathbf{A}_{BR}\mathbf{B}_R^{true}(t) + \mathbf{b}_m + \boldsymbol{\eta}_m(t). \tag{2.76}$$

Due to the disturbances sources inherent to the space vehicles, the magnetometer's calibration process is fundamental and a variety of algorithms are present in the literature (HAJIYEV; SOKEN, 2020). Another approach to reduce the distortions in the sensor observations is the use of boom deployed magnetometer, which isolates the instrument from the satellite body.

2.6.3 Sun Sensor

Sun sensors are used for the determination of the solar radiation direction with respect to the sensors assembly. Once the Sun is the primary power source for almost all spacecrafts, the Sun vector estimation is primordial for the satellite survivability. Also, such vector can be used for attitude determination in methods that use vector measurements, as the Geomagnetic field direction vector (MARKLEY; CRASSIDIS, 2014).

Such sensors convert the light radiation into electrical current signal which can be read by the onboard microcontroller. The signal is proportional to the irradiation flux density, the irradiation incidence angle with respect to the sensor plane and the area size of the photodetector (light-sensitive material). Cubesats use photodiodes as Sun sensors due the low cost, small size and simplicity of integration, as photovoltaic cells constitute sensors for larger satellites. Currently, there are also components based on Complementary Metal-Oxide-Semiconductor (CMOS) and Charge-Coupled Device (CCD) imagers.

With a set of Sun sensors mounted in the spacecraft body, covering different directions, it is possible to infer the Sun direction. Then, a unit vector in the satellite body frame is obtained

along with the related noise as (HAJIYEV; SOKEN, 2020)

$$\tilde{\mathbf{S}}(t) = \mathbf{A}_{BR}\mathbf{S}_R^{true}(t) + \boldsymbol{\eta}_s(t), \tag{2.77}$$

where $\tilde{\mathbf{S}}(t)$ is the sensor output reading, $\mathbf{S}^{true}(t)$ is the true field value and $\boldsymbol{\eta}_s(t)$ is a zero-mean Gaussian random process. The true quantity can be considered as the observation computed through the environment model rotated to the sensor body frame.

The previous equation is the general observation model for vector measurements. The Sun direction computing will depend on the sensor type and configuration. The basic method to determine the solar direction is based on photodiodes mounted on different faces of the satellite body, where the electric current generated by each device is a function of the incidence angle and has a co-sine profile curve, that is

$$I_{css-j} = I_{max}\cos(\alpha_j), \quad 0^\circ \leq \alpha_j \leq 90^\circ, \tag{2.78}$$

in which I_{css-j} is the electric current generated by the j-th coarse sun sensor (CSS), I_{max} is the maximum electric current value (null incidence angle) which depends on the solar radiation intensity and α_j is the incidence angle of the Sun flux.

Considering the theoretical minimum configuration of six sensors aligned to the satellite body frame and opposite directions, the Sun direction vector can be determined by (MARKLEY; CRASSIDIS, 2014)

$$\tilde{\mathbf{S}} = \frac{1}{I_{max}}\begin{bmatrix} I_{+X} - I_{-X} \\ I_{+Y} - I_{-Y} \\ I_{+Z} - I_{-Z} \end{bmatrix}, \tag{2.79}$$

in which $\{+X, -X, +Y, -Y, +Z, -Z\}$ are the sensors normal vector direction towards the spacecraft body frame. The result is the unit vector compound of the direction cosine. In practice, it is necessary more than six photodiodes, once the field-of-view may be reduced.

For simulation purposes, the observation model can consider the fact that in cosine sensors, that is, it is a function of an angle cosine, the noise level is higher for small incidence angles and the level reduces as the elevation increases (ASUNDI *et al.*, 2021). In this case, the measurement can be modeled as

$$\tilde{\mathbf{S}} = A_{BR}\mathbf{S}^{true} + \eta_s(1 - A_{BR}\mathbf{S}^{true}), \tag{2.80}$$

or each photodiode sensor may be defined as

$$I_{css-j} = I_{max}\mathbf{S}^{true} \cdot \hat{\mathbf{n}}_j^T + \eta_s(1 - \mathbf{S}^{true} \cdot \hat{\mathbf{n}}_j^T), \tag{2.81}$$

in which $\hat{\mathbf{n}}_j^T$ is the normal vector relative to the j-th sensor plane.

Another approach is to add the sensor noise in the azimuth and elevation angles related to the detector plane (BARONI, 2017). So the unit vector is transformed from the Cartesian coordinates to the spherical ones for this operation and transformed back to the Cartesian system. The Sun vector (x,y,z) can be then obtained as

$$r = \sqrt{x^2 + y^2 + z^2}, \tag{2.82a}$$

$$\theta = \arccos\left(z/r\right), \tag{2.82b}$$

$$\varphi = \arctan\left(y/x\right). \tag{2.82c}$$

After adding the noise, the Cartesian vector can be retrieved by

$$x = r\sin(\theta + \eta_s)\cos(\varphi + \eta_s), \tag{2.83a}$$

$$y = r\sin(\theta + \eta_s)\sin(\varphi + \eta_s), \tag{2.83b}$$

$$z = r\cos(\theta + \eta_s). \tag{2.83c}$$

An important consideration regarding unit vector measurements is the noise covariance matrix. Crassidis *et al.* (2007) states that the measurement model noise constitutes a rank-deficient matrix, once the errors may be given in the elevation and azimuth directions. But Shuster (1990) has shown that an approximation in which the matrix is non-singular and provide consistent results is given by $\mathbf{R} = \sigma^2\mathbf{I}_{3\times3}$.

Finally, it is important to mention that Sun sensors suffer the interference of the Earth's Albedo, which can produce an error of considerable magnitude. In such cases, the Albedo estimation must be computed for a more precise attitude determination. However, the Albedo computing is attitude-depended and it is a time consuming process, which may be impracticable for on-board applications. So it can be considered in simulations or offline telemetry processing.

Finally, Figure 2.4 presents the proposed approach in this work to estimate the attitude. It shows how the models and data are related to each other in order to generate an attitude determination and control environment.

Figure 2.4. Attitude Determination and Control System.

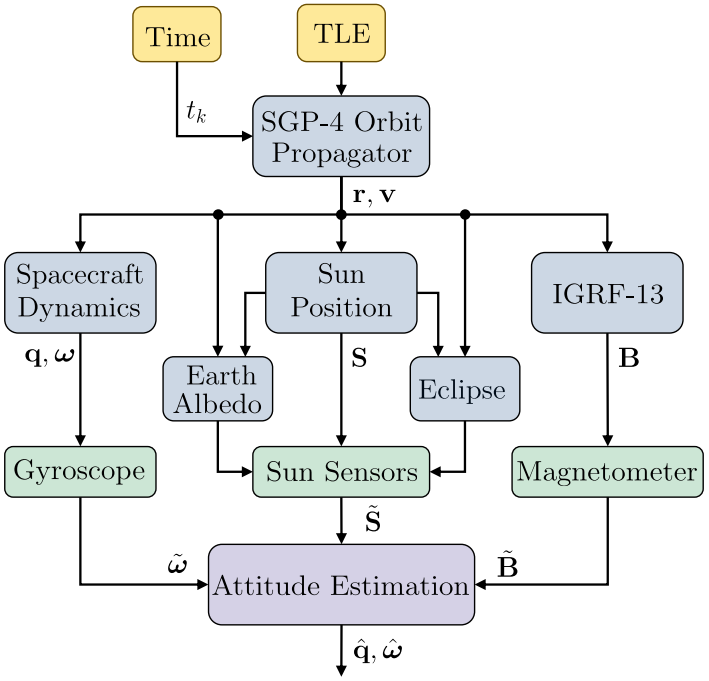

Source: Author.

CHAPTER 3

ATTITUDE ESTIMATION AND FILTERING

This chapter discuss the Kalman filtering theory and its application to the attitude determination problem. The linear filter algorithm is presented and its extensions to nonlinear systems also described. The chapter presents the rotational motion equations used in the process and observation models.

3.1 KALMAN FILTER

Given a mathematical model as function of a vector of variables, $\mathbf{x}$, and a set of measured observations $\tilde{\mathbf{y}}$, the filtering problem concern the solution of the following conditional expected value

$$\hat{\mathbf{x}}_k = E\{\mathbf{x}_k|\mathbf{Y}_k\}, \tag{3.1}$$

where $E\{\cdot\}$ is the expectation operation and $\mathbf{Y}_k = \{\mathbf{y}_1, \ldots, \mathbf{y}_k\}$ is a random process of observations in which $\mathbf{y}_i$ are realizations taken in discrete instants (BAR-SHALOM *et al.*, 2002). For the case of the system evolving over time, the solution for such problem is a recursive algorithm for the state estimation called Kalman filter.

A discrete-time linear dynamic system is described by the following set of equations

$$\mathbf{x}_k = \mathbf{F}_{k-1}\mathbf{x}_{k-1} + \mathbf{B}_{k-1}\mathbf{u}_{k-1} + \mathbf{G}_{k-1}\mathbf{w}_{k-1}, \tag{3.2a}$$

$$\mathbf{y}_k = \mathbf{H}_k\mathbf{x}_k + \mathbf{v}_k, \tag{3.2b}$$

in which $\mathbf{x}_k \in \mathbb{R}^n$ is the state vector, $\mathbf{F}_{k-1} \in \mathbb{R}^{n\times n}$ is the dynamical system function that updates the state in time, $\mathbf{w}_{k-1} \in \mathbb{R}^p$ is the model error vector, $\mathbf{G}_{k-1} \in \mathbb{R}^{n\times p}$ is a function that maps the process errors to the state space. The vector $\mathbf{u}_{k-1} \in \mathbb{R}^l$ is the control inputs and the matrix $\mathbf{B}_{k-1} \in \mathbb{R}^{n\times l}$ maps the control effects into the system. Besides, $\mathbf{y}_k \in \mathbb{R}^m$ is the output or measurement vector, while $\mathbf{H}_k \in \mathbb{R}^{m\times n}$ maps the state vector into the observation space and $\mathbf{v}_k \in \mathbb{R}^m$ is the measurement error vector.

Both process and observation error vectors are modeled as uncorrelated Gaussian random variables, that is

$$E\{\mathbf{w}_k\mathbf{w}_j^T\} = \mathbf{Q}_k\delta_{kj}, \tag{3.3a}$$

$$E\{\mathbf{v}_k\mathbf{v}_j^T\} = \mathbf{R}_k\delta_{kj}, \tag{3.3b}$$

$$E\{\mathbf{w}_k\mathbf{v}_j^T\} = E\{\mathbf{v}_k\mathbf{w}_j^T\} = \mathbf{0}, \tag{3.3c}$$

with $\delta_{kj} = 1$ if $k = j$ and $\delta_{kj} = 0$, $k \neq j$ (Kronecker delta).

In this work, the control problem will not be accounted in the filtering analysis. That is, the spacecraft has no actuator which results in input control vector $\mathbf{u}_k = \mathbf{0}$.

The Kalman filter is a minimum mean square error (MMSE) estimator, which solution is given as

$$\hat{\mathbf{x}}_k = \bar{\mathbf{x}}_k + \mathbf{K}(\tilde{\mathbf{y}}_k - \hat{\mathbf{y}}_k), \tag{3.4}$$

where $\bar{\mathbf{x}}$ is $E\{\mathbf{x}\} = \bar{\mathbf{x}}$, $\hat{\mathbf{x}} = E\{\mathbf{x}|\mathbf{y} = \tilde{\mathbf{y}}\}$ and $\mathbf{K}$ is a weighting factor. This result is called the Gauss-Markov Theorem (CRASSIDIS; JUNKINS, 2012).

Let $\mathbf{x}_k$ be the true system state and $\hat{\mathbf{x}}_k$ be the state estimate, then the *a priori* error $\tilde{\mathbf{x}}_k$ is defined by

$$\tilde{\mathbf{x}}_k = \mathbf{x}_k - \hat{\mathbf{x}}_k^-, \tag{3.5}$$

which results in the following statistics for an unbiased estimator

$$E\{\mathbf{x}_k\} = \hat{\mathbf{x}}_k^-, \tag{3.6}$$

$$E\{(\mathbf{x}_k - \hat{\mathbf{x}}_k)(\mathbf{x}_k - \hat{\mathbf{x}}_k)^T\} = E\{\tilde{\mathbf{x}}_k\tilde{\mathbf{x}}_k^T\} = \mathbf{P}_k. \tag{3.7}$$

The Kalman filter considers the following system for the filtering process

$$\begin{aligned} \hat{\mathbf{x}}_k &= \mathbf{F}_{k-1}\hat{\mathbf{x}}_{k-1} + \mathbf{G}_{k-1}\mathbf{w}_{k-1}, \\ \hat{\mathbf{y}}_k &= \mathbf{H}_k\hat{\mathbf{x}}_k + \mathbf{v}_k, \end{aligned} \tag{3.8}$$

where $\hat{\mathbf{x}}$ is the estimated state vector and $\hat{\mathbf{y}}$ is the predicted or estimated output vector.

The Kalman filter algorithm is divided into two stages called prediction and update steps (KALMAN, 1960). The prediction is the computing of the *a priori* information, denoted with the superscript $(^-)$, as follow for the expectation

$$E\{\mathbf{x}_k\} = E\{\mathbf{F}_{k-1}\mathbf{x}_{k-1} + \mathbf{G}_{k-1}\mathbf{w}_{k-1}\},$$

therefore,

$$\hat{\mathbf{x}}_k^- = \mathbf{F}_{k-1}\hat{\mathbf{x}}_{k-1}, \tag{3.9}$$

and for the state error covariance matrix

$$\begin{aligned} E\{\tilde{\mathbf{x}}_k\tilde{\mathbf{x}}_k^T\} &= E\{(\mathbf{F}_{k-1}\tilde{\mathbf{x}}_{k-1} + \mathbf{G}_{k-1}\mathbf{w}_{k-1})(\mathbf{F}_{k-1}\tilde{\mathbf{x}}_{k-1} + \mathbf{G}_{k-1}\mathbf{w}_{k-1})^T\} \\ &= \mathbf{F}_{k-1}E\{\tilde{\mathbf{x}}_{k-1}\tilde{\mathbf{x}}_{k-1}^T\}\mathbf{F}_{k-1}^T + \mathbf{G}_{k-1}E\{\mathbf{w}_{k-1}\mathbf{w}_{k-1}^T\}\mathbf{G}_{k-1}^T. \end{aligned}$$

Finally,

$$\mathbf{P}_k^- = \mathbf{F}_{k-1}\mathbf{P}_{k-1}^+\mathbf{F}_{k-1}^T + \mathbf{G}_{k-1}\mathbf{Q}_{k-1}\mathbf{G}_{k-1}^T, \tag{3.10}$$

since $E\{\tilde{\mathbf{x}}_{k-1}\mathbf{w}_{k-1}^T\} = E\{\mathbf{w}_{k-1}\tilde{\mathbf{x}}_{k-1}^T\} = \mathbf{0}$ due to the fact that the state error and process noise are uncorrelated variables.

Physical dynamic systems are modeled in the continuous-time domain, while the measurements are observed at discrete time instants (BAR-SHALOM *et al.*, 2002). Given the system counterpart in continuous-time $\dot{\mathbf{x}}(t) = \mathbf{A}\mathbf{x}(t)$, $\mathbf{A}$ is a constant matrix, the propagation of the state from instant t_{k-1} to t_k is computed as

$$\begin{aligned} \mathbf{\Phi}(t_k, t_{k-1}) &= \exp\left\{\mathbf{A}(t_k - t_{k-1})\right\}, \\ &= \sum_{n=0}^{\infty} \frac{1}{n!}\mathbf{A}^n(\Delta t)^n, \end{aligned} \tag{3.11}$$

in which $\mathbf{F}_k = \mathbf{\Phi}(t_k, t_{k-1})$ is called state transition matrix and $\Delta t = t_k - t_{k-1}$ is the sample period.

The update phase, also called correction phase computes the *a posteriori* information, denoted with the superscript $(^+)$. First, consider the following *a posteriori* error defined by

$$\begin{aligned} \tilde{\mathbf{x}}_k^+ &= \mathbf{x}_k - \hat{\mathbf{x}}_k^+ \\ &= [\mathbf{x}_k + \mathbf{K_k}(\tilde{\mathbf{y}}_k - \mathbf{H}_k\mathbf{x}_k)] - \left[\hat{\mathbf{x}}_k^- + \mathbf{K}_k(\tilde{\mathbf{y}}_k - \mathbf{H}_k\hat{\mathbf{x}}_k^-)\right] \\ &= [\mathbf{x}_k + \mathbf{K}_k(\tilde{\mathbf{y}}_k - \mathbf{H}_k\mathbf{x}_k)] - \left[\hat{\mathbf{x}}_k^- + \mathbf{K}_k(\tilde{\mathbf{y}}_k - \mathbf{H}_k\hat{\mathbf{x}}_k^- - \mathbf{v}_k)\right] \\ &= (\mathbf{x} - \hat{\mathbf{x}}_k^-) - \mathbf{K}_k(\mathbf{H}_k\mathbf{x}_k - \mathbf{H}_k\hat{\mathbf{x}}_k^-) - \mathbf{K}_k\mathbf{v}_k, \end{aligned}$$

therefore,

$$\tilde{\mathbf{x}}_k^+ = \tilde{\mathbf{x}}_k^- - \mathbf{K}_k\mathbf{H}_k\tilde{\mathbf{x}}_k^- + \mathbf{K}_k\mathbf{v}_k = (\mathbf{I} - \mathbf{K}_k\mathbf{H}_k)\tilde{\mathbf{x}}_k^- + \mathbf{K}_k\mathbf{v}_k. \tag{3.12}$$

The state error covariance matrix $\mathbf{P}_k^+ = E\{\tilde{\mathbf{x}}_k\tilde{\mathbf{x}}_k^T\}$ is given by

$$\begin{aligned} E\{\tilde{\mathbf{x}}_k\tilde{\mathbf{x}}_k^T\} &= E\{\left[(\mathbf{I}-\mathbf{K}_k\mathbf{H}_k)\tilde{\mathbf{x}}_k^- + \mathbf{K}_k\mathbf{v}_k\right]\left[(\mathbf{I}-\mathbf{K}_k\mathbf{H}_k)\tilde{\mathbf{x}}_k^- + \mathbf{K}_k\mathbf{v}_k\right]^T\}, \\ &= (\mathbf{I}-\mathbf{K}_k\mathbf{H}_k)E\{(\tilde{\mathbf{x}}_k^-)(\tilde{\mathbf{x}}_k^-)^T\}(\mathbf{I}-\mathbf{K}_k\mathbf{H}_k)^T + \mathbf{K}_kE\{\mathbf{v}\mathbf{v}^T\}\mathbf{K}_k^T, \end{aligned}$$

since $E\{\tilde{\mathbf{x}}_k\mathbf{v}_k^T\} = E\{\mathbf{v}_k\tilde{\mathbf{x}}_k^T\} = \mathbf{0}$ due to the fact that the state error and measurement noise are also uncorrelated. Then,

$$\mathbf{P}_k^+ = \left[\mathbf{I}-\mathbf{K}_k\mathbf{H}_k\right]\mathbf{P}_k^-\left[\mathbf{I}-\mathbf{K}_k\mathbf{H}_k\right]^T + \mathbf{K}_k\mathbf{R}_k\mathbf{K}_k^T. \tag{3.13}$$

The optimal value of $\mathbf{K}_k$ is the one that minimizes the state error covariance (KALMAN, 1960). In that case, the matrix $\mathbf{K}_k$ is called Kalman gain. The gain matrix is found through the minimization of the following cost function

$$\mathbf{J}_{cost} = tr(\mathbf{P}_k^+) \tag{3.14}$$

$$= tr\left[(\mathbf{I}-\mathbf{K}_k\mathbf{H}_k)\mathbf{P}_k^-(\mathbf{I}-\mathbf{K}_k\mathbf{H}_k)^T + \mathbf{K}_k\mathbf{R}_k\mathbf{K}_k^T\right] \tag{3.15}$$

$$= \mathbf{P}_k^- - \mathbf{K}_k\mathbf{H}_k\mathbf{P}_k^- - \mathbf{P}_k^-\mathbf{H}_k^T\mathbf{K}_k^T + \mathbf{K}_k\mathbf{H}_k\mathbf{P}\mathbf{H}_k^T\mathbf{K}_k^T + \mathbf{K}_k\mathbf{R}\mathbf{K}_k^T, \tag{3.16}$$

where $tr\{\cdot\}$ is the trace of a matrix.

The minimization is obtained by

$$\frac{\partial\mathbf{J}_{cost}}{\partial\mathbf{K}_k} = \mathbf{0}$$
$$\frac{\partial\mathbf{J}_{cost}}{\partial\mathbf{K}_k} = -\mathbf{P}_k^{-T}\mathbf{H}_k^T - \mathbf{P}_k^-\mathbf{H}_k^T + \mathbf{K}_k(\mathbf{H}_k\mathbf{P}_k^-\mathbf{H}_k^T + (\mathbf{H}_k\mathbf{P}_k^-\mathbf{H}_k^T)^T) + \mathbf{K}_k(\mathbf{R}+\mathbf{R}^T).$$

The covariance matrix is positive-definite, so $\mathbf{M} = \mathbf{M}^T$. Therefore,

$$-2\mathbf{P}_k^-\mathbf{H}_k^T + 2\mathbf{K}_k(\mathbf{H}_k\mathbf{P}_k^-\mathbf{H}_k^T + \mathbf{R}) = \mathbf{0},$$

$$\mathbf{K}_k(\mathbf{H}_k\mathbf{P}_k^-\mathbf{H}_k^T + \mathbf{R}) = \mathbf{P}_k^-\mathbf{H}_k^T.$$

Then, the Kalman gain which results in the optimal estimation in the MMSE sense is given by

$$\mathbf{K}_k = \mathbf{P}_k^-\mathbf{H}_k^T\left[\mathbf{H}_k\mathbf{P}_k^-\mathbf{H}_k^T + \mathbf{R}_k\right]^{-1}. \tag{3.17}$$

Such Kalman gain matrix is considered in the *a posteriori* state error covariance matrix as already shown

$$\mathbf{P}_k^+ = \left[\mathbf{I}-\mathbf{K}_k\mathbf{H}_k\right]\mathbf{P}_k^-\left[\mathbf{I}-\mathbf{K}_k\mathbf{H}_k\right]^T + \mathbf{K}_k\mathbf{R}_k\mathbf{K}_k^T. \tag{3.18}$$

Then, substituting the optimal Kalman gain definition into the equation of $\mathbf{P}^+$, the following simplification will be achieved as

$$\mathbf{P}_k^+ = [\mathbf{I} - \mathbf{K}_k\mathbf{H}_k]\,\mathbf{P}_k^-. \tag{3.19}$$

Finally, the optimal estimation of the state vector is computed by

$$\hat{\mathbf{x}}_k^+ = \hat{\mathbf{x}}_k^- + \mathbf{K}_k(\tilde{\mathbf{y}}_k - \mathbf{H}_k\hat{\mathbf{x}}_k^-). \tag{3.20}$$

The filter is initialized again in the prediction stage for the next time instant, recursively.

An important characteristic of the Kalman filter is the Orthogonality Principle. In (CRASSIDIS; JUNKINS, 2012) it is stated that the state vector estimate and the state error are orthogonals, which can be written as

$$E\left\{\tilde{\mathbf{x}}_k\hat{\mathbf{x}}_k\right\} = \mathbf{0}, \tag{3.21}$$

that is, the error is uncorrelated to the estimate. From a least-squares (LS) point of view, the filter generates the optimal estimate in which the error is minimum (CRASSIDIS; JUNKINS, 2012; BAR-SHALOM *et al.*, 2002).

The Kalman Filter was formulated for linear systems with Gaussian noises, for which it gives the optimal state estimation. For nonlinear systems, a series of approaches are proposed in the literature. The most common solutions are the extended Kalman filter and the unscented Kalman filter, a type of sigma-point filter.

3.2 EXTENDED KALMAN FILTER

The Extended Kalman Filter (EKF) is an approach for estimation of nonlinear systems using the structure of the linear Kalman filter. The EKF is based on the first-order linearization of the dynamic system related functions and the algorithm will provide a sub-optimal solution for the state estimate. Consider the following discrete-time dynamic system given by

$$\begin{aligned} \mathbf{x}_k &= \mathbf{f}(\mathbf{x}_{k-1}, \mathbf{u}_{k-1}, \mathbf{w}_{k-1}, k-1), \\ \mathbf{y}_k &= \mathbf{h}(\mathbf{x}_k, \mathbf{v}_k, k-1), \end{aligned} \tag{3.22}$$

where $\mathbf{f}(\cdot) \in \mathbb{R}^{n\times n}$ is the nonlinear dynamic system function and $\mathbf{h}(\cdot) \in \mathbb{R}^{m\times n}$ is the nonlinear measurement function (LEFFERTS *et al.*, 1982). All remaining variables are defined as in the case of the linear system.

The linearization is based on the Taylor series expansion which states that any function can be expressed by an infinite sum of polynomials compound with the function's derivatives (CRASSIDIS; JUNKINS, 2012). Regarding the nonlinear dynamic system, a linear approximation of first order around a nominal state $\bar{\mathbf{x}}$ is given by

$$\mathbf{f}(\mathbf{x}(t), t) \approx \mathbf{f}(\bar{\mathbf{x}}(t), t) + \left.\frac{\partial \mathbf{f}(\mathbf{x}, t)}{\partial \mathbf{x}}\right|_{\bar{\mathbf{x}}(t)} (\mathbf{x}(t) - \bar{\mathbf{x}}(t)). \tag{3.23}$$

Denoting the state transition matrix derivatives as follow

$$\mathbf{F}(\mathbf{x}, t) = \left.\frac{\partial \mathbf{f}(\mathbf{x}, t)}{\partial \mathbf{x}}\right|_{\mathbf{x}(t_k)}, \tag{3.24}$$

one gets the Jacobian matrix $\mathbf{F}(\mathbf{x}, t)$. Then, the state equation is

$$\Delta\dot{\mathbf{x}}(t) = \mathbf{F}(t)\Delta\mathbf{x}(t) + \mathbf{G}(t)\mathbf{w}(t). \tag{3.25}$$

Considering the same process for the observation model, the linear approximation is given by

$$\mathbf{h}(\mathbf{x}(t), t) \approx \mathbf{h}(\bar{\mathbf{x}}(t), t) + \left.\frac{\partial \mathbf{h}(\mathbf{x}, t)}{\partial \mathbf{x}}\right|_{\bar{\mathbf{x}}(t)} (\mathbf{x}(t) - \bar{\mathbf{x}}(t)), \tag{3.26}$$

and the measurement function derivatives can be denoted by

$$\mathbf{H}(\mathbf{x}, t) = \left.\frac{\partial \mathbf{h}(\mathbf{x}, t)}{\partial \mathbf{x}}\right|_{\mathbf{x}(t_k)}, \tag{3.27}$$

with $\mathbf{H}(\mathbf{x}, t)$ being the Jacobian matrix of the observation model, which is also called measurement sensitivity matrix.

Finally, with the linear approximation of both models, the state error covariance matrix and the Kalman gain can be computed as the same in the linear filter. Figure 3.1 presents the EKF workflow.

3.2.1 Multiplicative Extended Kalman Filter

The quaternion is widely used for attitude representation due to the advantages previously presented. However, such parameter set has a unit norm constraint, which may not be satisfied in the state update equation where there is an additive term of the innovation. In order to preserve the quaternion unit norm in the Kalman filter with no brute normalization, a

Figure 3.1. Extended Kalman Filter Structure.

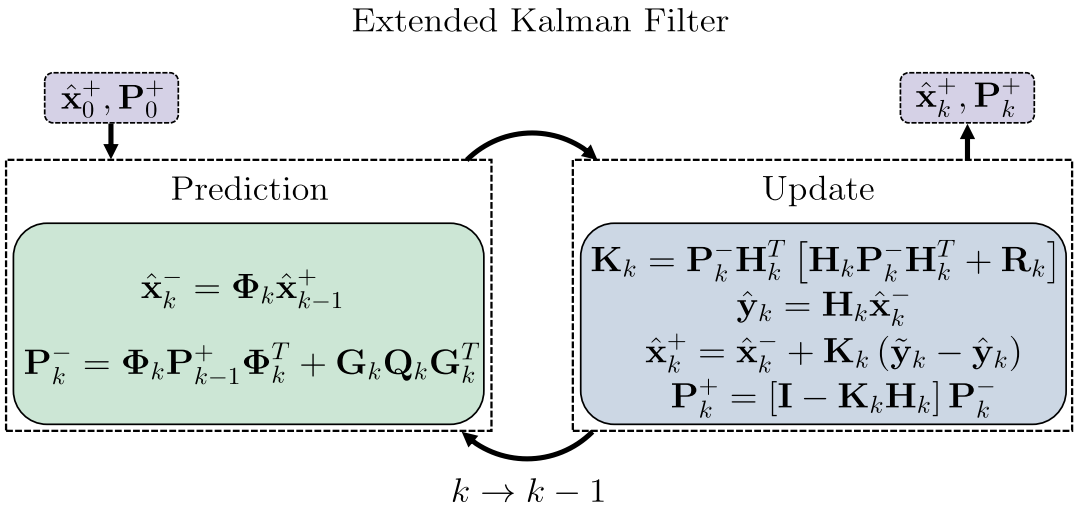

Source: Author.

multiplicative formulation was proposed in literature (FARRENKOPF, 1978; LEFFERTS *et al.*, 1982).

In the multiplicative approach, the global or absolute attitude is represented by a quaternion while a three-parameter set is used for the local attitude representation (MARKLEY, 2003). In this case, the spacecraft pose is defined as

$$\mathbf{q}^{true} = \delta\mathbf{q}(\boldsymbol{\xi}) \otimes \hat{\mathbf{q}}, \tag{3.28}$$

in which $\boldsymbol{\xi}$ is any three-parameter representation, such as the Rodrigues Parameters, Gibbs vector or rotation vector, $\mathbf{q}^{true}$ is the true unknown quaternion and $\hat{\mathbf{q}}$ is the estimated one. The quaternion multiplication operation denoted by $\otimes$ preserves the unit norm when the operands are also unit norm quaternions (MARKLEY *et al.*, 2005).

Concerning the filtering problem, the global attitude representation is propagated in time with the rotational motion equations while the EKF is used for the local attitude estimation. An attitude-error formulation is considered in which a small deviation or rotation is estimated, transformed into a quaternion and the global one is updated (MARKLEY, 2003). It is important to mention that the three-parameter representations as cited above have no norm constraint which make them suitable for the Kalman filter.

This formulation is called Multiplicative Extended Kalman Filter (MEKF). The attitude

error representation is denoted by $\boldsymbol{\vartheta}(t)$ and the equivalent quaternion is defined by

$$\delta\mathbf{q} \equiv \begin{bmatrix} \delta\boldsymbol{\varrho} & \delta q_4 \end{bmatrix}^T, \tag{3.29}$$

where the $\delta\mathbf{q}$ is also called error-quaternion and for small rotations, one gets the following relation

$$\delta\boldsymbol{\varrho} \approx \frac{\delta\boldsymbol{\vartheta}}{2}. \tag{3.30}$$

In Markley & Crassidis (2014) the attitude-error kinematics is developed. As a result such model is given by

$$\dot{\boldsymbol{\vartheta}}(t) = -\left[\hat{\boldsymbol{\omega}}\times\right]\boldsymbol{\vartheta}(t) + \delta\boldsymbol{\omega}(t), \tag{3.31}$$

where $\hat{\boldsymbol{\omega}}$ is the estimated angular velocity vector and the angular rate error, $\delta\boldsymbol{\omega}$, is given as

$$\delta\boldsymbol{\omega} \equiv \boldsymbol{\omega}^{true} - \hat{\boldsymbol{\omega}}. \tag{3.32}$$

Considering the bias estimation error, which is

$$\Delta\boldsymbol{\beta} \equiv \boldsymbol{\beta}^{true} - \hat{\boldsymbol{\beta}}, \tag{3.33}$$

then, from the gyroscope measurement model, one gets

$$\delta\boldsymbol{\omega} = -\left(\Delta\boldsymbol{\beta} + \boldsymbol{\eta}_v\right). \tag{3.34}$$

For spacecraft attitude estimation there are two structures for the Kalman filter: the gyro-based and dynamics-based model. In the first case, the process model is the kinematics equation with the angular velocity provided by the gyroscope measurements. While in the second case, the process model is given by the dynamics equation and the angular velocity is estimated in the state vector (MARKLEY; CRASSIDIS, 2014).

In this work the process model will be given by gyro-based kinematics equation. The error-state vector to be estimated is defined by

$$\Delta\hat{\mathbf{x}}(t) = \begin{bmatrix} \delta\boldsymbol{\vartheta}(t) \\ \delta\boldsymbol{\beta}(t) \end{bmatrix}, \tag{3.35}$$

where $\delta\boldsymbol{\vartheta}$ is the small angle deviation and $\delta\boldsymbol{\beta}$ is the gyroscope bias.

The state transition matrix can be computed from the attitude-error kinematics equation as

$$\mathbf{F} = \begin{bmatrix} -[\hat{\boldsymbol{\omega}}\times] & -\mathbf{I}_{3\times3} \\ \mathbf{0}_{3\times3} & \mathbf{0}_{3\times3} \end{bmatrix}, \tag{3.36}$$

in which the estimated angular velocity vector is the measured one corrected by the estimated bias as

$$\hat{\boldsymbol{\omega}} = \tilde{\boldsymbol{\omega}} - \hat{\boldsymbol{\beta}}. \tag{3.37}$$

For small sampling period, the time propagation of the quaternion can be given by an approximation of power series (MARKLEY; CRASSIDIS, 2014). One gets a closed form equation for the discrete-time kinematics equation. From the continuous to discrete state matrix transform and the attitude kinematics for quaternion one gets

$$\exp\left\{\frac{1}{2}\Omega(\hat{\boldsymbol{\omega}})t\right\} = \sum_{k=0}^{\infty} \frac{\left[\frac{1}{2}\Omega(\hat{\boldsymbol{\omega}})t\right]^k}{k!} \tag{3.38}$$

$$= \sum_{k=0}^{\infty} \left\{ \frac{\left[\frac{1}{2}\Omega(\hat{\boldsymbol{\omega}})t\right]^{2k}}{(2k)!} + \frac{\left[\frac{1}{2}\Omega(\hat{\boldsymbol{\omega}})t\right]^{2k+1}}{(2k+1)!} \right\} \tag{3.39}$$

$$= \cos\left(\frac{1}{2}\|\hat{\boldsymbol{\omega}}\|t\right)\mathbf{I}_{4\times 4} + \frac{\sin\left(\frac{1}{2}\|\hat{\boldsymbol{\omega}}\|t\right)}{\|\hat{\boldsymbol{\omega}}\|}\Omega(\hat{\boldsymbol{\omega}}). \tag{3.40}$$

Then, the global attitude representation can be updated in time as

$$\hat{\mathbf{q}}_k^- = \bar{\Theta}(\hat{\boldsymbol{\omega}}_{k-1})\hat{\mathbf{q}}_{k-1}^+, \tag{3.41}$$

where

$$\bar{\Theta}(\hat{\boldsymbol{\omega}}_{k-1}) \equiv \begin{bmatrix} \cos\left(\frac{1}{2}\|\hat{\boldsymbol{\omega}}_{k-1}\|\Delta t\right)\mathbf{I}_{3\times 3} - \left[\hat{\Psi}_{k-1}^+\times\right] & \hat{\Psi}_{k-1}^+ \\ -\hat{\Psi}_{k-1}^{+\,T} & \cos\left(\frac{1}{2}\|\hat{\boldsymbol{\omega}}_{k-1}\|\Delta t\right) \end{bmatrix}, \tag{3.42}$$

with $\Delta t = t_k - t_{k-1}$ being the sampling period and

$$\hat{\Psi}_{k-1}^+ \equiv \sin\left(\frac{1}{2}\|\hat{\boldsymbol{\omega}}_{k-1}\|\Delta t\right)\frac{\hat{\boldsymbol{\omega}}_{k-1}}{\|\hat{\boldsymbol{\omega}}_{k-1}\|}. \tag{3.43}$$

For the defined state vector, the state transition matrix can also given through power series approximation as developed in (MARKLEY; CRASSIDIS, 2014). Such matrix has the following form

$$\boldsymbol{\Phi}(\hat{\boldsymbol{\omega}}_{k-1}) = \begin{bmatrix} \boldsymbol{\Phi}_{11} & \boldsymbol{\Phi}_{12} \\ \boldsymbol{\Phi}_{21} & \boldsymbol{\Phi}_{22} \end{bmatrix}, \tag{3.44}$$

where each sub-matrix is given by

$$\mathbf{\Phi}_{11} = \mathbf{I}_{3\times3} - [\hat{\boldsymbol{\omega}}_{k-1}\times] \frac{\sin\left(\|\hat{\boldsymbol{\omega}}_{k-1}\|\Delta t\right)}{\|\hat{\boldsymbol{\omega}}_{k-1}\|} + [\hat{\boldsymbol{\omega}}_{k-1}\times]^2 \frac{\{1-\cos\left(\|\hat{\boldsymbol{\omega}}_{k-1}\|\Delta t\right)\}}{\|\hat{\boldsymbol{\omega}}_{k-1}\|^2},$$

$$\mathbf{\Phi}_{12} = [\hat{\boldsymbol{\omega}}_{k-1}\times] \frac{\{1-\cos\left(\|\hat{\boldsymbol{\omega}}_{k-1}\|\Delta t\right)\}}{\|\hat{\boldsymbol{\omega}}_{k-1}\|^2} - \mathbf{I}_{3\times3}\Delta t - [\hat{\boldsymbol{\omega}}_{k-1}\times]^2 \frac{\{\|\hat{\boldsymbol{\omega}}_{k-1}\|\Delta t - \sin\left(\|\hat{\boldsymbol{\omega}}_{k-1}\|\Delta t\right)\}}{\|\hat{\boldsymbol{\omega}}_{k-1}\|^3},$$

$$\mathbf{\Phi}_{21} = \mathbf{0}_{3\times3},$$

$$\mathbf{\Phi}_{22} = \mathbf{I}_{3\times3}.$$

The process noise covariance matrix in continuous-time form can be defined with the gyroscope noise parameters as (MARKLEY; CRASSIDIS, 2014)

$$\mathbf{Q}(t) = \begin{bmatrix} \sigma_v^2\mathbf{I}_{3\times3} & \mathbf{0}_{3\times3} \\ \mathbf{0}_{3\times3} & \sigma_u^2\mathbf{I}_{3\times3} \end{bmatrix}, \tag{3.45}$$

and the related mapping matrix is

$$\mathbf{G}(t) = \begin{bmatrix} -\mathbf{I}_{3\times3} & \mathbf{0}_{3\times3} \\ \mathbf{0}_{3\times3} & \mathbf{I}_{3\times3} \end{bmatrix}, \tag{3.46}$$

The discrete-time equivalent process noise covariance matrix, $\mathbf{Q}_{k-1}$, can be computed following the development in (FARRENKOPF, 1978; MARKLEY; REYNOLDS, 2000), which will results in

$$\mathbf{Q}_{k-1} = \begin{bmatrix} (\sigma_v^2\Delta t + \frac{1}{3}\sigma_u^2\Delta t^3)\mathbf{I}_{3\times3} & -(\frac{1}{2}\sigma_u^2\Delta t^2)\mathbf{I}_{3\times3} \\ -(\frac{1}{2}\sigma_u^2\Delta t^2)\mathbf{I}_{3\times3} & (\sigma_u^2\Delta t)\mathbf{I}_{3\times3} \end{bmatrix}, \tag{3.47}$$

The state vector and error covariance matrix are updated following the prediction phase of the Linear Kalman filter.

Next, the observation model which will provide the predicted output is given by

$$\hat{\mathbf{y}}_k = \begin{bmatrix} A(\mathbf{q}_k^-)\mathbf{r}_1 \\ A(\mathbf{q}_k^-)\mathbf{r}_2 \\ \vdots \\ A(\mathbf{q}_k^-)\mathbf{r}_n \end{bmatrix}. \tag{3.48}$$

For the computing of the Kalman gain and the covariance update, the measurement sensitivity matrix $\mathbf{H}_k$ must be found. The attitude matrix built from angle rotation is

$$A(\delta\mathbf{q}(\delta\boldsymbol{\vartheta})) \approx \mathbf{I}_{3\times3} - [\delta\boldsymbol{\vartheta}\times] - \frac{1}{2}(\|\delta\boldsymbol{\vartheta}\|^2\mathbf{I}_{3\times3} - \delta\boldsymbol{\vartheta}\delta\boldsymbol{\vartheta}^T), \tag{3.49}$$

in which the second-order term and higher can be neglected.

From the quaternion multiplication equation, the related attitude matrix is given by

$$A(\mathbf{q}^{ref}) = A(\delta\mathbf{q}(\delta\boldsymbol{\vartheta}))A(\hat{\mathbf{q}}^{-}). \tag{3.50}$$

Let $\mathbf{r}$ be a measurement vector described in a reference frame, then such vector in the spacecraft body frame is computed as

$$\mathbf{b}^{ref} = A(\mathbf{q}^{ref})\mathbf{r}, \tag{3.51}$$

$$\hat{\mathbf{b}}^{-} = A(\hat{\mathbf{q}}^{-})\mathbf{r}. \tag{3.52}$$

The deviation in the body frame vector is then

$$\Delta\mathbf{b} \equiv \mathbf{b}^{ref} - \hat{\mathbf{b}}^{-} = -\left[\delta\boldsymbol{\vartheta}\times\right] A(\hat{\mathbf{q}}^{-})\mathbf{r} = \left[\hat{\mathbf{b}}^{-}\times\right]\delta\boldsymbol{\vartheta}. \tag{3.53}$$

Following that, the observation sensitivity matrix is defined as

$$\mathbf{H}_k = \begin{bmatrix} A(\mathbf{q}_k^{-})[\mathbf{r}_1\times] \\ A(\mathbf{q}_k^{-})[\mathbf{r}_2\times] \\ \vdots \\ A(\mathbf{q}_k^{-})[\mathbf{r}_n\times] \end{bmatrix}. \tag{3.54}$$

After the computing of the *a posteriori* state vector, the global attitude quaternion is updated through the multiplication with the quaternion-error defined as

$$\delta\mathbf{q}(\delta\boldsymbol{\vartheta}) = \frac{1}{\sqrt{4+\delta\boldsymbol{\vartheta}^2}}\begin{bmatrix}\delta\boldsymbol{\vartheta} \\ 2\end{bmatrix}, \tag{3.55}$$

and the gyroscope bias is also updated by

$$\hat{\boldsymbol{\beta}}_k^{+} = \hat{\boldsymbol{\beta}}_{k-1}^{+} + \delta\hat{\boldsymbol{\beta}}_k. \tag{3.56}$$

Finally, the state vector is reset, that is, $\Delta\hat{\mathbf{x}} = \mathbf{0}$, and another iteration is executed. Table 3.1 summarizes the MEKF equations and the workflow.

3.3 UNSCENTED KALMAN FILTER

This method is based on the Unscented Transform (UT), which approximates a non-linear function by a set of points in the state-space according to a probability density function, usually

Table 3.1. MEKF algorithm steps.

Initialization	$\hat{\mathbf{q}}_0 = \mathbf{q}_0$, $\hat{\mathbf{x}}_0^+ = \mathbf{0}$, $\mathbf{P}_0^+ = \mathbf{P}_0$, $\hat{\boldsymbol{\beta}}_0 = \boldsymbol{\beta}_0$
Propagation	$\hat{\boldsymbol{\omega}}_{k-1} = \tilde{\boldsymbol{\omega}}_{k-1} - \hat{\boldsymbol{\beta}}_{k-1}$ $\hat{\mathbf{q}}_k^- = \bar{\Theta}(\hat{\boldsymbol{\omega}}_{k-1})\hat{\mathbf{q}}_{k-1}^+$ $\hat{\mathbf{x}}_k^- = \boldsymbol{\Phi}_{k-1}\hat{\mathbf{x}}_{k-1}^+$ $\mathbf{P}_k^- = \boldsymbol{\Phi}_{k-1}\mathbf{P}_{k-1}^+\boldsymbol{\Phi}_{k-1}^T + \mathbf{G}_{k-1}\mathbf{Q}_{k-1}\mathbf{G}_{k-1}^T$
Update	$\mathbf{H}_k = \begin{bmatrix} A(\mathbf{q}_k^-)[\mathbf{r}_1\times] \\ A(\mathbf{q}_k^-)[\mathbf{r}_2\times] \\ \vdots \\ A(\mathbf{q}_k^-)[\mathbf{r}_n\times] \end{bmatrix}$ $\mathbf{K}_k = \mathbf{P}_k^-\mathbf{H}_k^T\left[\mathbf{H}_k\mathbf{P}_k^-\mathbf{H}_k^T + \mathbf{R}_k\right]^{-1}$ $\hat{\mathbf{y}}_k = \begin{bmatrix} A(\mathbf{q}_k^-)\mathbf{r}_1 \\ A(\mathbf{q}_k^-)\mathbf{r}_2 \\ \vdots \\ A(\mathbf{q}_k^-)\mathbf{r}_n \end{bmatrix}$ $\hat{\mathbf{x}}_k^+ = \hat{\mathbf{x}}_k^- + \mathbf{K}_k(\tilde{\mathbf{y}}_k - \hat{\mathbf{y}}_k)$ $\mathbf{P}_k^+ = \left[\mathbf{I} - \mathbf{K}_k\mathbf{H}_k\right]\mathbf{P}_k^-$ $\hat{\mathbf{q}}_k^+ = \delta\hat{\mathbf{q}}(\delta\boldsymbol{\vartheta}) \otimes \hat{\mathbf{q}}_k^-$, $\hat{\boldsymbol{\beta}}_k^+ = \hat{\boldsymbol{\beta}}_{k-1}^+ + \delta\hat{\boldsymbol{\beta}}_k$
Reset	$\hat{\mathbf{x}}_k^+ = \mathbf{0}$

assumed Gaussian (JULIER; UHLMANN, 1997). That is, the UT provides the computing of a random variable statistics after a nonlinear transform operation.

Let $\mathcal{X}$ be an independent random variable with known first and second moments of the probability density function (p.d.f.), the dependent variable $\mathcal{Y}$ given by the nonlinear function $\mathbf{g}(\cdot)$ of $\mathcal{X}$ is defined as

$$\mathcal{Y} = \mathbf{g}(\mathcal{X}). \tag{3.57}$$

Taking the sample points $\{\mathcal{X}_i\}$ from the p.d.f of $\mathcal{X}$ through a deterministic rule, the expected value and variance of $\mathcal{Y}$ is given by:

$$E\{\mathcal{Y}\} = E\{\mathbf{g}(\mathcal{X}^i)\}, \tag{3.58}$$

$$Var\{\mathcal{Y}\} = Var\{\mathbf{g}(\mathcal{X}^i)\}. \tag{3.59}$$

That is, the expected value and variance of $\mathcal{Y}$ is given by a weighted average of the transformed sample points (JULIER; UHLMANN, 1997). Figure 3.2 presents the structure of the

UKF used by (CRASSIDIS; MARKLEY, 2003) for attitude filtering.

Figure 3.2. Uscented Kalman Filter Structure.

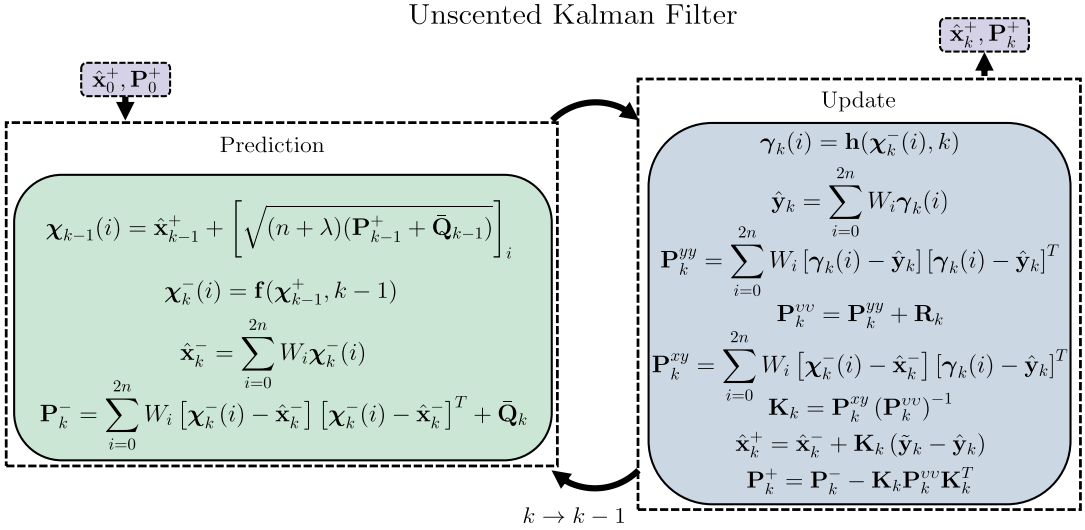

Source: Author.

3.3.1 Unscented Attitude Filter

The Unscented Quaternion Estimator (USQUE) is a filter based on the UT and also considers the multiplicative approach with respect to the attitude parameters. As for the MEKF, a global attitude represents the actual spacecraft pose while a local attitude parameter represents the attitude error. Such error will be estimated by the filter and it will correct the global representation after one iteration.

The local attitude-error quaternion, $\delta\mathbf{q}$, is represented using a vector of GRP. As stated in (CRASSIDIS; MARKLEY, 2003), when $f = 2(a+1)$ then $\|\delta\mathbf{p}\|$ is equivalent to $\delta\boldsymbol{\vartheta}$ for small errors. Therefore, the state vector is composed by the attitude error in GRP parameterization and the gyroscope biases, as expressed by

$$\hat{\mathbf{x}} \equiv \begin{bmatrix} \delta\mathbf{p} \\ \delta\boldsymbol{\beta} \end{bmatrix}. \tag{3.60}$$

The UT generates a set of points, called sigma-points, which are taken from the state vector's probability density function by a deterministic rule (JULIER; UHLMANN, 1997). Then, the $2n+1$ σ-points are generated from the state vector for $i = 0, \ldots, 2n$, with $n = 6$ being the

state dimension, as presented below

$$M = \begin{bmatrix} \mathbf{0} & S & -S \end{bmatrix}, \quad \text{where: } S = \sqrt{(n+\lambda)(\mathbf{P}^{+}_{k-1} + \bar{\mathbf{Q}}_{k-1})}, \tag{3.61}$$

where M is a matrix with each column is a σ-point deviation sample (MARKLEY, 2003). With the estimated state vector $\hat{\mathbf{x}}^{+}_{k-1}$ the σ-point vectors are given by

$$\begin{aligned} \boldsymbol{\chi}_{k-1}(i) &= M_i + \hat{\mathbf{x}}^{+}_{k-1}, \quad \text{and} \\ \boldsymbol{\chi}_{k-1}(0) &= \hat{\mathbf{x}}^{+}_{k-1}. \end{aligned} \tag{3.62}$$

Each σ-point is propagated in time using the process model. First, the GRP parameters are converted into quaternions, which have a closed form equation for the kinematics model (BATTISTINI *et al.*, 2016). A small angle in GRP can be converted to a quaternion such as

$$\delta\mathbf{q} = \begin{bmatrix} \delta\boldsymbol{\varrho} \\ \delta q_4 \end{bmatrix}, \tag{3.63}$$

where the GRP is related by

$$\delta\mathbf{p} = f\frac{\delta\boldsymbol{\varrho}}{a + \delta q_4}. \tag{3.64}$$

Then, the inverse transform to get the quaternion is given by

$$\delta q_4 = \frac{-a\|\delta\mathbf{p}|^2 + f\sqrt{f^2 + (1-a^2)\|\delta\mathbf{p}\|^2}}{f^2 + \|\delta\mathbf{p}\|^2}, \tag{3.65a}$$

$$\delta\boldsymbol{\varrho} = \frac{(a + \delta q_4)}{f}\delta\mathbf{p}. \tag{3.65b}$$

The full σ-points quaternions are obtained by the product of the estimate $\hat{\mathbf{q}}^{+}_{k-1}$ and the error quaternions converted from GRP, as

$$\hat{\mathbf{q}}^{+}_{k-1}(i) = \delta\mathbf{q}^{+}_{k-1}(i) \otimes \hat{\mathbf{q}}^{+}_{k-1}, \tag{3.66a}$$

$$\hat{\mathbf{q}}^{+}_{k-1}(0) = \hat{\mathbf{q}}^{+}_{k-1}, \tag{3.66b}$$

where $\boldsymbol{\delta}\mathbf{q}^{+}_{k} = \begin{bmatrix} \delta\boldsymbol{\varrho}^{+}_{k} & \delta q^{+}_{4} \end{bmatrix}^{T}$ is the attitude-error quaternion retrieved from the GRP.

The predicted state is obtained from the numeric integration of the attitude kinematic equation presented previously as $\boldsymbol{\chi}^{-}_{k}(i) = \mathbf{f}[\boldsymbol{\chi}_{k-1}(i), k]$.

The gyroscope measurements are used in the kinematic model and computed as $\hat{\boldsymbol{\omega}} = \tilde{\boldsymbol{\omega}} - \boldsymbol{\chi}^{\beta}_{k-1}(i)$, where $\hat{\boldsymbol{\omega}}$ is the estimated quantity, $\tilde{\boldsymbol{\omega}}$ the observed one and $\boldsymbol{\chi}^{\beta}_{k-1}(i)$ is the state vector part related to the bias estimation (MARKLEY, 2003).

After the σ-points propagation in time, the error quaternions are retrieved by

$$\delta\mathbf{q}_k^-(i) = \hat{\mathbf{q}}_k^-(i) \otimes \left[\hat{\mathbf{q}}_k^-\right]^{-1}, \tag{3.67}$$

where $\hat{\mathbf{q}}_k^- = \hat{\mathbf{q}}_k^-(0)$. The σ-points error-quaternions are converted back to GRP parameters.

Then, the mean state vector and mean covariance error matrix are computed as a weighted sample mean and covariance such as

$$\hat{\mathbf{x}}_k^- = \frac{1}{n+\lambda}\left\{\lambda\boldsymbol{\chi}_k^-(0) + \frac{1}{2}\sum_{i=1}^{2n}\boldsymbol{\chi}_k^-(i)\right\}, \tag{3.68}$$

and

$$\begin{aligned}\mathbf{P}_k^- =& \frac{1}{n+\lambda}\Bigg\{\lambda\left[\boldsymbol{\chi}_k^-(0) - \hat{\mathbf{x}}_k^-\right]\left[\boldsymbol{\chi}_k^-(0) - \hat{\mathbf{x}}_k^-\right]^T \\ &+ \frac{1}{2}\sum_{i=1}^{2n}\left[\boldsymbol{\chi}_k^-(i) - \hat{\mathbf{x}}_k^-\right]\left[\boldsymbol{\chi}_k^-(i) - \hat{\mathbf{x}}_k^-\right]^T\Bigg\} + \bar{\mathbf{Q}}_k.\end{aligned} \tag{3.69}$$

The discrete-time process error covariance matrix is derived in (MARKLEY, 2003) for high sample rate systems. They consider an approach similar to the trapezoidal rule for the integration which gives

$$\boldsymbol{\Phi}(\Delta t)\bar{\mathbf{Q}}_k\boldsymbol{\Phi}^T(\Delta t) + \bar{\mathbf{Q}}_k = \mathbf{G}_k\mathbf{Q}_k\mathbf{G}_k^T, \tag{3.70}$$

where $\boldsymbol{\Phi}(\Delta t)$ is the state transition matrix. The solution of the previous equation is given by (MARKLEY, 2003)

$$\bar{\mathbf{Q}}_k = \frac{\Delta t}{2}\begin{bmatrix}(\sigma_v^2 - \frac{1}{6}\sigma_u^2)\Delta t I_{3\times3} & 0_{3\times3} \\ 0_{3\times3} & \sigma_u^2\Delta t\end{bmatrix}. \tag{3.71}$$

In the correction phase, the mean predicted output is computed from the observation model as

$$\hat{\mathbf{y}}_k^- = \frac{1}{n+\lambda}\left\{\lambda\boldsymbol{\gamma}_k(0) + \frac{1}{2}\sum_{i=1}^{2n}\boldsymbol{\gamma}_k(i)\right\}, \tag{3.72}$$

where each σ-point is transformed by the observation function $\boldsymbol{\gamma}_k(i) = \mathbf{h}\left[\boldsymbol{\chi}_k(i), k\right]$.

The observation model for any vector measurement taken by a sensor is given by

$$\tilde{\mathbf{y}}_k = \begin{bmatrix}A(\mathbf{q})\mathbf{r}_1 \\ A(\mathbf{q})\mathbf{r}_2 \\ \vdots \\ A(\mathbf{q})\mathbf{r}_n\end{bmatrix} + \begin{bmatrix}\boldsymbol{\nu}_1 \\ \boldsymbol{\nu}_2 \\ \vdots \\ \boldsymbol{\nu}_n\end{bmatrix}, \tag{3.73}$$

where $A(\mathbf{q})$ is the rotation matrix from inertial to the body frame, $\mathbf{r}_i$ are reference vectors obtained from models and $\boldsymbol{\nu}_i$ is the measurement error associated to the i-th sensor. For the

predicted output, the matrix $A(\mathbf{q})$ is the attitude matrix built with the predicted quaternion from the prediction step. This is also the form of the observation function $\mathbf{h}(\cdot)$ when computing $\boldsymbol{\gamma}_k(i)$.

The output covariance matrix, $\mathbf{P}_k^{yy}$, the innovation covariance matrix, $\mathbf{P}_k^{\upsilon\upsilon}$, and the cross-correlation matrix, $\mathbf{P}_k^{xy}$, are computed as the equations below

$$\mathbf{P}_k^{yy} = \frac{1}{n+\lambda}\left\{\lambda\left[\boldsymbol{\gamma}_k(0)-\hat{\mathbf{y}}_k\right]\left[\boldsymbol{\gamma}_k(0)-\hat{\mathbf{y}}_k\right]^T + \frac{1}{2}\sum_{i=1}^{2n}\left[\boldsymbol{\gamma}_k(i)-\hat{\mathbf{y}}_k\right]\left[\boldsymbol{\gamma}_k(i)-\hat{\mathbf{y}}_k\right]^T\right\}, \tag{3.74}$$

$$\mathbf{P}_k^{\upsilon\upsilon} = \mathbf{P}_k^{yy} + \mathbf{R}_k, \tag{3.75}$$

$$\mathbf{P}_k^{xy} = \frac{1}{n+\lambda}\left\{\lambda\left[\boldsymbol{\chi}_k^-(0)-\hat{\mathbf{x}}_k^-\right]\left[\boldsymbol{\gamma}_k(0)-\hat{\mathbf{y}}_k\right]^T + \frac{1}{2}\sum_{i=1}^{2n}\left[\boldsymbol{\chi}_k^-(i)-\hat{\mathbf{x}}_k^-\right]\left[\boldsymbol{\gamma}_k(i)-\hat{\mathbf{y}}_k\right]^T\right\}. \tag{3.76}$$

With the covariance matrices, the Kalman gain can be obtained as

$$\mathbf{K}_k = \mathbf{P}_k^{xy}(\mathbf{P}_k^{\upsilon\upsilon})^{-1}. \tag{3.77}$$

The innovation is computed as the difference between the sensors observations and the predicted output

$$\boldsymbol{\upsilon}_k \equiv \tilde{\mathbf{y}}_k - \hat{\mathbf{y}}_k^- = \tilde{\mathbf{y}}_k - \mathbf{h}(\hat{\mathbf{x}}_k^-, k). \tag{3.78}$$

The final step is the state vector update with the innovation and the gain as for the error covariance matrix

$$\hat{\mathbf{x}}_k^+ = \hat{\mathbf{x}}_k^- + \mathbf{K}_k\boldsymbol{\upsilon}_k, \tag{3.79}$$

$$\mathbf{P}_k^+ = \mathbf{P}_k^- - \mathbf{K}_k\mathbf{P}_k^{\upsilon\upsilon}\mathbf{K}_k^T. \tag{3.80}$$

The attitude error is transformed to a quaternion and it is used to update the global attitude representation which is the new attitude estimate, as in the equation below,

$$\hat{\mathbf{q}}_k^+ = \delta\mathbf{q}_k^+ \otimes \hat{\mathbf{q}}_k^-. \tag{3.81}$$

Finally, the attitude-error in the state vector is set to zero (reset procedure) before the beginning of the next iteration. Table 3.2 presents the USQUE workflow, in which W_i are the sigma-points weights.

Table 3.2. USQUE algorithm steps.

Initialization	$\hat{\mathbf{q}}_0 = \mathbf{q}_0,\ \hat{\mathbf{x}}_0^+ = \mathbf{0},\ \mathbf{P}_0^+ = \mathbf{P}_0,\ \hat{\boldsymbol{\beta}}_0 = \boldsymbol{\beta}_0$
Propagation	$\boldsymbol{\chi}_{k-1}(i) = M_i + \hat{\mathbf{x}}_{k-1}^+ \Longrightarrow \delta\mathbf{q}_{k-1}^+(i)$ $\hat{\mathbf{q}}_{k-1}^+(i) = \delta\mathbf{q}_{k-1}^+(i) \otimes \hat{\mathbf{q}}_{k-1}^+$ $\hat{\boldsymbol{\omega}}_{k-1} = \tilde{\boldsymbol{\omega}}_{k-1} - \hat{\boldsymbol{\beta}}_{k-1}$ $\hat{\mathbf{q}}_k^-(i) = \bar{\Theta}(\hat{\boldsymbol{\omega}}_{k-1})\hat{\mathbf{q}}_{k-1}^+(i) \Longrightarrow \boldsymbol{\chi}_k^-(i)$ $\hat{\mathbf{x}}_k^- = \sum_{i=0}^{2n} W_i \boldsymbol{\chi}_k^-(i)$ $\mathbf{P}_k^- = \sum_{i=0}^{2n} W_i \left[\boldsymbol{\chi}_k^-(i) - \hat{\mathbf{x}}_k^-\right]\left[\boldsymbol{\chi}_k^-(i) - \hat{\mathbf{x}}_k^-\right]^T + \bar{\mathbf{Q}}_k$
Update	$\boldsymbol{\gamma}_k(i) = \begin{bmatrix} A(\mathbf{q}_k^-(i))\mathbf{r}_1 \\ A(\mathbf{q}_k^-(i))\mathbf{r}_2 \\ \vdots \\ A(\mathbf{q}_k^-(i))\mathbf{r}_n \end{bmatrix}$ $\hat{\mathbf{y}}_k = \sum_{i=0}^{2n} W_i \boldsymbol{\gamma}_k(i)$ $\mathbf{P}_k^{yy} = \sum_{i=0}^{2n} W_i \left[\boldsymbol{\gamma}_k(i) - \hat{\mathbf{y}}_k\right]\left[\boldsymbol{\gamma}_k(i) - \hat{\mathbf{y}}_k\right]^T$ $\mathbf{P}_k^{\upsilon\upsilon} = \mathbf{P}_k^{yy} + \mathbf{R}_k$ $\mathbf{P}_k^{xy} = \sum_{i=0}^{2n} W_i \left[\boldsymbol{\chi}_k^-(i) - \hat{\mathbf{x}}_k^-\right]\left[\boldsymbol{\gamma}_k(i) - \hat{\mathbf{y}}_k\right]^T$ $\mathbf{K}_k = \mathbf{P}_k^{xy}(\mathbf{P}_k^{\upsilon\upsilon})^{-1}$ $\hat{\mathbf{x}}_k^+ = \hat{\mathbf{x}}_k^- + \mathbf{K}_k(\tilde{\mathbf{y}}_k - \hat{\mathbf{y}}_k^-)$ $\mathbf{P}_k^+ = \mathbf{P}_k^- - \mathbf{K}_k\mathbf{P}_k^{\upsilon\upsilon}\mathbf{K}_k^T$ $\hat{\mathbf{q}}_k^+ = \delta\mathbf{q}_k^+ \otimes \hat{\mathbf{q}}_k^-, \quad \hat{\boldsymbol{\beta}}_k^+ = \hat{\boldsymbol{\beta}}_{k-1}^+ + \delta\hat{\boldsymbol{\beta}}_k$
Reset	$\hat{\mathbf{x}}_k^+ = \mathbf{0}$

CHAPTER 4

ADAPTIVE APPROACH FOR KALMAN FILTERING

After a spacecraft being launched in space the maintenance of its components is impracticable. Some platforms allows software corrective update or a reconfiguration of the subsystems parameters for the minimization of errors. Besides, the on-board sensors may have time-varying noise statistics or uncertain parameters. In such cases the mission may have a deteriorated operation or the satellite may be lost if the failure is critical. This chapter presents an adaptive strategy for attitude estimation which provide reliable satellite pose estimate in conditions such of change in sensor measurements statistics or unknown noise characteristics.

4.1 APPLICATIONS TO NOISE COVARIANCE MATRIX ESTIMATION

In order to the Kalman filter converges and provides the optimal estimate, it is necessary an accurate knowledge of the system *a priori* information, such as the dynamics model, disturbance influence and the noise statistics (MAYBECK, 1979; MYERS; TAPLEY, 1976; SAGE; HUSA, 1969). Mehra (1972) states that the use of wrong noise statistics may generate large estimation errors or the filter's divergence.

Small satellites' on-board sensors commonly are low cost, with no qualification or certification process for space applications. Therefore, the noise characteristics and the error modeling are not completely known. Due to such facts, the tuning of the process and measurement noise matrices is a challenging task (SOKEN; HACIZADE, 2019).

In general, stochastic errors may be the angle random walk, bias instability and rate random walk ,as examples. The deterministic errors are bias, misalignment and non-orthogonality. With such characterization it is possible to increase the estimation accuracy. To this end, the Allan Variance (AV) test is a commonly used method for noise identification (NARASIMHAPPA *et al.*, 2020).

In dynamics-based system model, several parameters must be considered for the process noise covariance definition. Frequently, small satellites inertia tensor are computed through Computer Aided Design (CAD) softwares which may not reflect the true parameters. Also, the disturbance torques must be known and they are not completely identifiable. The gravity-gradient perturbation depends on the inertia tensor and satellite position, the residual magnetic moment depends on the magnetic dipole value which may be time-varying. The aerodynamic torque is a function of the air density, the relative velocity with respect to the spacecraft and the effective area.

The application of adaptive filtering for estimation performance improvement have been widely investigated in the last decades (DUNÍK *et al.*, 2017). This is an approach considered for inertial navigation systems which also make use of gyroscopes and magnetometers, as the same for smallsats (CHIELLA *et al.*, 2019). Therefore, the attitude estimation problem can take advantage of such advances.

4.2 APPLICATION TO FAULT DETECTION, ISOLATION AND RECOVERY (FDIR)

In order to handle abnormal behaviour, spacecrafts have a Fault Detection, Isolation and Recovery (FDIR) system on-board. Also, an common approach that improves the spacecraft reliability and reduces the whole system failure is the use of redundant devices. The FDIR is responsible for the management of the equipment when an error occurs.

According to Gao *et al.* (2015), the fault diagnosis comprises three sequential functions. The first phase is the failure detection which is the recognition of a erroneous behaviour in a subsystem. After, the failure isolation is the process of identifying the faulty component and the type of error it is generating. Last, the failure recovery is the procedure for the normal condition restoration. It can be done by switching to redundant element, by a reset of the equipment or by ignoring the abnormal data.

Some sensors may suffer variation in their noise statistics as the temperature changes, which is the case of a LEO satellite when it is heated by the Sun or in eclipse. Such devices are prone to large stochastic errors and to the degradation from vibration and pressure levels (NARASIMHAPPA *et al.*, 2020). Besides, intense space weather phenomena may degrade the

sensor observations, for example when a magnetic storm occurs, the magnetometer may suffer interference. The exposure to radiation in-orbit also contributes to the change in the sensor's characteristics.

In all operations phase, the ADCS perform a critical role for the platform safety as such system can provide the Sun pointing function, once the Sun is the primary source of energy. In critical situations, the FDIR system can change the satellite's operations mode to what is commonly called safe (or survival) mode where only the strictly necessary subsystems are powered-on and a complete recovery process is executed. In this context, the attitude sensors play an important role and special attention is required.

4.3 ADAPTIVE KALMAN FILTERING

For a system to be tolerant against sensor faults, a stochastic fault diagnosis method in one of the solutions that can be considered for the implementation of this characteristic (GAO *et al.*, 2015). Furthermore, to be robust against time-varying disturbances and parameters, an identification method also must be used (MEHRA, 1970; DUNÍK *et al.*, 2017). Either way, an approach is to use Adaptive Kalman Filtering (AKF) which allows statistical tests for measurement assessment (GAO *et al.*, 2015). Differently from the traditional KF, in the adaptive method the filter parameters can be adjusted in order to improve the estimation accuracy (HAJIYEV; SOKEN, 2020).

The parameters that may be adapted are the process and measurement noise covariance matrices, $\mathbf{Q}$ and $\mathbf{R}$, respectively (MEHRA, 1972; MYERS; TAPLEY, 1976; SAGE; HUSA, 1969). This technique can reject disturbances and outliers present in the sensor's observations which increases the filter's robustness. As the space is a harsh and dynamic environment, low-cost sensors may suffer temporary disturbances or malfunctions along time (CHIELLA *et al.*, 2019).

A method for the adaptation of the system and observation noise covariance matrices is the Covariance Matching (CM) which is presented in (MEHRA, 1972). In such approach, the theoretical statistics of the innovations vector are compared to the innovations sequence statistics over time and then the noise covariance matrices are scaled in order to keep the filter's

accuracy.

4.4 COVARIANCE MATCHING TECHNIQUE

In the Kalman filter, the innovation process is defined as the difference between the measured observation vector and predicted output vector such as

$$\boldsymbol{\upsilon}_k \equiv \tilde{\mathbf{y}}_k - \hat{\mathbf{y}}_k, \tag{4.1}$$

and the innovation covariance is computed as

$$\begin{aligned} E\left\{\boldsymbol{\upsilon}_k \boldsymbol{\upsilon}_k^T\right\} &= E\left\{(\tilde{\mathbf{y}}_k - \hat{\mathbf{y}}_k)(\tilde{\mathbf{y}}_k - \hat{\mathbf{y}}_k)^T\right\}, \\ &= E\left\{(\mathbf{H}_k\mathbf{x}_k + \mathbf{v}_k - \mathbf{H}_k\hat{\mathbf{x}}_k^-)(\mathbf{H}_k\mathbf{x}_k + \mathbf{v}_k - \mathbf{H}_k\hat{\mathbf{x}}_k^-)^T\right\}, \\ &= E\left\{(\mathbf{H}_k\tilde{\mathbf{x}}_k^- + \mathbf{v}_k)(\mathbf{H}_k\tilde{\mathbf{x}}_k^- + \mathbf{v}_k)^T\right\}, \\ &= \mathbf{H}_k E\left\{\tilde{\mathbf{x}}_k^-\tilde{\mathbf{x}}_k^{-T}\right\}\mathbf{H}_k^T + E\left\{\mathbf{v}_k\mathbf{v}_k^T\right\}, \end{aligned}$$

with $E\left\{\tilde{\mathbf{x}}_k^-\mathbf{v}_k^T\right\} = E\left\{\mathbf{v}_k\tilde{\mathbf{x}}_k^{-T}\right\} = \mathbf{0}$. Therefore, the innovation covariance $\mathbf{S}_k$ is given by

$$\mathbf{S}_k = \mathbf{H}_k\mathbf{P}_k^-\mathbf{H}_k^T + \mathbf{R}_k. \tag{4.2}$$

Kailath (1968) states that a filter working optimally generates an innovations process which is characterized as a white noise random process. Therefore, the innovation's mean value is $E\{\boldsymbol{\upsilon}_k\} = \mathbf{0}$ and the covariance matrix is $\mathbf{S}_k$ (MEHRA, 1970).

Bar-Shalom *et al.* (2002) affirms that the innovation sequence is also an orthogonal sequence, in which there is no correlation between sample vectors. Such sequence is zero-mean and white. Besides, the innovation has the same information that the measurements (BAR-SHALOM *et al.*, 2002). A *whiteness test* of the innovation sequence can verify the filter's consistency and optimality.

4.5 ADAPTIVE EKF

In the EKF, both the process and measurement noise covariance matrices may be adapted according to the source of the change in the noise statistics. Once the designed filter uses the gyroscope measurements in the process model, the $\mathbf{Q}_k$ matrix is associated to the sensor behavior. In the following, the adaptation of each covariance matrix is presented.

4.5.1 Measurement noise Covariance Matrix Adaptation

In case of change in the statistical characteristics of a sensor, the analysis of the innovation sequence can provide means to detect such change and an adaptation of the measurement covariance matrix $\mathbf{R}$ may be performed in order to deal with the abnormal behavior. Let N be the number of samples in a moving window of the innovation sequence, then the innovation sequence covariance matrix is given by

$$\hat{\mathbf{C}}_{\upsilon_k} = \frac{1}{N} \sum_{j=k-N+1}^{k} \boldsymbol{\upsilon}_j \boldsymbol{\upsilon}_j^T, \tag{4.3}$$

in which the innovation vector is defined as

$$\boldsymbol{\upsilon}_k = \tilde{\mathbf{y}}_k - \mathbf{H}_k \hat{\mathbf{x}}_k^-. \tag{4.4}$$

However, the theoretical innovation covariance is given as

$$\mathbf{S}_k = \mathbf{H}_k \mathbf{P}_k^- \mathbf{H}_k^T + \mathbf{R}_k. \tag{4.5}$$

The innovation sequence covariance matrix, $\hat{\mathbf{C}}_{\upsilon_k}$, is the sample innovation process covariance. Then, one gets

$$\hat{\mathbf{C}}_{\upsilon_k} = \mathbf{H}_k \mathbf{P}_k^- \mathbf{H}_k^T + S(k)\mathbf{R}, \tag{4.6}$$

in which $S(k)$ is the multiple scale matrix that matches the innovation sequence and theoretical matrices. The solution for the scale factors is given by

$$S(k) = \left\{ \hat{\mathbf{C}}_{\upsilon_k} - \mathbf{H}_k \mathbf{P}_k^- \mathbf{H}_k^T \right\} \mathbf{R}^{-1}. \tag{4.7}$$

In order to guarantee that the measurement noise covariance matrix is a positive definite matrix, Hajiyev & Soken (2020) uses a diagonal matrix defined as

$$S^*(k) = diag(s_1^*, \ldots, s_m^*), \tag{4.8}$$

where the elements of the principal diagonal are the ones from multiple scale factors retrieved by the following rule

$$s_i^* = \max\left\{1, S_{ii}(k)\right\}, \quad for \quad i = 1, \ldots, m. \tag{4.9}$$

Therefore, the multiple scale factor matrix $S^*(k)$ is used to weight the observation noise matrix in order to the innovations sequence covariance matches its theoretical value. The

considering of the innovation sample covariance matrix by N and not $N-1$, which results in a biased estimate, is justified by the fact that it produces a smaller error (MEHRA, 1972).

4.5.2 Process Noise Covariance Matrix Adaptation

According to (MOHAMED; SCHWARZ, 1999), given the adaptive parameter α, the measurements conditional probability density function with respect to α is given by

$$p(y|\alpha) = \frac{1}{\sqrt{(2\pi)^m |\mathbf{C}_{\upsilon_k}|}} \exp\left\{-\frac{1}{2}\boldsymbol{\upsilon}_k^T \mathbf{C}_{\upsilon_k}^{-1} \boldsymbol{\upsilon}_k\right\}, \tag{4.10}$$

in which m is the number of measurements and $|\cdot|$ is the determinant operator.

The Maximum Likelihood Estimation (MLE) is used to find the adaptive parameter. The previous equation can be written as

$$\ln\{p(y|\alpha)\} = -\frac{1}{2}\left\{m\ln(2\pi) + \ln(|\mathbf{C}_{\upsilon_k}|) + \boldsymbol{\upsilon}_k^T \mathbf{C}_{\upsilon_k}^{-1} \boldsymbol{\upsilon}_k\right\}, \tag{4.11}$$

and by the MLE, the maximization of $p(y|\alpha)$ is the minimization of the right-side of the above equation (MOHAMED; SCHWARZ, 1999). Besides, the maximum likelihood as a function of the adaptive parameter is given by

$$\frac{\partial p(y|\alpha)}{\partial \alpha} = 0. \tag{4.12}$$

which gives (MAYBECK, 1979)

$$\sum_{j=0}^{k}\left[\mathrm{tr}\left\{\mathbf{C}_{\upsilon_j}^{-1}\frac{\partial \mathbf{C}_{\upsilon_j}}{\partial \alpha}\right\} - \boldsymbol{\upsilon}_j^T \mathbf{C}_{\upsilon_j}^{-1}\frac{\partial \mathbf{C}_{\upsilon_j}}{\partial \alpha}\mathbf{C}_{\upsilon_j}^{-1}\boldsymbol{\upsilon}_j\right] = 0. \tag{4.13}$$

The innovation covariance and its derivative as a function of $\mathbf{R}$ and $\mathbf{Q}$ is given as

$$\mathbf{C}_{\upsilon_k} = \mathbf{H}_k \mathbf{P}_k^- \mathbf{H}_k^T + \mathbf{R}_k, \tag{4.14a}$$

$$\frac{\partial \mathbf{C}_{\upsilon_k}}{\partial \alpha} = \mathbf{H}_k \frac{\partial \mathbf{P}_k^-}{\partial \alpha}\mathbf{H}_k^T + \frac{\partial \mathbf{R}_k}{\partial \alpha}. \tag{4.14b}$$

Substituting $\mathbf{P}_k^- = \boldsymbol{\Phi}(\hat{\boldsymbol{\omega}}_{k-1})\mathbf{P}_{k-1}^+\boldsymbol{\Phi}^T(\hat{\boldsymbol{\omega}}_{k-1}) + \mathbf{Q}_{k-1}$ and assuming the system in steady-state (MOHAMED; SCHWARZ, 1999), then

$$\frac{\partial \mathbf{P}_k^-}{\partial \alpha} = \frac{\partial \mathbf{Q}_{k-1}}{\partial \alpha}. \tag{4.15}$$

As a result the maximum likelihood expression for the adaptive approach is (MOHAMED; SCHWARZ, 1999)

$$\sum_{j=0}^{k} \left\{ \left[\mathbf{C}_{\upsilon_j}^{-1} - \mathbf{C}_{\upsilon_j}^{-1} \boldsymbol{\upsilon}_j \boldsymbol{\upsilon}_j^T \mathbf{C}_{\upsilon_j}^{-1} \right] \left[\mathbf{H}_j \frac{\partial \mathbf{Q}_{j-1}}{\partial \alpha} \mathbf{H}_j^T + \frac{\partial \mathbf{R}_j}{\partial \alpha} \right] \right\}. \tag{4.16}$$

in which $\alpha = \alpha_k$ is the adaptive parameter at instant k.

In order to find the solution for the above equation, Mohamed & Schwarz (1999) considers the measurement noise covariance matrix to be completely known and independent of the adaptive parameter. Also, considering $\alpha_i = Q_{ii}$, that is, the adaptive parameters are the process noise variances which one wants to estimate, it follows

$$\sum_{j=0}^{k} \left\{ \mathbf{H}_j \left[\mathbf{C}_{\upsilon_j}^{-1} - \mathbf{C}_{\upsilon_j}^{-1} \boldsymbol{\upsilon}_j \boldsymbol{\upsilon}_j^T \mathbf{C}_{\upsilon_j}^{-1} \right] \mathbf{H}_j^T \right\}. \tag{4.17}$$

Let the residual state vector be defined as the difference between the *a priori* and *a posteriori* estimation, that is

$$\Delta \mathbf{x}_k = \hat{\mathbf{x}}_k^+ - \hat{\mathbf{x}}_k^-. \tag{4.18}$$

From the Kalman filter update equation, one gets the following relation

$$\Delta \mathbf{x}_k = \mathbf{K}_k \boldsymbol{\upsilon}_k. \tag{4.19}$$

Considering the previous expressions, Mohamed & Schwarz (1999) derived the solution for the maximum likelihood problem. Then, the estimated process noise covariance matrix $\hat{\mathbf{Q}}_k$ is given by

$$\hat{\mathbf{Q}}_k = \frac{1}{N} \sum_{j=k-N+1}^{k} \Delta \mathbf{x}_j \Delta \mathbf{x}_j^T + \mathbf{P}_k^+ - \mathbf{P}_k^- + \mathbf{Q}_{k-1}, \tag{4.20}$$

in which $\mathbf{P}_k^- + \mathbf{Q}_{k-1} = \mathbf{F}_k \mathbf{P}_{k-1}^+ \mathbf{F}_k^T$ can be used equivalently.

In order to avoid abrupt changes in the $\mathbf{Q}$ matrix, which may causes the filter divergence, a low-pass filter can be considered as (HAJIYEV; SOKEN, 2020)

$$\mathbf{Q}_k = \eta \hat{\mathbf{Q}}_k + (1 - \eta) \mathbf{Q}_{k-1}, \tag{4.21}$$

in which $\eta \in [0,1]$ is a scale factor.

4.6 ADAPTIVE UKF

The adaptation method for the USQUE filter is analogous to the one presented for the EKF case. The main differences are in the definition of the noise covariance matrices due to the Unscented Transform.

4.6.1 Measurement Noise Covariance Matrix Adaptation

Similarly to the adaptation provided for the EKF, the USQUE algorithm considers the theoretical innovation covariance matrix as (HAJIYEV; SOKEN, 2020)

$$\mathbf{P}_k^{\upsilon\upsilon} = \mathbf{P}_k^{yy} + \mathbf{R}_k, \tag{4.22}$$

and the innovation sample sequence covariance as

$$\hat{\mathbf{C}}_{\upsilon_k} = \mathbf{P}_k^{yy} + S(k)\mathbf{R}. \tag{4.23}$$

Matching both covariance matrices through a multiple scale factors matrix, one gets

$$S(k) = \left\{\hat{\mathbf{C}}_{\upsilon_k} - \mathbf{P}_k^{yy}\right\}\mathbf{R}^{-1}. \tag{4.24}$$

In order to keep the adapted covariance matrix as a positive definite one, the used scale factors matrix $S^*(k)$ can be computed as the same for the EFK case. As before, the multiple scale factor matrix $S^*(k)$ is used to weight the observation noise matrix in order to the innovations sequence covariance matches its theoretical value.

4.6.2 Process Noise Covariance Matrix Adaptation

The expression for the process noise covariance matrix adaptation presented next can be found in (MOHAMED; SCHWARZ, 1999) and in (HAJIYEV; SOKEN, 2020) and it is demonstrated here for the understanding of the method. Following the derivation for the process noise adaptation described for the EKF, once the problem statement is independent of the filter structure, the relation below is also true for the UKF

$$\sum_{j=0}^{k}\left[\mathrm{tr}\left\{\mathbf{C}_{\upsilon_j}^{-1}\frac{\partial\mathbf{C}_{\upsilon_j}}{\partial\alpha}\right\} - \boldsymbol{\upsilon}_j^T\mathbf{C}_{\upsilon_j}^{-1}\frac{\partial\mathbf{C}_{\upsilon_j}}{\partial\alpha}\mathbf{C}_{\upsilon_j}^{-1}\boldsymbol{\upsilon}_j\right] = 0, \tag{4.25}$$

in which α is the adaptive parameter to be defined, $\boldsymbol{\upsilon}_k$ is the innovations vector at instant k and $\mathbf{C}_{\upsilon_k}$ is its covariance matrix.

However, in the linear Kalman filter, the cross-covariance is computed as

$$\begin{aligned} E\left\{(\mathbf{x}_k - \hat{\mathbf{x}}_k^-)(\tilde{\mathbf{y}}_k - \hat{\mathbf{y}}_k)^T\right\} &= E\left\{\tilde{\mathbf{x}}_k^-(\mathbf{H}_k\tilde{\mathbf{x}}_k^- + \mathbf{v}_k)^T\right\} \\ &= E\left\{\tilde{\mathbf{x}}_k^-\tilde{\mathbf{x}}_k^{-T}\right\}\mathbf{H}_k^T + E\left\{\tilde{\mathbf{x}}_k^-\mathbf{v}_k^T\right\} \\ &= \mathbf{P}_k^-\mathbf{H}_k^T, \end{aligned} \tag{4.26}$$

in which $E\left\{\tilde{\mathbf{x}}_k^-\mathbf{v}_k^T\right\} = \mathbf{0}$ and $\mathbf{H}_k$ is the measurement sensitivity matrix.

Once $\mathbf{P}_k^{xy} = E\left\{(\mathbf{x}_k - \hat{\mathbf{x}}_k^-)(\tilde{\mathbf{y}}_k - \hat{\mathbf{y}}_k)^T\right\}$, therefore, the state-output cross-covariance matrix is given by

$$\mathbf{P}_k^{xy} = \mathbf{P}_k^-\mathbf{H}_k^T. \tag{4.27}$$

Taking the relation above for the UKF structure, one gets the following measurement sensitivity matrix

$$\mathbf{H}_k = \left(\mathbf{P}_k^{xy}\right)^T\mathbf{P}_k^-. \tag{4.28}$$

Such result is discussed in Lefebvre *et al.* (2002), in which it stated that the UT is a Linear Regression Kalman Filter (LRKF), an estimator based on the approximation of nonlinear functions by statistical linear regression through points in the state-space.

As for the EKF, taking $\alpha_i = Q_{ii}$, which means that the adaptive parameters are the process noise variances which one wants to estimate, then the adaptation problem can be reduced to the following expression (MOHAMED; SCHWARZ, 1999; HAJIYEV; SOKEN, 2020)

$$\sum_{j=0}^{k}\left\{\mathbf{H}_j\left[\mathbf{C}_{\upsilon_j}^{-1} - \mathbf{C}_{\upsilon_j}^{-1}\boldsymbol{\upsilon}_j\boldsymbol{\upsilon}_j^T\mathbf{C}_{\upsilon_j}^{-1}\right]\mathbf{H}_j^T\right\}. \tag{4.29}$$

From the USQUE filter, one gets the following relation

$$\mathbf{P}_k^{\upsilon\upsilon} = \mathbf{P}_k^{yy} + \mathbf{R}_k. \tag{4.30}$$

For a moving window of N innovations vector samples, the innovations theoretical value is given by

$$\mathbf{C}_{\upsilon_k} = \mathbf{P}_k^{yy} + \mathbf{R}_k. \tag{4.31}$$

However, the output covariance matrix for the linear case is given by

$$\begin{aligned} E\left\{(\mathbf{y}_k - \hat{\mathbf{y}}_k)(\mathbf{y}_k - \hat{\mathbf{y}}_k)^T\right\} &= E\left\{(\mathbf{H}_k\mathbf{x}_k - \mathbf{H}_k\hat{\mathbf{x}}_k^-)(\mathbf{H}_k\mathbf{x}_k - \mathbf{H}_k\hat{\mathbf{x}}_k^-)^T\right\} \\ &= \mathbf{H}_k E\left\{\tilde{\mathbf{x}}_k^-\tilde{\mathbf{x}}_k^{-T}\right\}\mathbf{H}_k^T \\ &= \mathbf{H}_k\mathbf{P}_k^-\mathbf{H}_k^T, \end{aligned} \tag{4.32}$$

in which $\mathbf{y}_k$ is the true unknown observation vector and $\tilde{\mathbf{x}}_k^- = \mathbf{x}_k - \hat{\mathbf{x}}_k^-$. Therefore, the output covariance matrix is written as

$$\mathbf{P}_k^{yy} = \mathbf{H}_k\mathbf{P}_k^-\mathbf{H}_k^T. \tag{4.33}$$

Considering the definition of the sensitivity matrix for the UKF, one gets

$$\mathbf{P}_k^{yy} = \mathbf{P}_k^{xyT}\left(\mathbf{P}_k^-\right)^{-1}\mathbf{P}_k^{xy}. \tag{4.34}$$

Then, the innovation covariance becomes

$$\mathbf{C}_{\upsilon_k} = \mathbf{P}_k^{xyT}\left(\mathbf{P}_k^-\right)^{-1}\mathbf{P}_k^{xy} + \mathbf{R}_k, \tag{4.35}$$

and its derivative with respect to the adaptive parameter is

$$\frac{\partial\mathbf{C}_{\upsilon_k}}{\partial\alpha} = -\mathbf{P}_k^{xyT}\left(\mathbf{P}_k^-\right)^{-1}\frac{\partial\mathbf{Q}_k}{\partial\alpha}\left(\mathbf{P}_k^-\right)^{-1}\mathbf{P}_k^{xy} + \frac{\partial\mathbf{R}_k}{\partial\alpha}, \tag{4.36}$$

in which $\mathbf{P}_k^{xy}$ is not a function of α. Besides, taking $\mathbf{P}_k^- = \mathbf{P}_k^* + \mathbf{Q}_k$, where $\mathbf{P}_k^*$ is the state error covariance propagated without the additive process noise, then $\mathbf{P}_k^*$ is also independent of the adaptive parameter.

Considering the measurement noise covariance matrix as a completely known matrix and independent of α, one gets the following equation

$$\sum_{j=0}^{k}\left\{\left[\mathbf{C}_{\upsilon_j}^{-1} - \mathbf{C}_{\upsilon_j}^{-1}\boldsymbol{\upsilon}_j\boldsymbol{\upsilon}_j^T\mathbf{C}_{\upsilon_j}^{-1}\right]\left[\mathbf{H}_j\frac{-\partial\mathbf{Q}_{j-1}}{\partial\alpha}\mathbf{H}_j^T\right]\right\}. \tag{4.37}$$

Again, Mohamed & Schwarz (1999) derived the solution for the maximum likelihood problem. Then, the estimated process noise covariance matrix $\hat{\mathbf{Q}}_k$ is given by

$$\hat{\mathbf{Q}}_k = \frac{1}{N}\sum_{j=k-N+1}^{k}\Delta\mathbf{x}_j\Delta\mathbf{x}_j^T + \mathbf{P}_k^+ - \mathbf{P}_k^- + \mathbf{Q}_{k-1}. \tag{4.38}$$

In order to avoid abrupt changes in the $\mathbf{Q}$ matrix, which may causes the filter divergence, a low-pass filter can be considered as (HAJIYEV; SOKEN, 2020)

$$\mathbf{Q}_k = \eta\hat{\mathbf{Q}}_k + (1-\eta)\mathbf{Q}_{k-1}, \tag{4.39}$$

where $\eta \in [0,1]$ is a scale factor.

In such way, the process noise covariance matrix can be adapted by a multiple scale factors depending upon the innovation covariance. If the innovation covariance increases due to a disturbance, then the process noise matrix will be scaled in order to compensate the noise.

CHAPTER 5

MAIN RESULTS AND NUMERICAL ANALYSIS

This chapter presents the main results and simulations of small satellites in orbit along with the environment models and disturbance torques. In the first analysis, a set of on-board sensors is considered and the attitude estimation results are discussed. Also, the adaptive filtering is presented with simulated sensor's fault injection and disturbance. The second part of this chapter presents the proposed procedure for the AlfaCrux CubeSat mission control platform. Specifically, the data processing configuration and EKF results are evaluated along with an adaptation scheme.

5.1 NUMERICAL SIMULATION OF A SATELLITE MODEL

In this first case study, a simulated satellite is considered. The spacecraft position is defined by the SGP-4 model using the orbital parameters of the AlfaCrux Cubesat (BORGES *et al.*, 2022). The two-line elements (TLE) for the small satellite is the following one:

```
1 52160U 22033D   23174.00581841  .00034043  00000+0  96046-3 0  9999
2 52160  97.3553 255.9084 0008294 156.8196 203.3424 15.36288620 68227
```

From the TLE file, the following information related to the spacecraft orbit is retrieved

- TLE Epoch: 23 Jun 2023 00:08:22.711 UTC
- Period: 95 min;
- Inclination: 97.3553°;
- Apogee: 488 km;
- Perigee: 454 km.

The simulation of the true model is given by the following system

$$\begin{bmatrix} \dot{\mathbf{q}}(t) \\ \dot{\boldsymbol{\omega}}(t) \end{bmatrix} = \begin{bmatrix} \frac{1}{2}\Xi[\mathbf{q}(t)]\boldsymbol{\omega}(t) \\ \mathbf{J}^{-1}\left[\mathbf{T}_{gg} + \mathbf{T}_{rm} + \mathbf{T}_{aero} - \boldsymbol{\omega}(t) \times \mathbf{J}\boldsymbol{\omega}(t)\right] \end{bmatrix}, \tag{5.1}$$

in which the inertia tensor matrix for the attitude dynamics equation modeling was taken from Markley & Crassidis (2014) as

$$\mathbf{J} = \begin{bmatrix} 100 & 0 & 0 \\ 0 & 75 & 0 \\ 0 & 0 & 50 \end{bmatrix} kg \cdot m^2. \tag{5.2}$$

The initial true state vector of the smallsat is defined as

$$\mathbf{q}_0 = \begin{bmatrix} 0 & 0 & 0 & 1 \end{bmatrix}^T, \tag{5.3a}$$

$$\boldsymbol{\omega}_0 = \begin{bmatrix} 0.1 & 0.01 & 0.01 \end{bmatrix}^T \quad [rad/s]. \tag{5.3b}$$

For the simulation the main disturbance torques are the gravity-gradient, residual magnetic moment and the aerodynamics torque. For this case, the solar radiation pressure torque can be neglected due to its magnitude. The residual magnetic moment is

$$\mathbf{m}_{rm} = \begin{bmatrix} 0.1 & 0.5 & 0.3 \end{bmatrix}^T \times 10^{-3} \qquad [Am^2]. \tag{5.4}$$

The aerodynamics torque considers the distance between the spacecraft center-of-mass and the center-of-pressure which the value is given by

$$\mathbf{m}_{rm} = \begin{bmatrix} 0.05 & 0 & 0 \end{bmatrix}^T \qquad [m], \tag{5.5}$$

and the atmosphere density is given by the exponential model as (MARKLEY; CRASSIDIS, 2014)

$$\rho_{air}(h = 500km) = 1.6 \times 10^{-13} \qquad [kg/m^3]. \tag{5.6}$$

The drag coefficient commonly used value is $C_D = 2.2$ and the total effective area is $100 \times 10^{-4} m^2$. The sensors noise parameters used in the simulation are shown in Table 5.1. The chosen values are close to the ones found in the literature. The eclipse events were not simulated. Also, the Earth's Albedo is not considered in the simulation, therefore, the Sun sensors noise value was increased in order to account such disturbance.

The dynamics models were executed using the Runge-Kutta 4th/5th order and the samples were generated at every 0.5 seconds. The true quaternions are presented in Figure 5.1.

Table 5.1. Attitude Sensors Noise Parameters.

Sensor	Parameter	Value	Unit
Gyroscope	σ_v	10^{-6}	$(rad/s)\sqrt{Hz}$
	σ_u	10^{-10}	$(rad/s)/\sqrt{Hz}$
Magnetometer	σ_m	700	nT
Sun sensors	σ_s	5	$^\circ$

Figure 5.1. Satellite true quaternions.

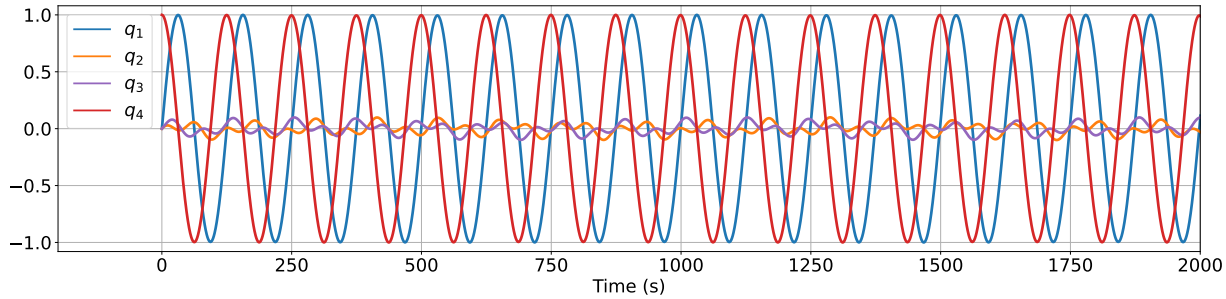

Source: Author.

The Earth's magnetic field generated by the IGRF-13 is presented in Figure 5.2 described in the ECI frame.

Figure 5.2. Earth magnetic field in ECI frame.

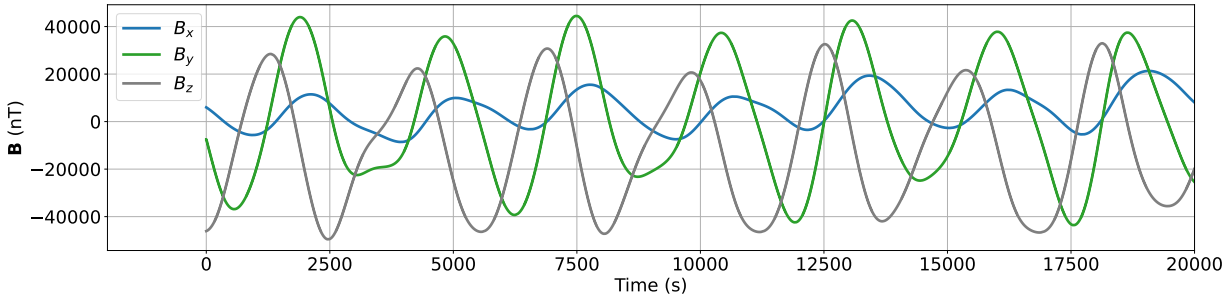

Source: Author.

And the Sun position model in ECI frame is shown in Figure 5.3.

Figure 5.3. Sun direction vector in ECI frame.

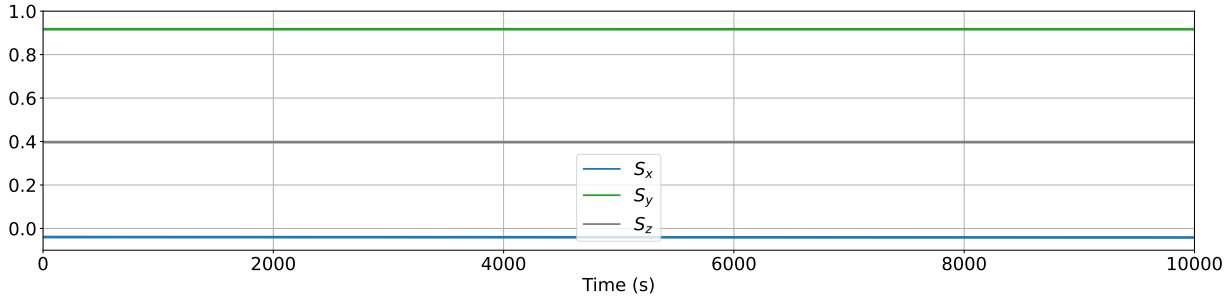

Source: Author.

The satellite position and velocity, along with the geomagnetic field and Sun position were all compared with the results from the software System Tool Kit (STK), developed by Ansys Government Initiatives (AGI), which is used in the aerospace industry. A difference of 5% on average were found between the variables, which indicates that such models are reliable solutions for the simulation purpose.

After the variables are given in the ECI frame, the measurements in body frame can be derived using the true quaternion. As result, in Figure 5.4 can be found the true angular velocity vector and the simulated measured one which is corrupted by the noise.

Figure 5.4. Satellite true angular rate.

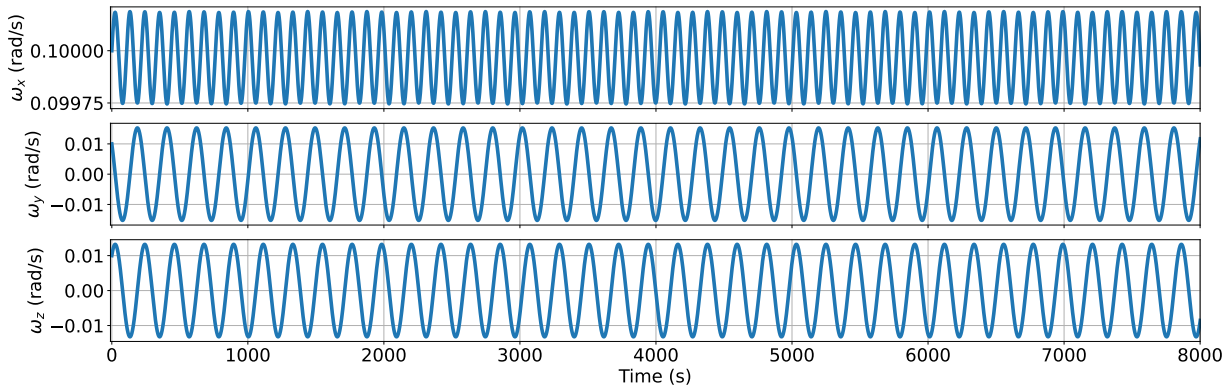

Source: Author.

The Figure 5.5 shows the Gaussian white noise which is added to the gyroscope bias.

Figure 5.5. Angular rate bias noise simulated data.

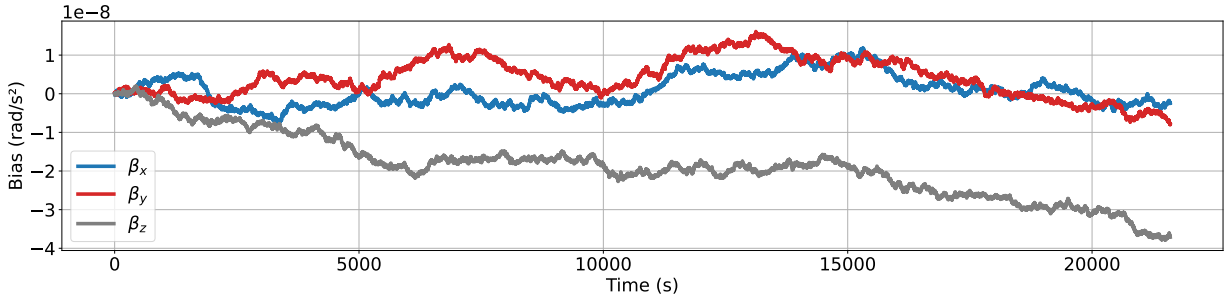

Source: Author.

Figure 5.6 and Figure 5.7 show the geomagnetic field and Sun direction vector in body frame, respectively. Both Figures present the true value and the sensor observation with noise.

Figure 5.6. Geomagnetic field in body frame simulated data.

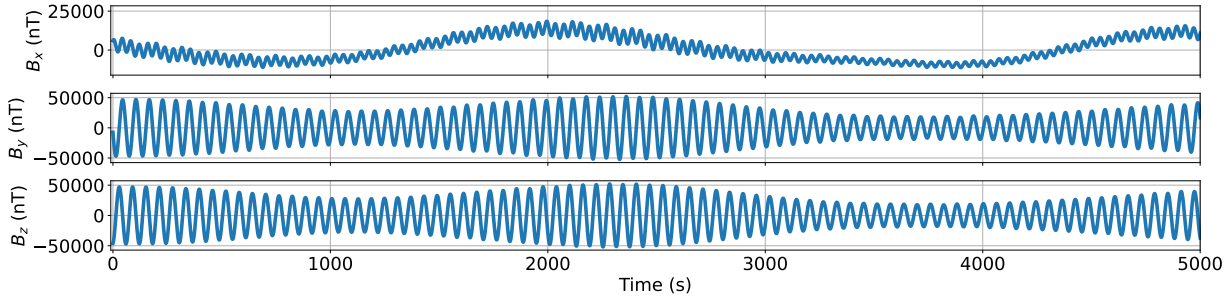

Source: Author.

Figure 5.7. Sun direction vector in body frame simulated data.

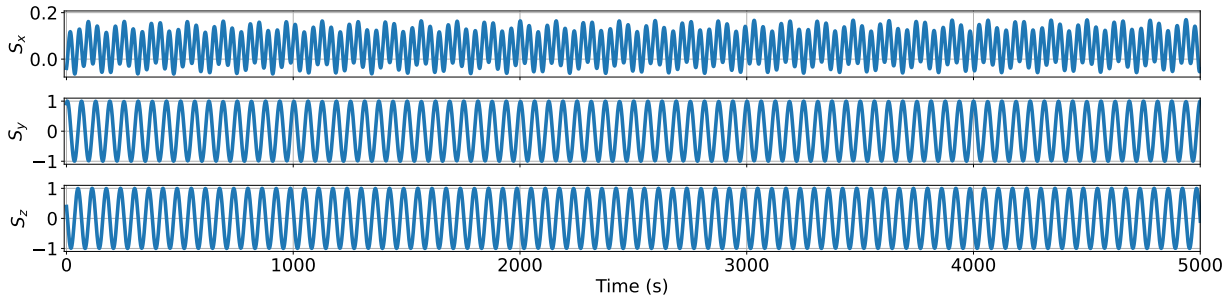

Source: Author.

5.1.1 Initial Conditions

The initial global quaternion is given as $\hat{\mathbf{q}}_0^+ = \begin{bmatrix} 0.01 & 0.01 & 0.01 & 0.99 \end{bmatrix}^T$. Also, the initial state error covariance matrix is given by $P_0 = diag(\begin{bmatrix} 10^{-2} & 10^{-2} & 10^{-2} & 10^{-12} & 10^{-12} & 10^{-12} \end{bmatrix})$. For the simulations, it will be considered the filter in steady-state.

The Kalman filters are parameterized with $\sigma_u = 10^{-10}\ rad/s^{3/2}$ and $\sigma_v = 10^{-6}\ rad/s^{1/2}$, which will be used for computing of the process noise covariance matrix, $\mathbf{Q}_k$. The measurement noise covariance matrix is given as $R = diag(\begin{bmatrix} 700^2 & 700^2 & 700^2 & (0.03)^2 & (0.03)^2 & (0.03)^2 \end{bmatrix})$.

For the filters performance assessment, it will be given by the angular error between the estimated and true attitudes. Both quaternions are related by

$$\mathbf{q}^{true} = \delta\mathbf{q}(\Delta\vartheta) \otimes \hat{\mathbf{q}}^+. \tag{5.7}$$

Then, the error-quaternion can be generated as

$$\delta\mathbf{q}(\Delta\vartheta) = \mathbf{q}^{true} \otimes \left[\hat{\mathbf{q}}^+\right]^{-1}, \tag{5.8}$$

and the error angle is given by

$$\Delta\vartheta = 2\arccos(\delta q_4). \tag{5.9}$$

besides the rotation angle error, from the error-quaternion it is possible to retrieve the Euler angles, which will be given in the $3-2-1$ rotation sequence, that is

$$A_{321}(\delta\mathbf{q}(\Delta\vartheta)) \longrightarrow \Delta\phi,\Delta\theta,\Delta\psi.$$

in which $A_{321}(\delta\mathbf{q}(\Delta\vartheta)) = A_{321}(\mathbf{q}^{true})A_{321}^{T}(\hat{\mathbf{q}}^{+})$.

5.1.2 MEFK

For the Multiplicative Extended Kalman filter, Figure 5.8 presents the state error covariance convergence when the estimator works with no disturbance.

Figure 5.8. EKF standard deviation of the rotation angle state vector.

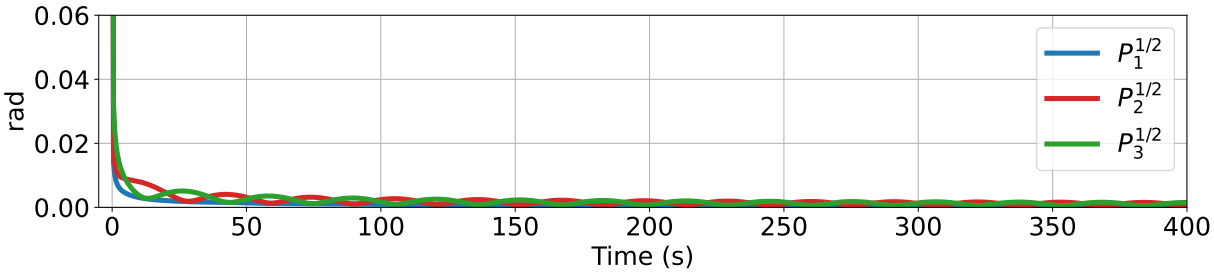

Source: Author.

The Euler angles and the error angle are shown in Figure 5.9 and Figure 5.10, respectively. In normal conditions, the MEKF provides an estimate with less than 1° of error.

5.1.3 USQUE

For the Unscented filter, Figure 5.11 presents the state error covariance convergence when the estimator works with no disturbance.

Analogous to the MEKF case, the Euler angles and the error angle are shown in Figure 5.12 and Figure 5.13, respectively. In normal conditions, the USQUE provides an estimate with less than 0.2° of error.

Figure 5.9. MEKF Euler angles error between the true and estimated quaternions.

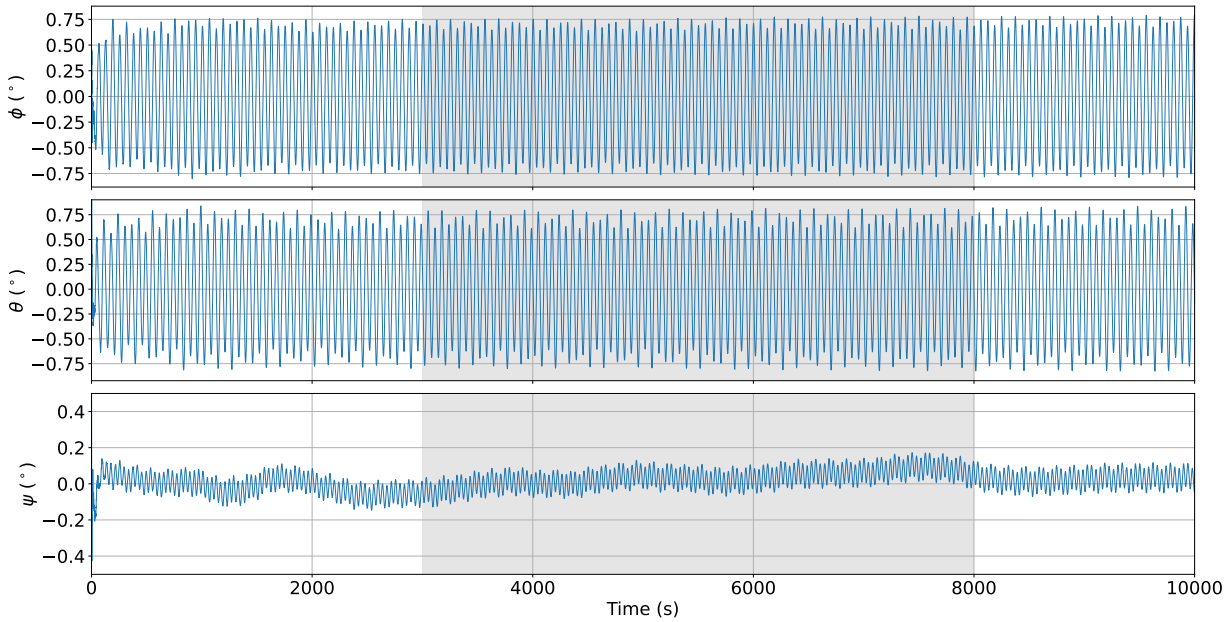

Source: Author.

Figure 5.10. MEKF true angle error.

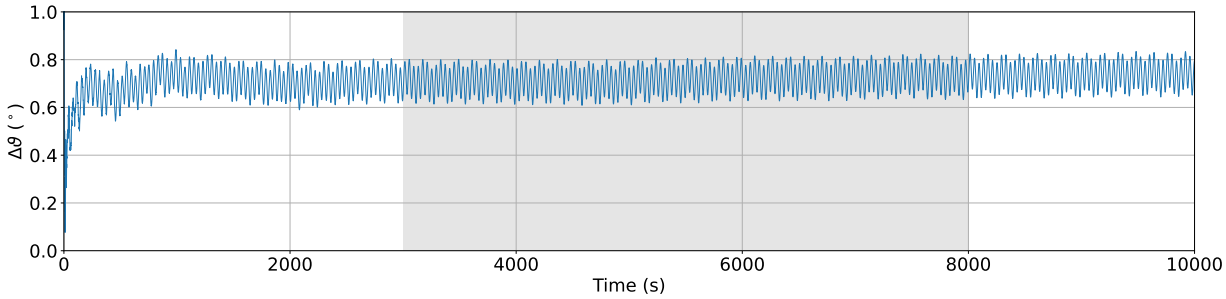

Source: Author.

Figure 5.11. USQUE standard deviation of the rotation angle state vector.

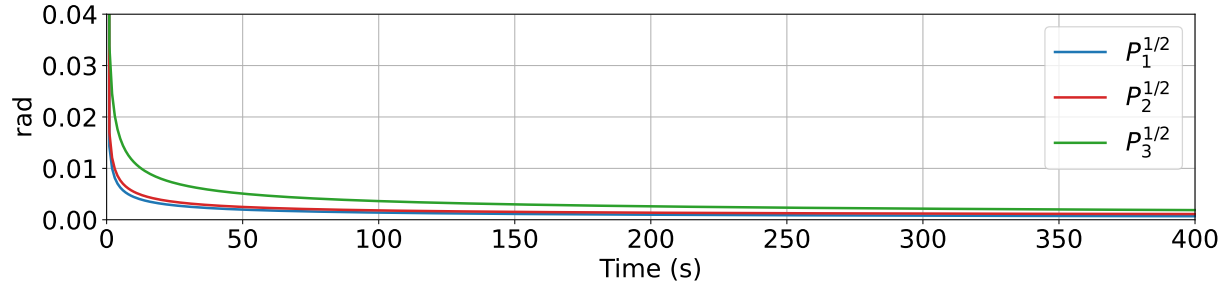

Source: Author.

5.1.4 Adaptive MEKF

In the adaptive MEKF, three cases of perturbations will be considered in order to evaluate the adaptation process performance in the attitude estimation. Both filters, with adaptation

Figure 5.12. USQUE Euler angles error between the true and estimated quaternions.

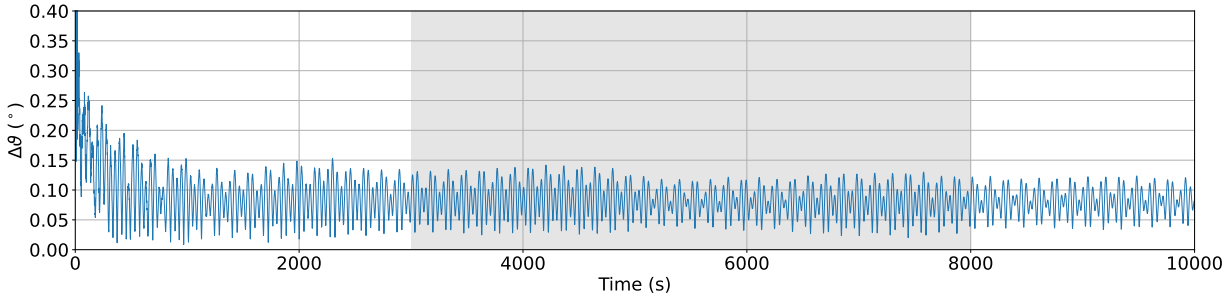

Source: Author.

Figure 5.13. USQUE estimated angle error.

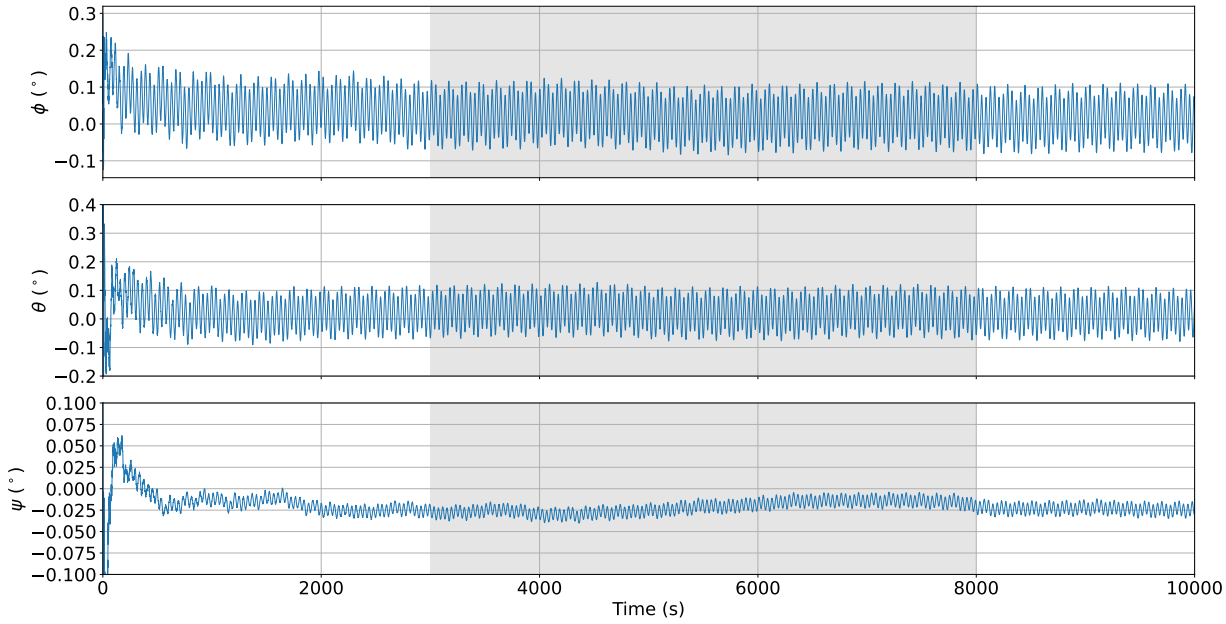

Source: Author.

and without the feature will be compared and the results discussed.

5.1.4.1 Magnetometer Noise Increase

In this simulation, the magnetometer noise suffered an increase of 100 times in its magnitude, changing the statistical characteristics. Figure 5.14 presents the angle error due to this disturbance. The increase of the noise level occurs in the gray area of the graphs and then the noise level return to its original value.

The Figure 5.15 shows the Euler angles error, where it is possible to see each individual contribution into the total error.

Figure 5.16 presents the angle error of the MEKF with the measurement noise covariance

Figure 5.14. MEKF angle error when noise level increase.

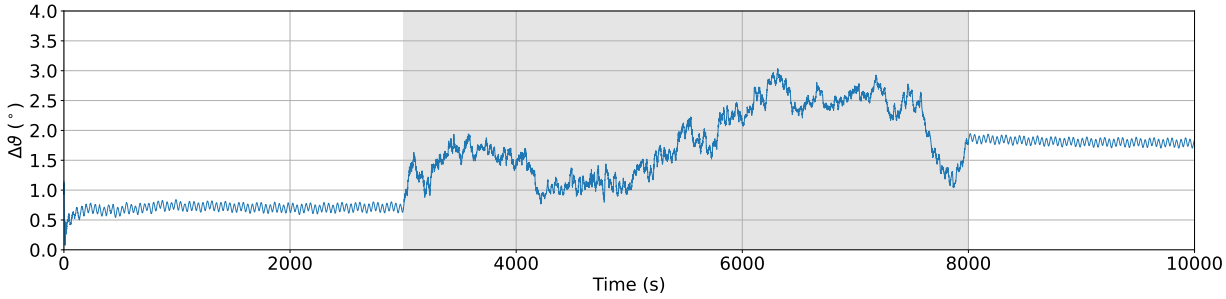

Source: Author.

Figure 5.15. MEKF Euler angles error when noise level increase.

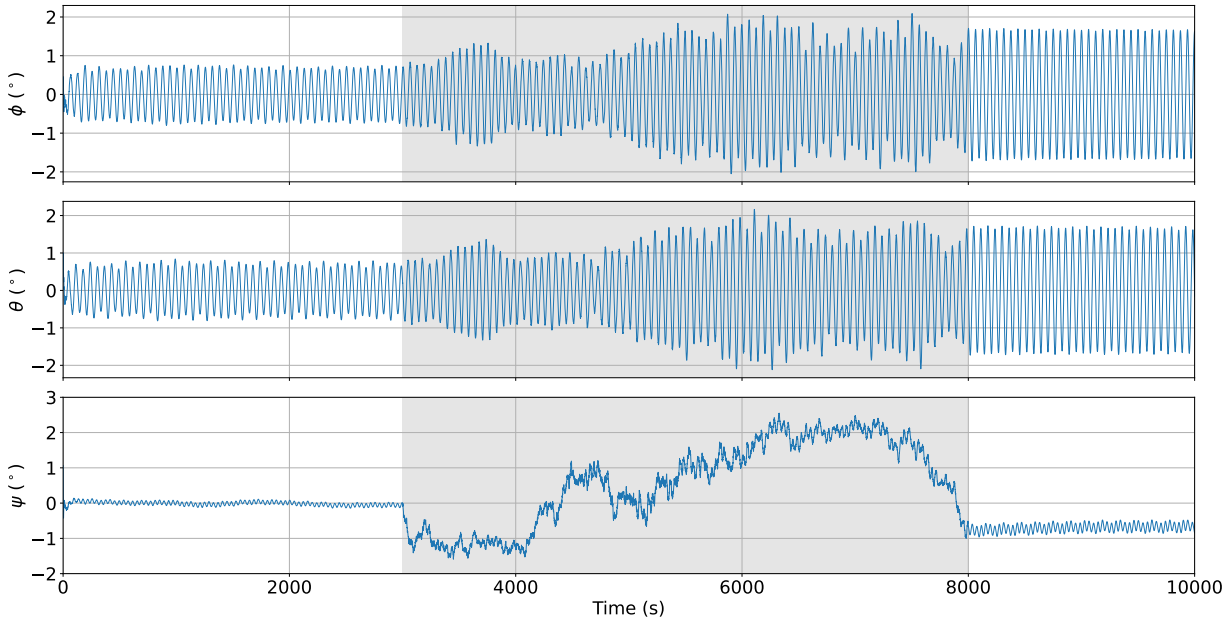

Source: Author.

matrix adaptation in which the sliding window is of 100 samples, where the sampling period is $500ms$. It is possible to verify the algorithm capability to accommodate the perturbation, that is, the magnetometer noise was scaled in a form that the measurements weight were lower than the nominal case, reducing its contribution to the estimation.

Figure 5.16. Adaptive MEKF angle error when noise level increase.

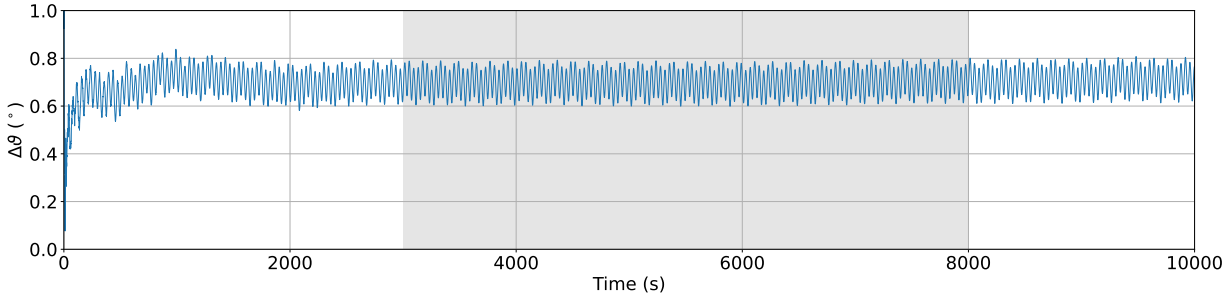

Source: Author.

In the Figure 5.17 the Euler angles errors are presented in which the curves are similar to the nominal case.

Figure 5.17. Adaptive MEKF Euler angles error when noise level increase.

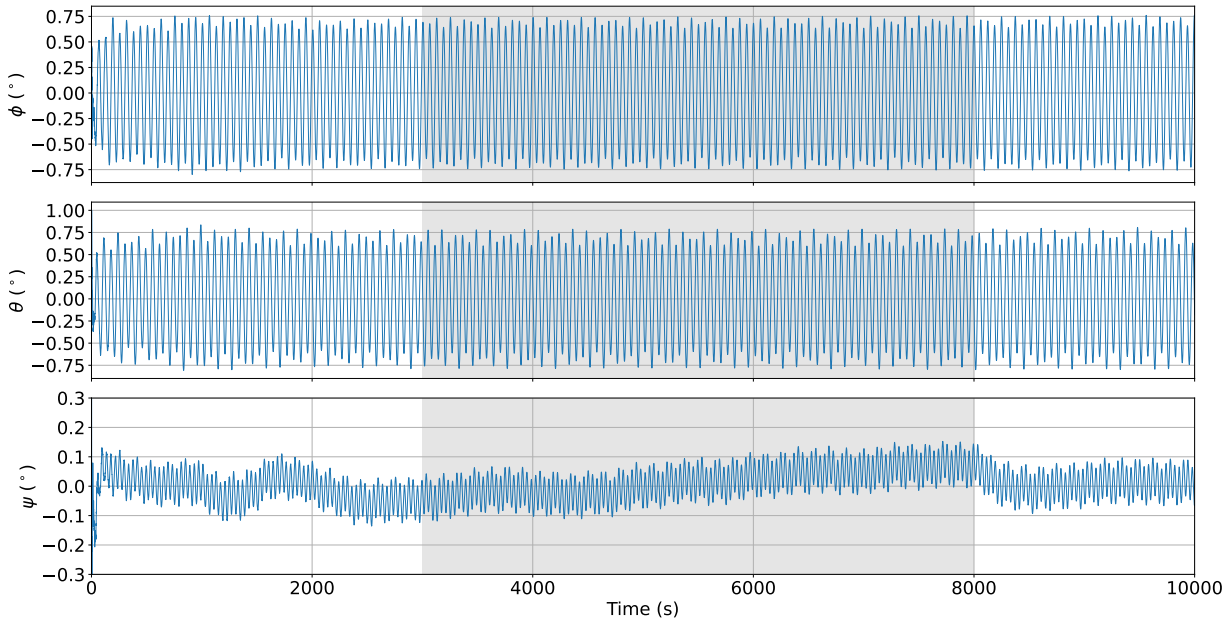

Source: Author.

Table 5.2 shows that the adapted filter performance is very close from the filter in the nominal operation. The filter without adaptation almost doubled the angular error. The root mean squared (rms) error is used for the filter assessment.

Table 5.2. Euler angles rms errors.

Angle	**Nominal**	**Non-Adaptive filter**	**Adaptive filter**
ϕ	0.53884	0.99652	0.54588
θ	0.51512	1.07070	0.47122
ψ	0.04244	0.71306	0.04715

5.1.4.2 Gyroscope Bias Abrupt Change

In this simulation the gyroscope bias will suffer an abrupt change in its bias. It will be added $\begin{bmatrix}1 & 1 & 1\end{bmatrix} \times 10^{-5}\ rad/s$ into the measurements. The performance of the non-adaptive filter is shown in Figure 5.18.

Figure 5.19 shows that the yaw angle suffered an increase of error, while the pitch and roll almost had no changes.

Figure 5.18. MEKF angle error with bias abrupt change.

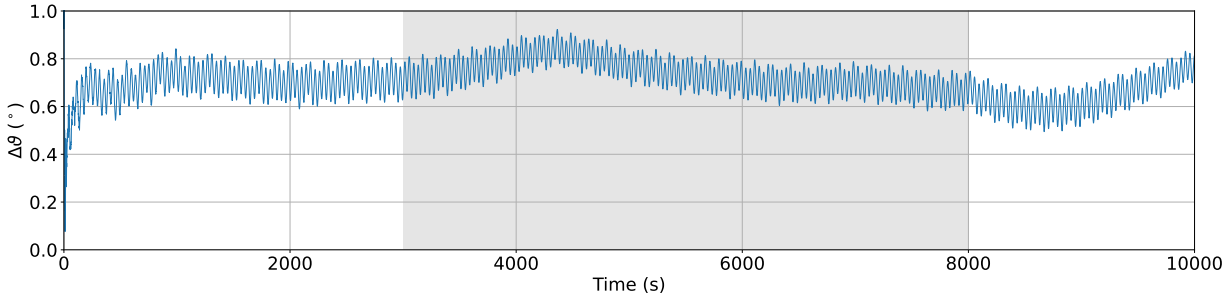

Source: Author.

Figure 5.19. MEKF Euler angles errors with bias abrupt change.

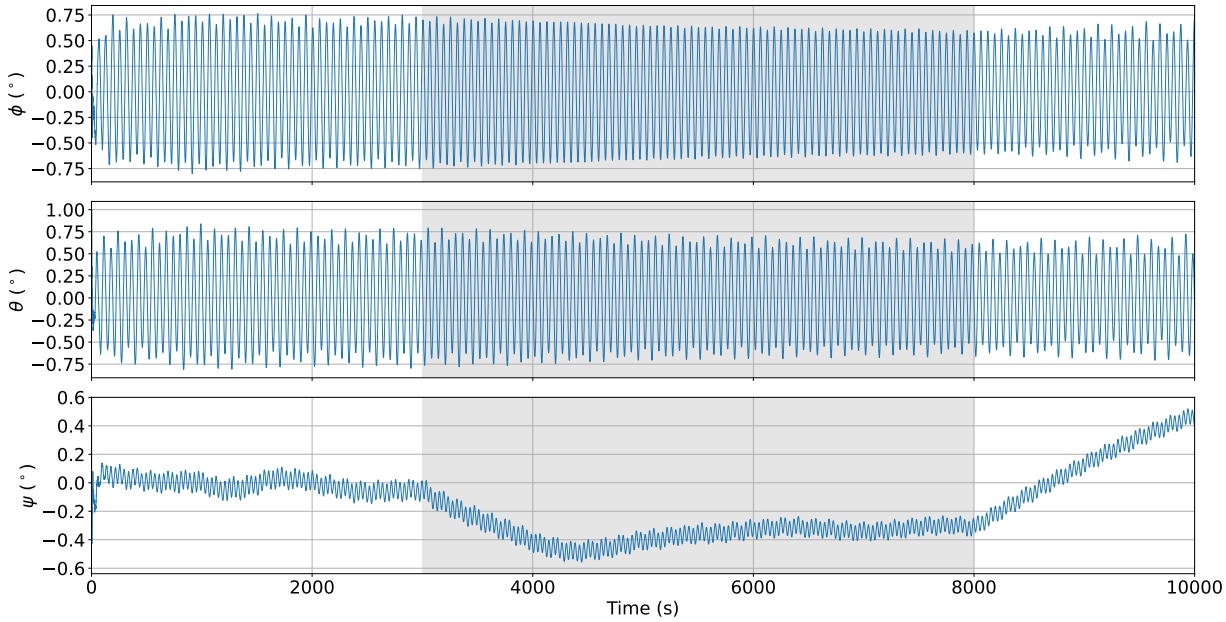

Source: Author.

The adaptive filter had a smaller overshoot in the angular error, as presented in Figure 5.20, despite in both cases the error has the same behavior. The MEKF had its process noise covariance matrix adapted in which the sliding windows is of 100 samples. The low-pass filter for the matrix update is $\alpha = 0.8$.

Figure 5.20. Adaptive MEKF angle error with bias abrupt change.

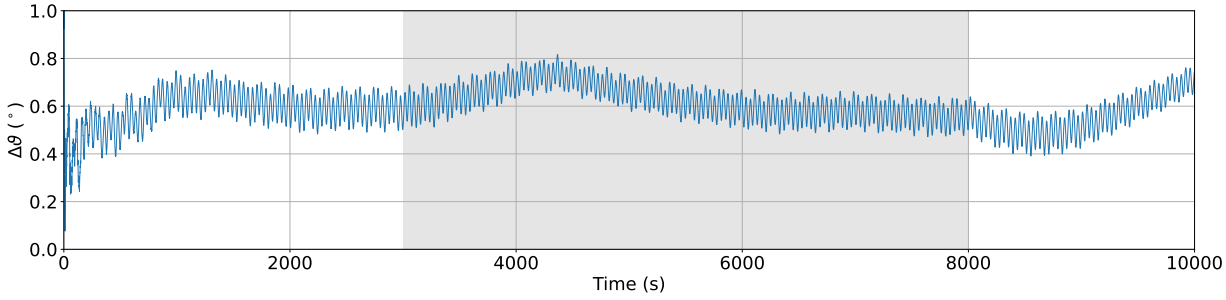

Source: Author.

Figure 5.21 shows that as for the non-adaptive case, the yaw angle is the most impacted with the bias change.

Figure 5.21. Adaptive MEKF Euler angles errors with bias abrupt change.

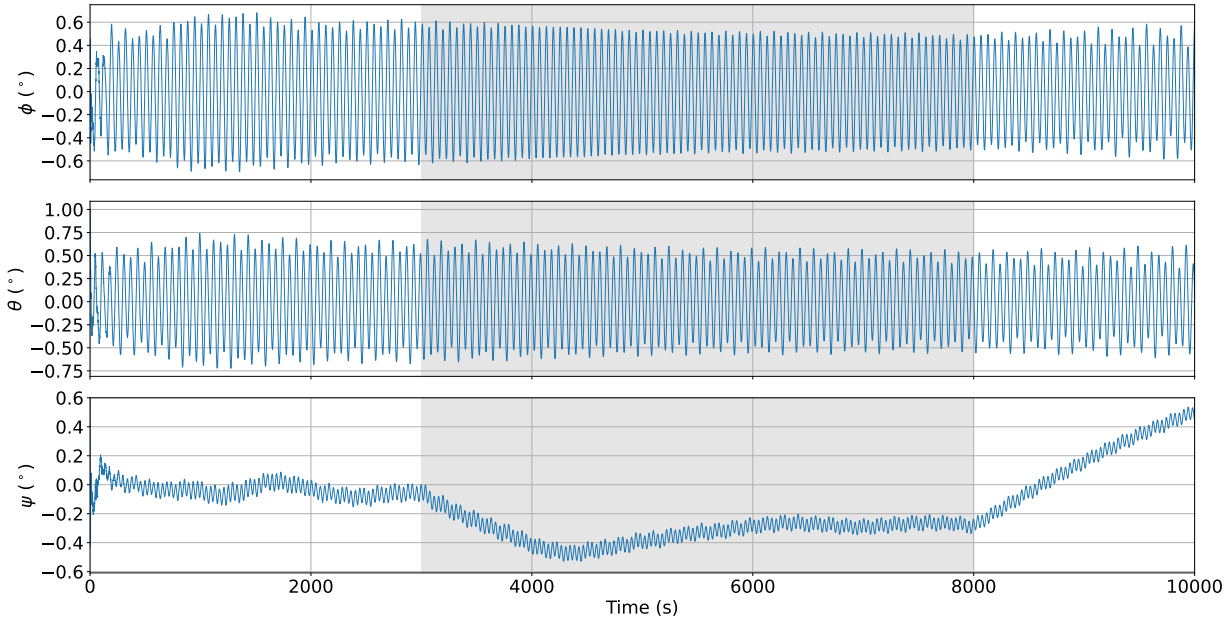

Source: Author.

Table 5.3 shows that the adapted filter performance is better than the non-adaptive version and even the nominal one. The filter without adaptation presented an error 23% higher in the ψ angle when compared with the adaptive algorithm. The ϕ angle of the adaptive estimator is smaller than the error in the nominal case, which shows that the covariance matrix can be optimized in the nominal situation in order to improve the overall estimation.

Table 5.3. Euler angles rms errors with bias abrupt change.

Angle	Nominal	Non-Adaptive filter	Adaptive filter
ϕ	0.53884	0.56868	0.35200
θ	0.51512	0.52046	0.54394
ψ	0.04244	0.58882	0.47806

5.1.4.3 Sun Sensor Degradation

For the Sun sensor degradation, it will be considered a negative bias of $\begin{bmatrix}-0.8 & -0.3 & -0.5\end{bmatrix}$ applied to the computer solar direction vector. The angle error for the non-adaptive filter is shown in Figure 5.22.

Figure 5.22. MEKF angle error with Sun sensor degradation.

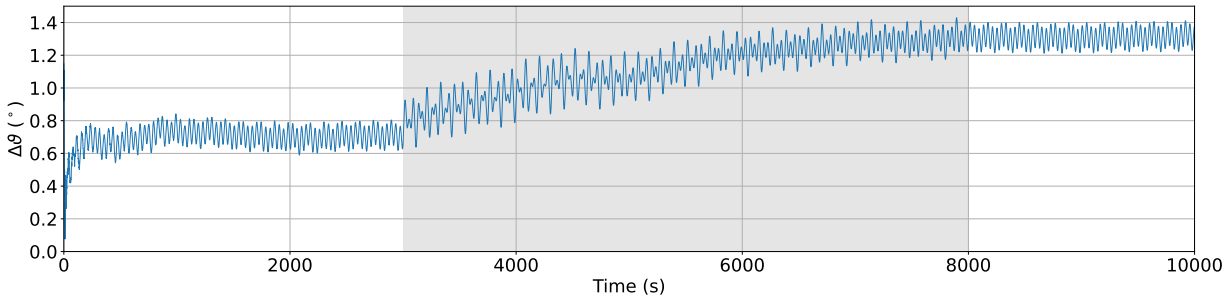

Source: Author.

The Euler angles for this case is presented in Figure 5.23. The three Euler angles are affected due to the degradation, however the yaw angle returned to its original value faster than the others two.

Figure 5.23. MEKF Euler angles errors with Sun sensor degradation.

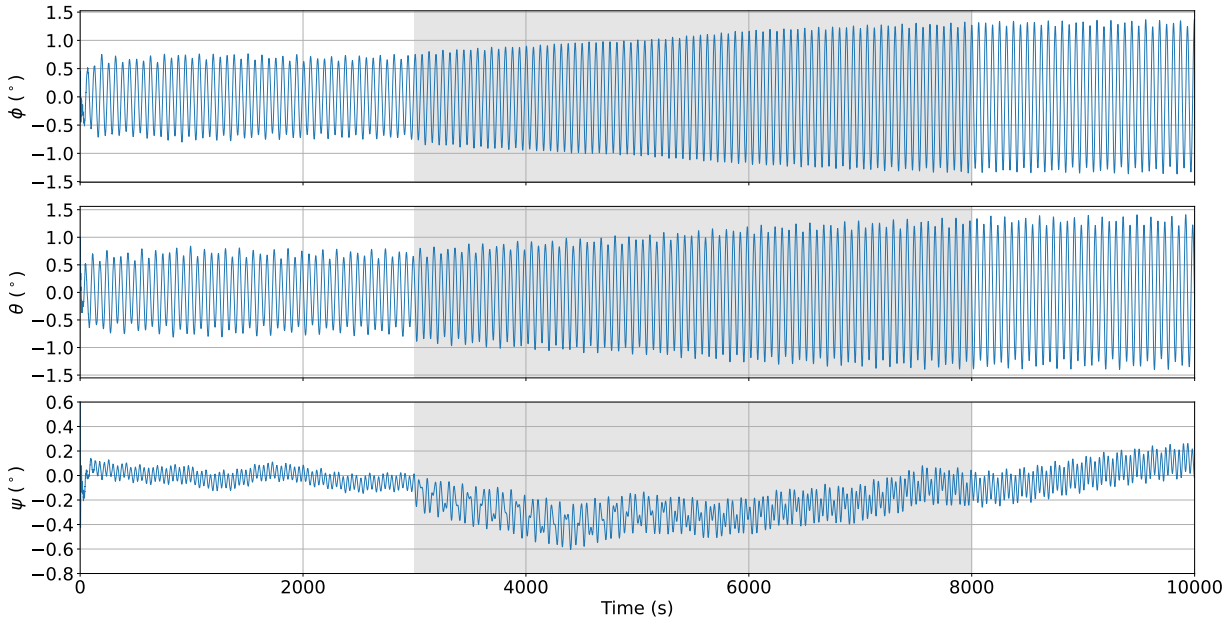

Source: Author.

For the filter executed with adaptation in the measurement noise covariance matrix and sliding windows of 100 samples, the result is shown in Figure 5.24. The error is close to the original case, with no degradation.

Figure 5.25 shows that no change in the Euler angles errors are perceived. As for the magnetometer case, the measurement weighting reduces the contribution of the Sun sensors observation in the estimation.

Table 5.4 summarizes the rms values of the Euler angles errors. It shows that the adaptation

Figure 5.24. Adaptive MEKF angle error with Sun sensor degradation.

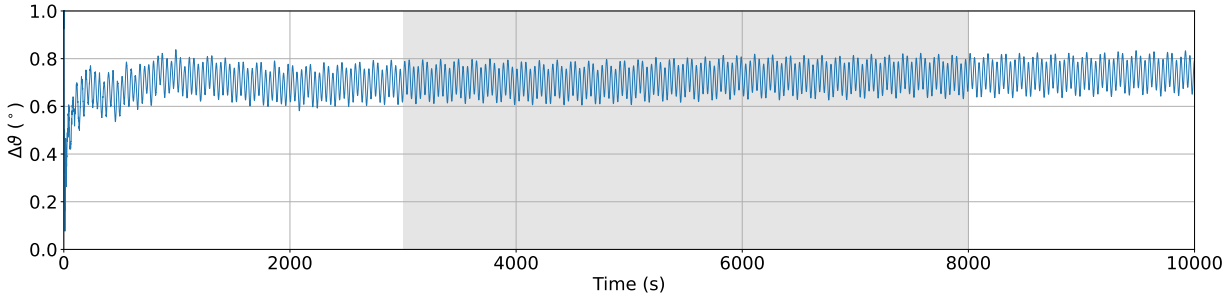

Source: Author.

Figure 5.25. Adaptive MEKF Euler angles errors with Sun sensor degradation.

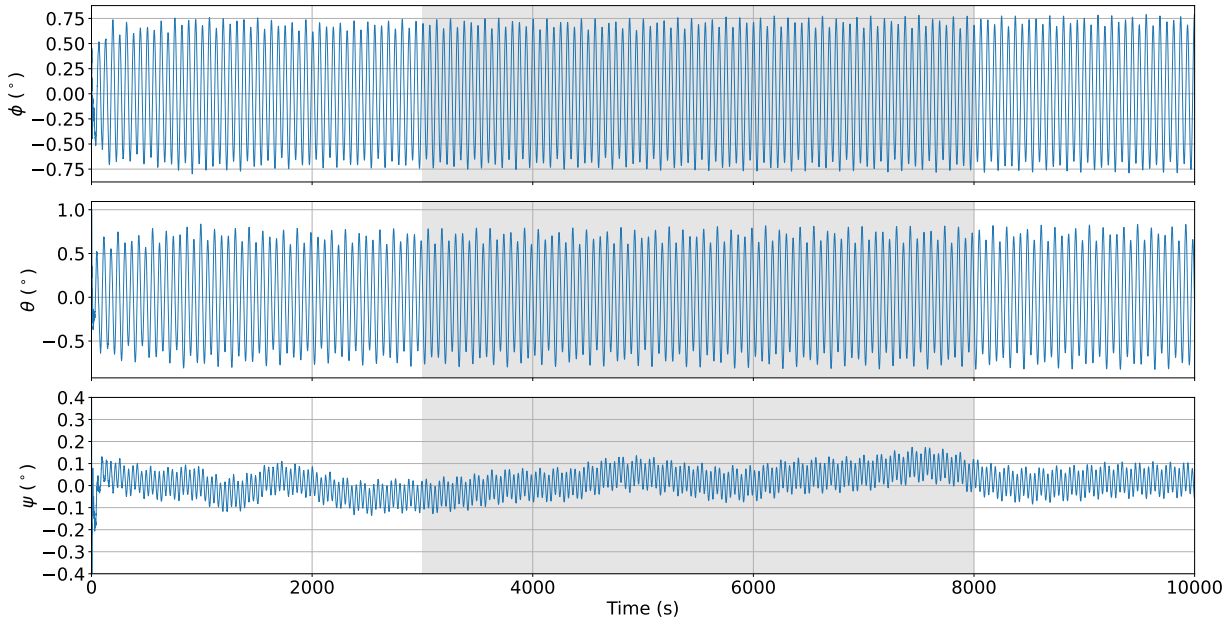

Source: Author.

mechanism keeps the errors almost unaltered, while the non-adaptive filter had a considerable increase in the errors.

Table 5.4. Euler angles rms errors.

Angle	Nominal	Non-Adaptive filter	Adaptive filter
ϕ	0.53884	0.92519	0.54636
θ	0.51512	0.83785	0.50922
ψ	0.04244	0.22524	0.04280

5.1.5 Adaptive USQUE

For the adaptive USQUE, the same three cases of perturbations will be considered. Both filters, with adaptation and without the feature will be compared and the results discussed.

5.1.5.1 Magnetometer Noise Increase

For this simulation, the magnetometer noise suffered an increase of 200 times in its magnitude, changing the statistical characteristics and generating outliers. Figure 5.26 presents the angle error due to this disturbance. The increase of the noise level occurs in the gray area of the graphs and then the noise level return to its original value.

Figure 5.26. USQUE angle error when noise level increase.

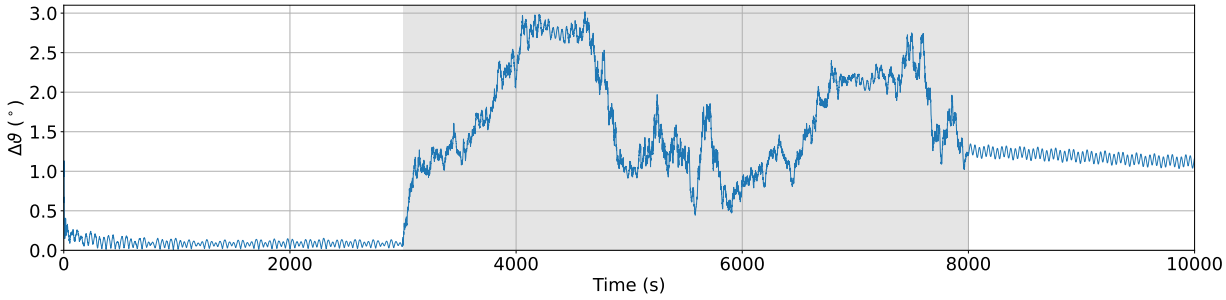

Source: Author.

The individual contribution of each Euler angle can be seen in Figure 5.27. After the disturbance stops, the error slowly approach to its original value.

Figure 5.28 presents the angle error of the USQUE with the measurement noise covariance matrix adaptation in which the sliding windows is of 100 samples. The algorithm is able to accommodate the perturbation, that is, the magnetometer noise was scaled in a form that the measurements weight were lower than the nominal case, reducing its contribution to the estimation.

In the Figure 5.29 the Euler angles errors are presented in which the curves shows and increase of the error level in the pitch and yaw angles.

Table 5.5 shows that the adapted filter performance is close from the filter in the nominal operation. The filter without adaptation had an increase of 10 times on average in the angular error while the adaptive filter kept the same error magnitude order.

Figure 5.27. USQUE Euler angles error when noise level increase.

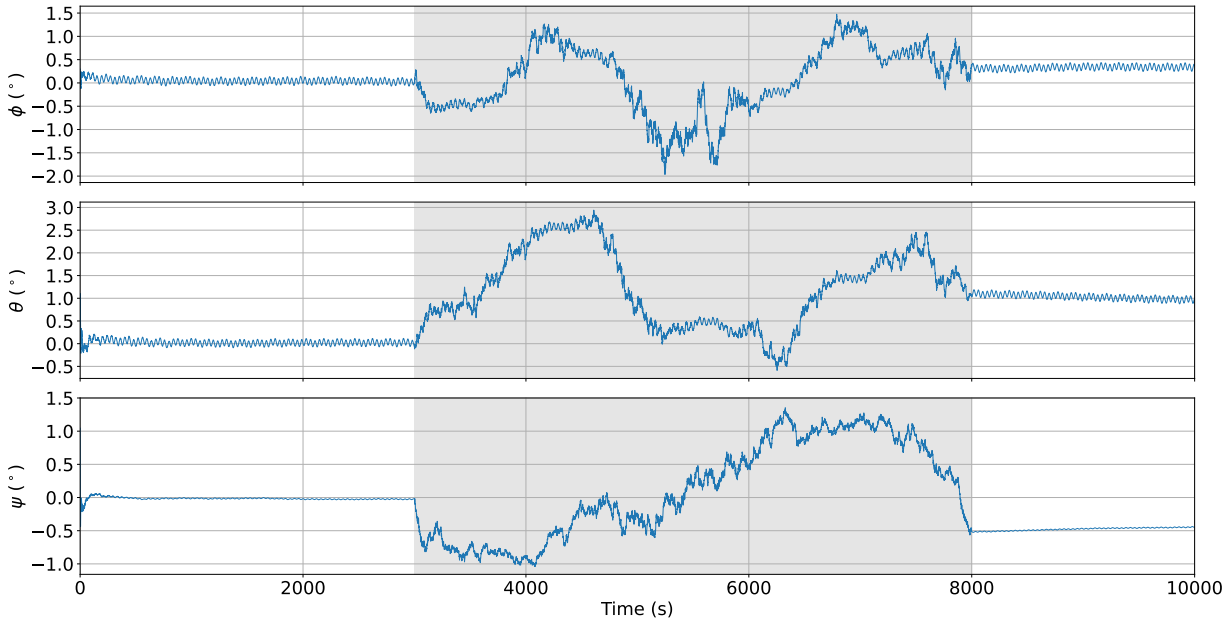

Source: Author.

Figure 5.28. Adaptive USQUE angle error when noise level increase.

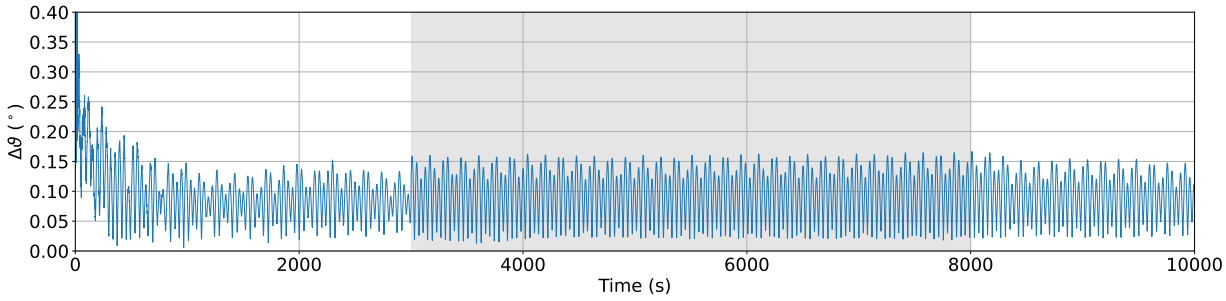

Source: Author.

Table 5.5. Euler angles rms errors.

Angle	Nominal	Non-Adaptive filter	Adaptive filter
ϕ	0.06026	0.39760	0.07070
θ	0.06098	0.89456	0.05910
ψ	0.03256	0.43359	0.03190

5.1.5.2 Gyroscope Bias Abrupt Change

In this simulation the gyroscope bias will suffer an abrupt change in its bias. It will be added $\begin{bmatrix}1 & 1 & 1\end{bmatrix} \times 10^{-5}\ rad/s$ into the measurements. The performance of the non-adaptive filter is shown in Figure 5.30.

Figure 5.31 shows that the roll and yaw angles suffered an increase of error, while the pitch angle almost had no changes. The total error was about 2°.

Figure 5.29. Adaptive USQUE Euler angles error when noise level increase.

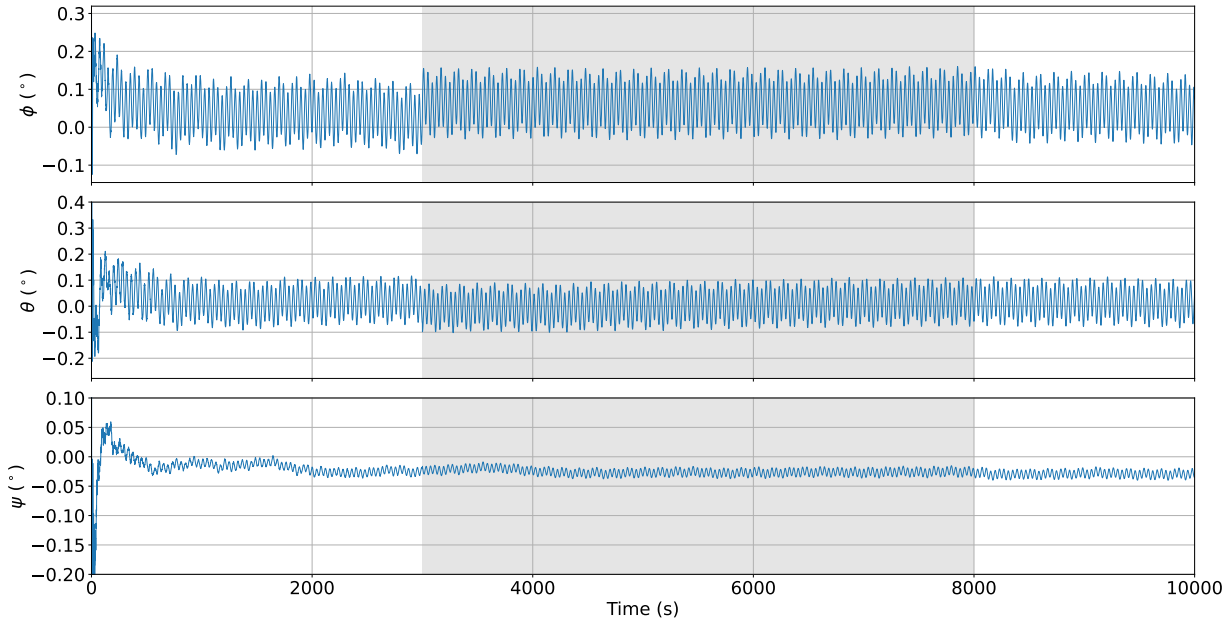

Source: Author.

Figure 5.30. USQUE estimated angle error.

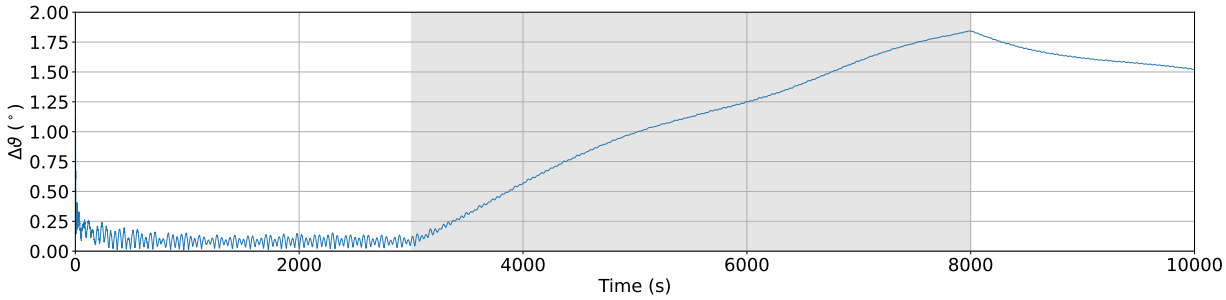

Source: Author.

The adaptive filter had a smaller overshoot in the angular error, almost a half of the previous case, as presented in Figure 5.32. The USQUE had its process noise covariance matrix adapted in which the sliding windows is of 100 samples. The low-pass filter for the matrix update is $\alpha = 0.8$.

Figure 5.33 shows that the yaw angle suffered an increase of error, while the others two angles almost had no change.

Table 5.6 shows that the adapted filter performance is better than the non-adaptive version and even the nominal one. The filter without adaptation presented errors around 50% higher than the adapted version.

Figure 5.31. USQUE Euler angles errors with bias abrupt change.

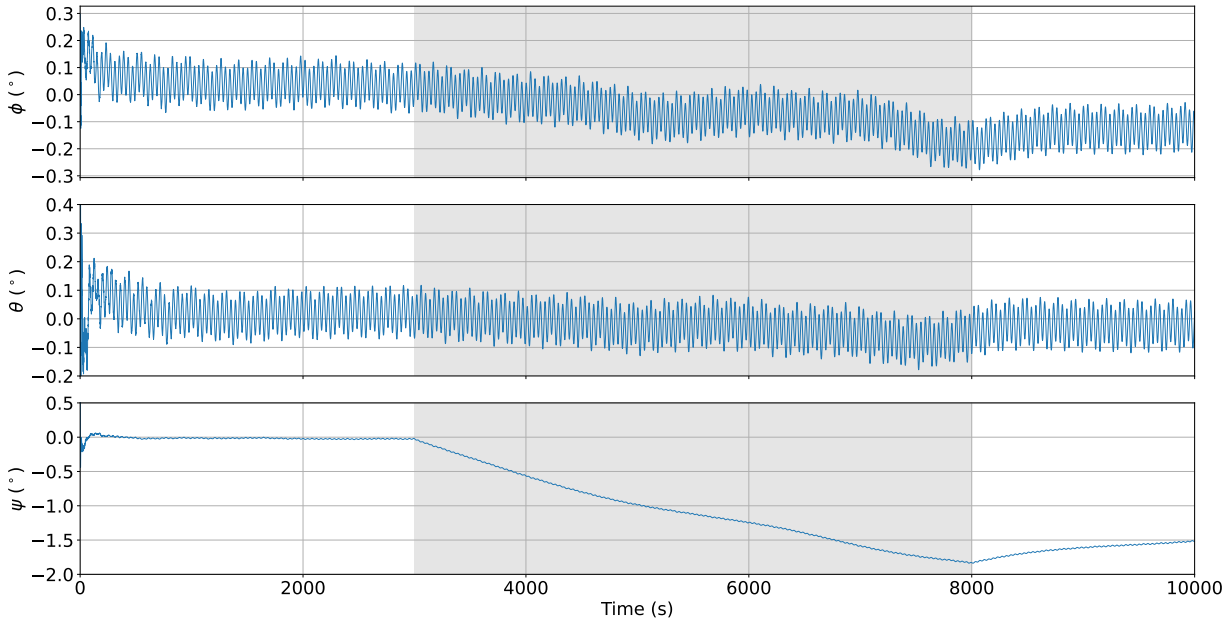

Source: Author.

Figure 5.32. Adaptive USQUE estimated angle error.

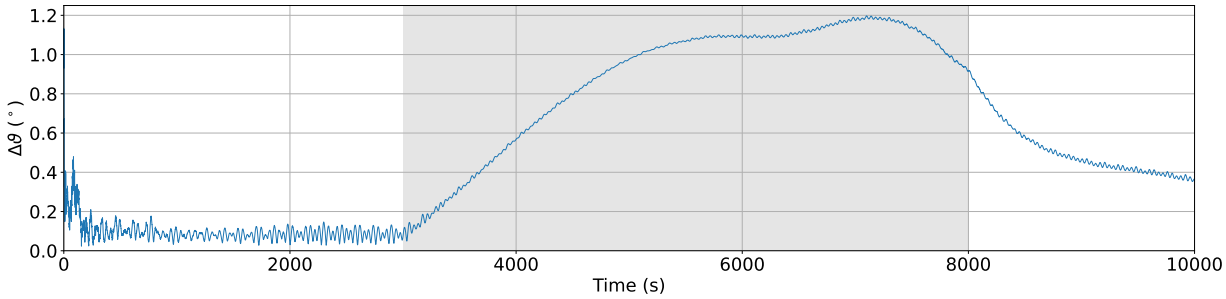

Source: Author.

Table 5.6. Euler angles rms errors with bias abrupt change.

Angle	Nominal	Non-Adaptive filter	Adaptive filter
ϕ	0.06026	0.09886	0.06129
θ	0.06098	0.06274	0.06317
ψ	0.03256	0.99916	0.48626

5.1.5.3 Sun Sensor Degradation

For the Sun sensor degradation, it will be considered a negative bias of $\begin{bmatrix}-0.8 & -0.3 & -0.5\end{bmatrix}$ applied to the computed solar direction vector. The angle error for the non-adaptive filter is shown in Figure 5.34.

The Euler angles for this case is presented in Figure 5.35. The three Euler angles are affected due to the degradation, however the pitch angle had an increase higher the roll and yaw angles.

Figure 5.33. Adaptive USQUE Euler angles errors with bias abrupt change.

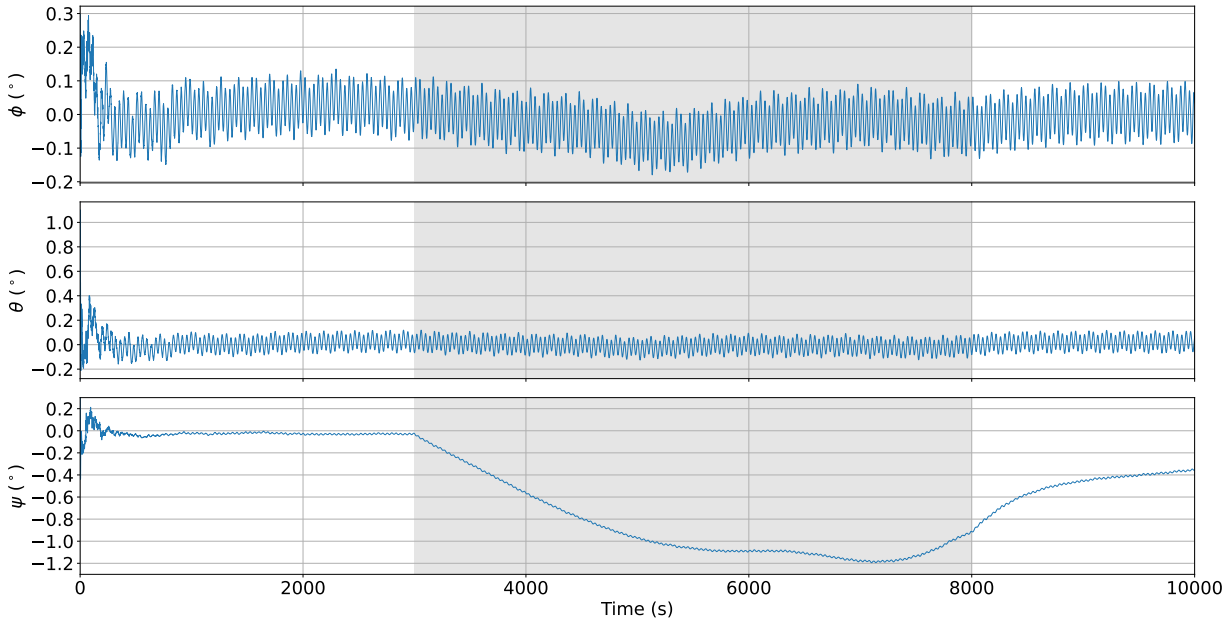

Source: Author.

Figure 5.34. USQUE angle error with Sun sensor degradation.

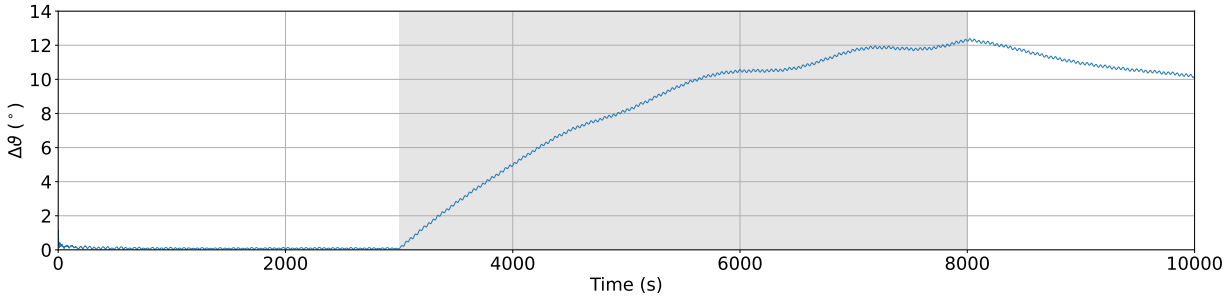

Source: Author.

For the filter executed with adaptation in the measurement noise covariance matrix and sliding windows of 100 samples, the result is shown in Figure 5.36. The error is close to the original case, with no degradation.

Figure 5.37 shows that no change in the Euler angles errors are perceived. As for the magnetometer case, the measurement weighting reduces the contribution of the Sun sensors observation in the estimation.

Table 5.7 summarizes the rms of the Euler angles errors. It shows that the adaptation mechanism keeps the errors almost unaltered, while the non-adaptive filter had a considerable increase in the errors.

Figure 5.35. USQUE Euler angles errors with Sun sensor degradation.

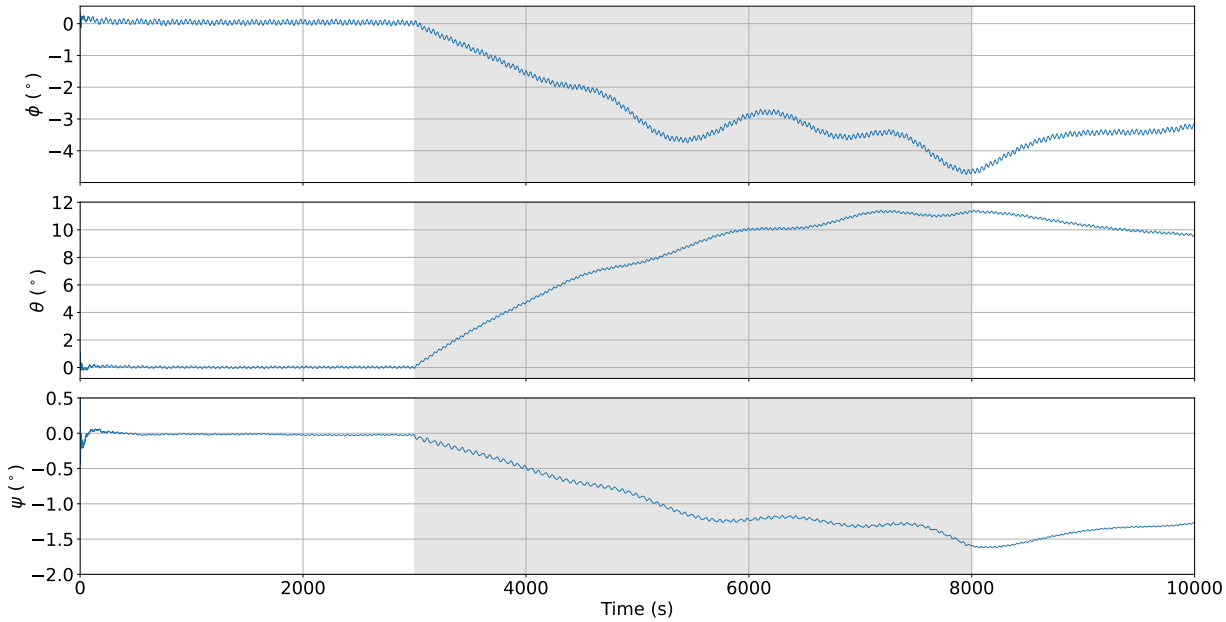

Source: Author.

Figure 5.36. Adaptive USQUE angle error with Sun sensor degradation.

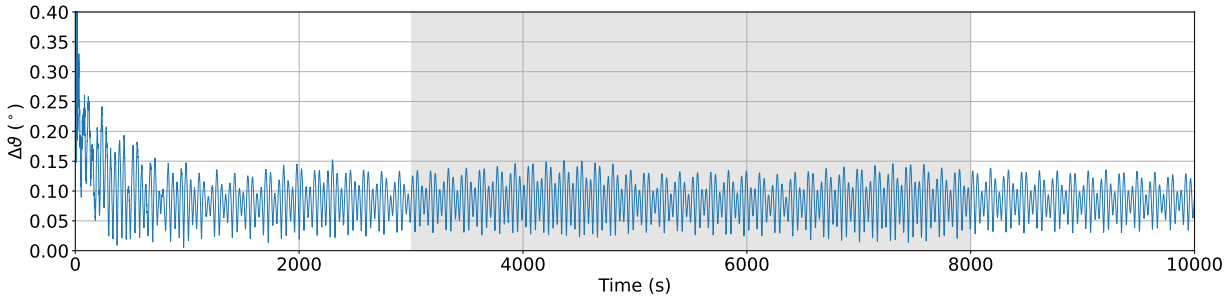

Source: Author.

Table 5.7. Euler angles rms errors with bias abrupt change.

Angle	Nominal	Non-Adaptive filter	Adaptive filter
ϕ	0.06026	2.32153	0.05898
θ	0.06098	6.71206	0.06511
ψ	0.03256	0.88447	0.03367

5.1.6 Outlier Detection

The abrupt or fast and intense disturbances in the on-board sensor observations may cause the filter divergence even with the adaptation mechanism once the innovations sequence can introduce an abrupt change in the noise covariance matrices. Also, for on-board applications with constrained computation resources, which is the case of small satellites, the execution of

Figure 5.37. Adaptive USQUE Euler angles errors with Sun sensor degradation.

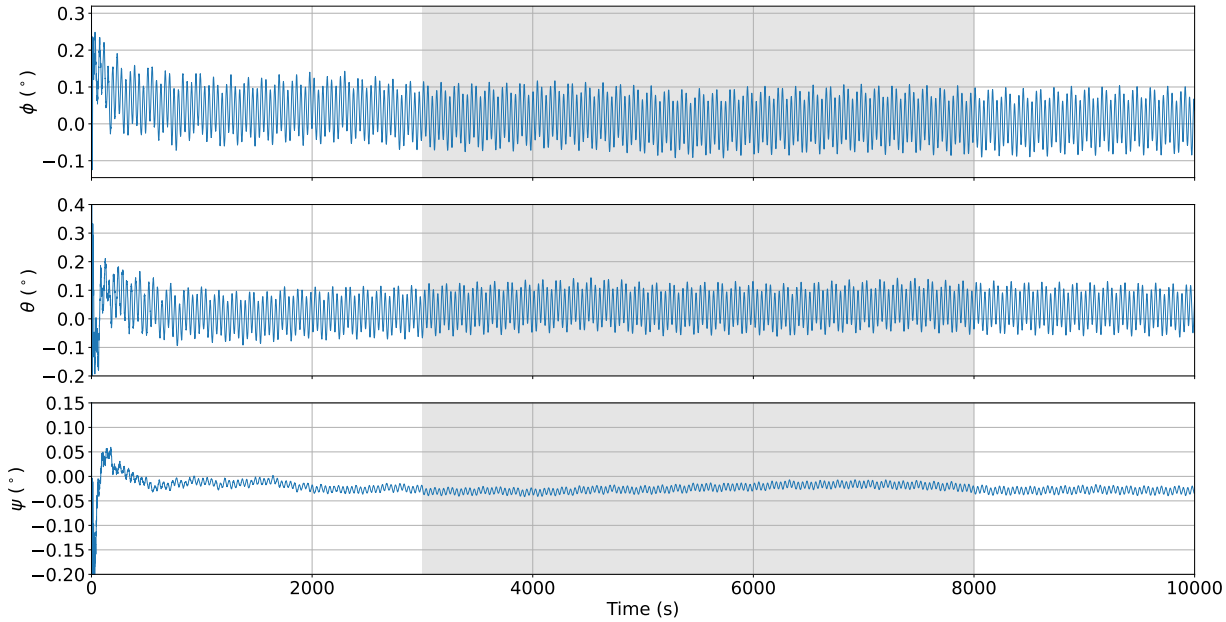

Source: Author.

the filter adaptation is computationally consuming.

In order to execute the adaptive algorithm only when a change is perceived, an outlier or fault detection technique may be executed. The outlier detection is a statistical test that verify if a fault had occurred. (HAJIYEV; SOKEN, 2020) uses the innovations vector for the fault detection as

$$d_k^2 = \boldsymbol{\upsilon}_k^T \left[\mathbf{H}_k \mathbf{P}_k^- \mathbf{H}_k^T + \mathbf{R}_k\right]^{-1} \boldsymbol{\upsilon}_k, \tag{5.10}$$

for the EKF filter and for the UKF it is given as

$$d_k^2 = \boldsymbol{\upsilon}_k^T \left[\mathbf{P}_k^{yy} + \mathbf{R}_k\right]^{-1} \boldsymbol{\upsilon}_k, \tag{5.11}$$

which is the squared Malahanobis distance for the innovations vector at instant k. The Malahanobis distance is a measure of similarity between two samples, normalized by the standard deviation. The figure 5.38 shows d_k^2 for the MEKF with the magnetometer noise increase perturbation of 2 times.

The function d_k^2 has a χ^2 probability distribution with m degrees of freedom, where m is the innovation vector dimension. A hypothesis test can considers two options

$$\mathcal{H}_0 = \text{the system is nominal},$$

$$\mathcal{H}_1 = \text{fault have occurred in the system.}$$

Figure 5.38. Outlier detection

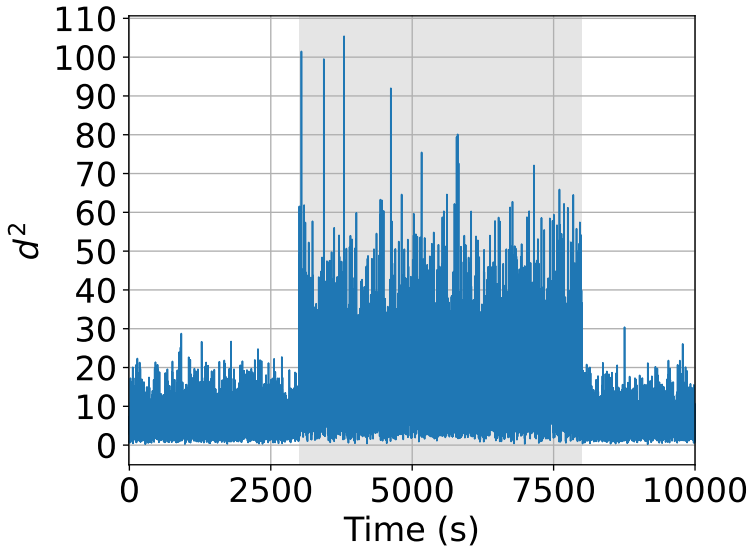

Source: Author.

Defining a confidence level, it is possible to set a lower bound to the value of d_k^2 through a χ^2 test, which will indicate the presence of outlier.

5.2 ALFACRUX'S CUBESAT ATTITUDE MOTION RECONSTRUCTION USING ON-BOARD SENSORS DATA

The second part of this chapter concerns the attitude reconstruction of a Cubesat by means of its telemetry data. The AlfaCrux CubeSat is an 1U nanosatellite launched in orbit on April 1st of 2022 in a Sun-synchronous orbit. It is an amateur radio and educational mission conducted by the University of Brasília, which provided the learning in areas such as project management, risk analysis and space missions design (BORGES *et al.*, 2022). The satellite's payload is a software-defined radio (SDR), working in the ultra-high frequency (UHF), which serves as an digital packet repeater and a store-and-forward system (BORGES *et al.*, 2022).

One objective of the research involving the AlfaCrux is the development of a Digital Twin (DT) model, which is an virtual representation of the CubeSat features, subsystems, capabilities and environment (KONTAXOGLOU *et al.*, 2021). This model also considers the attitude motion of the small satellite, since it is part of the spacecraft state (BORGES *et al.*, 2022). The attitude can be estimated using the telemetry data regarding the on-board sensors.

Such CubeSat has a on-board computer (OBC) with a tri-axis magnetometer and gyroscope. AlfaCrux has no embedded attitude control system, neither a filtering algorithm for the attitude determination. However, the sensor's data can be retrieved from the telemetry packets stored in a database. Currently, the nanosatellite transmits telemetry data with a sampling period of 30 seconds.

In (MELLO *et al.*, 2022), it is used the USQUE filter for the AlfaCrux attitude reconstruction using a gyroscope-based process model, the magnetometer measurements and the Sun direction estimation through the solar panels data. In (BRENAG *et al.*, 2022) and (BRENAG *et al.*, 2023) a different approach using magnetometer-only data was considered, based on (IVANOV *et al.*, 2021).

The approach first step is the estimation of the magnetometer bias, which is considered constant in the time interval of analysis. The telemetry data is compared with the IGRF model and the mean bias is computed using the least squares method. With a small on-orbit sensors dataset, the determination of the initial state vector is fundamental for the filter fast convergence. Figure 5.39 shows the attitude reconstruction workflow.

Figure 5.39. AlfaCrux's attitude motion reconstruction procedure.

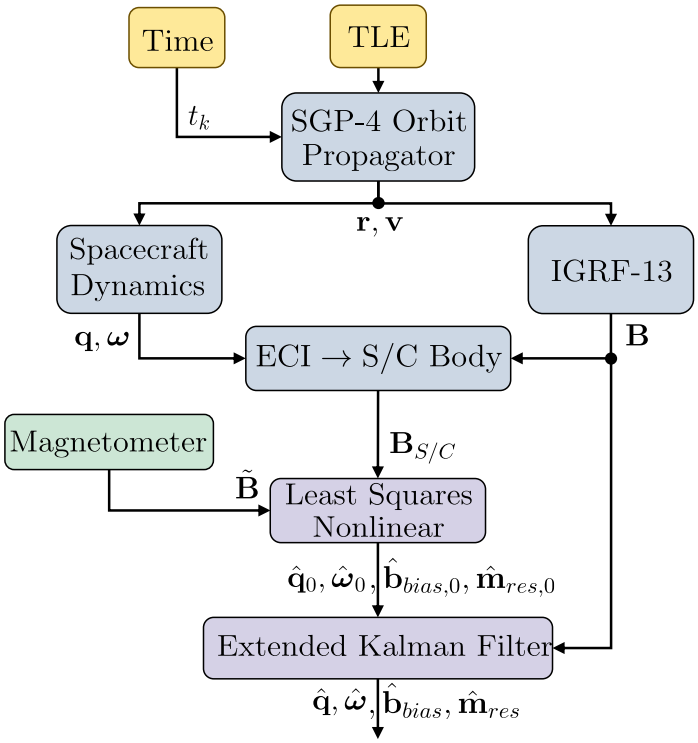

Source: Author.

In order to find the initial attitude parameters and angular rate, an optimization problem

was formulated. Based only on the magnetometer data, now corrected with the estimated mean bias, the initial state is found by minimizing the cost function defined as the difference between the sensor data and the predicted magnetic field provided by a attitude kinematics and dynamics set of equations propagated on time. That is, let $\Gamma(\boldsymbol{\xi})$ be the cost function defined as

$$\Gamma(\boldsymbol{\xi}) = \sum_{k=0}^{N} \left(\mathbf{B}^{k}_{model} - \mathbf{B}^{k}_{meas}\right)^{2}, \tag{5.12}$$

in which $\mathbf{B}_{model}$ is the geomagnetic field from the dynamics model, $\mathbf{B}_{meas}$ is the magnetometer data and $\boldsymbol{\xi} = \begin{bmatrix}\mathbf{q}(0) & \boldsymbol{\omega}(0) & \mathbf{m}_{res} & \mathbf{b}_{m}\end{bmatrix}$ is the state vector. The parameter $\mathbf{b}_{m}$ is the small fluctuation in the estimated mean bias.

The nonlinear batch least squares is solved using the Differential Evolution (DE) technique. This is a stochastic search algorithm in which a population of state vector samples are generated randomly in the state space, and the best cost vector is used in the next iteration in place of an state vector with higher cost value. Some operations are included in order to increase the samples variability. More details can be found in (BRENAG *et al.*, 2022), (BRENAG *et al.*, 2023) and in (STORN; PRICE, 1997).

As results from previous works presented in (MELLO *et al.*, 2022), (BRENAG *et al.*, 2022) and (BRENAG *et al.*, 2023), the preliminary analysis of AlfaCrux's attitude motion is performed using telemetry data from September 16th of 2022 at 13h50 to 13h56 UTC. The set of date comprises 10 telemetry packets with sampling period of 30 seconds. Figure 5.40 presents the magnetometer data and the corrected values without bias.

Figure 5.40. AlfaCrux magnetometer measurements and corrected data.

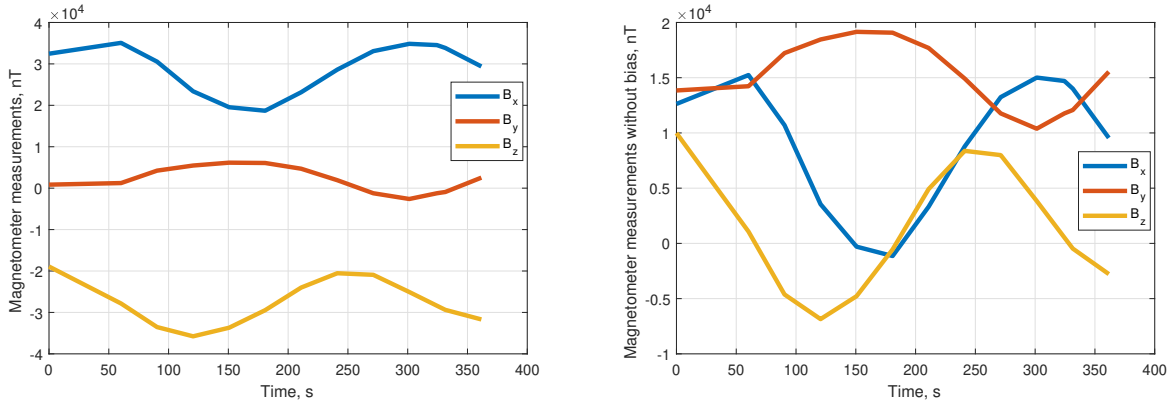

Source: Author.

From the batch processing of the magnetometer data, the initial state vector can be es-

timated and propagated in time through a precise dynamics model in order to verify if the observations are consistent with the predicted values from the model. Figure 5.41 present the magnetometer observations and the predicted measurements computed using the dynamics model.

Figure 5.41. AlfaCrux's magnetometer measurements and model.

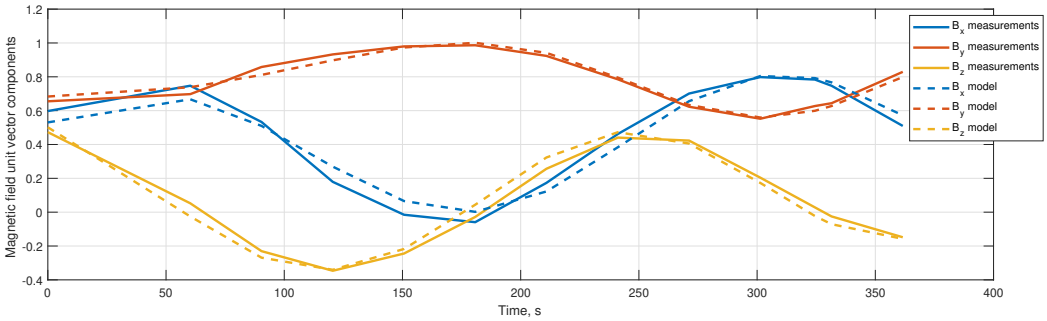

Source: Author.

It is possible to verify the correspondence between the telemetry data curves and the model generated ones. That is, the initial state vector found through the optimization problem is consistent regarding the generated model data comparing with the sensors corrected data.

Although the estimation is based on magnetometer-only data, the gyroscope measurements can be used to assess the estimation accuracy. In this approach, the telemetry data and the estimated angular rate can be compared in order to verify if the model produces the same profile than the observations. Figure 5.42 shows the gyroscope telemetry data.

Figure 5.42. AlfaCrux's gyroscope measurements.

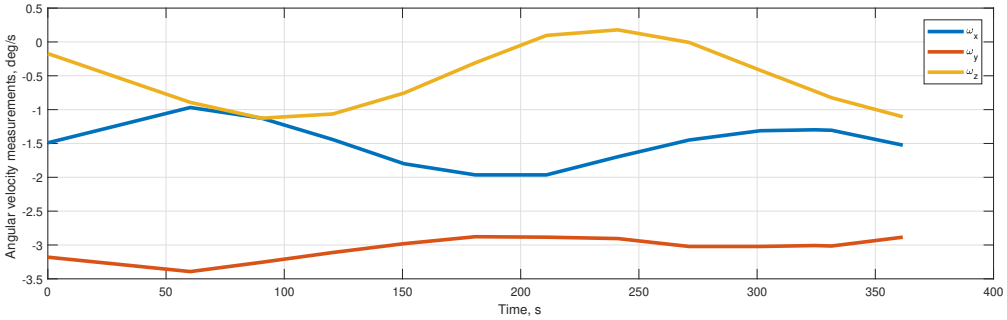

Source: Author.

By comparing the estimated angular rates and the observations from the gyroscope, one can detect the presence of a bias which produce a vertical shift in the graphs. The Figure 5.43 shows the modeled and observed angular rates after subtracting the bias from the gyroscope

measurements.

Figure 5.43. AlfaCrux's modeled and observed angular rate with bias correction.

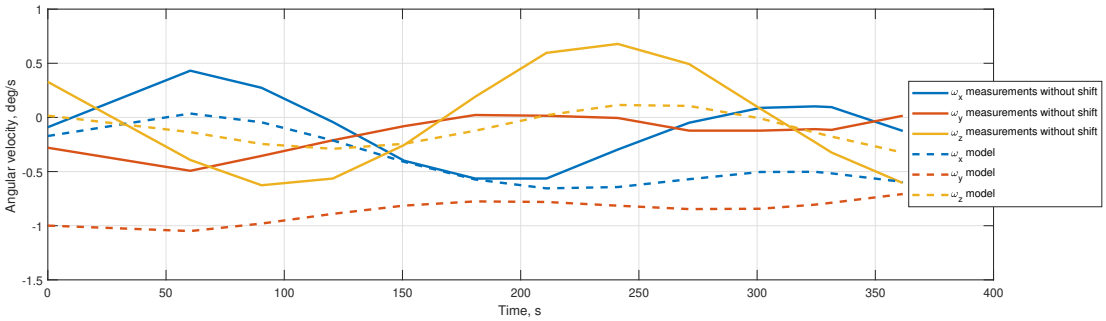

Source: Author.

As for the magnetometer observations, in the gyroscope data one can verify that both modeled and measured curves are correlated, that is, the angular rates provided by the model have the same behaviour of the sensors data, when a bias is considered, which is a valid statement since the MEMS gyroscope bias vary on time.

In order to improve the system estimation and prediction, the Kalman filtering techniques can be used. To deal with the under-sampled small dataset, synthetic magnetometer data can be generated using the dynamics model propagation. It will allow the attitude motion estimation and the accuracy computing.

The Dynamics-based MEKF is formulated as described in (IVANOV *et al.*, 2021). First, a linearization is considered such as

$$\Delta\dot{\mathbf{x}} = \mathbf{F}(\mathbf{x},t)\Delta\mathbf{x}, \tag{5.13}$$

in which the state vector is given by

$$\hat{\mathbf{x}} = \begin{bmatrix}\boldsymbol{\varrho}^T & \boldsymbol{\omega}^T & \mathbf{m}_{res}^T & \mathbf{b}_{m,}^T\end{bmatrix}^T \tag{5.14}$$

where $\boldsymbol{\varrho}$ is the quaternion vector part, $\boldsymbol{\omega}$ is the angular rate, $\mathbf{m}_{res}$ is the residual magnetic moment and $\mathbf{b}_m$ is the magnetometer bias (IVANOV *et al.*, 2017).

The first-order approximation of the process model given by the Taylor Series is defined as

$$\mathbf{F}(\mathbf{x},t) = \begin{bmatrix} -[\hat{\boldsymbol{\omega}}\times] & \frac{1}{2}\mathbf{I}_{3\times3} & \mathbf{0}_{3\times3} & \mathbf{0}_{3\times3} \\ \mathbf{J}^{-1}(\mathbf{F}_g + \mathbf{F}_m) & \mathbf{J}^{-1}\mathbf{F}_{gir} & -\mathbf{J}^{-1}[(A\mathbf{B}_R)\times] & \mathbf{0}_{3\times3} \\ \mathbf{0}_{3\times3} & \mathbf{0}_{3\times3} & \mathbf{0}_{3\times3} & \mathbf{0}_{3\times3} \\ \mathbf{0}_{3\times3} & \mathbf{0}_{3\times3} & \mathbf{0}_{3\times3} & \mathbf{0}_{3\times3} \end{bmatrix}, \tag{5.15}$$

in which $\mathbf{F}_g$ is the gravity-gradient linear torque, $\mathbf{F}_m$ is the residual magnetic linear torque and $\mathbf{F}_{gir}$ is the gyroscopic linear torque (IVANOV *et al.*, 2017). Such forces are given as

$$\mathbf{F}_g = 6\omega_0^2 \left([(A\mathbf{o}_3)\times] \, \mathbf{J} \, [(A\mathbf{o}_3)\times] - [(\mathbf{J}A\mathbf{o}_3)\times] \, [(A\mathbf{o}_3)\times] \right), \tag{5.16a}$$

$$\mathbf{F}_m = 2 \left[\mathbf{m}_{res}\times \right] \left[(A\mathbf{B}_R) \times \right], \tag{5.16b}$$

$$\mathbf{F}_{gir} = 2 \left([(\mathbf{J}\boldsymbol{\omega})\times] \, [\boldsymbol{\omega}\times] - [\boldsymbol{\omega}\times] \, \mathbf{J} \, [\boldsymbol{\omega}\times] \right). \tag{5.16c}$$

Therefore, the discrete-time state transition matrix is given by

$$\mathbf{F}_k = \mathbf{I}_{12\times 12} + \mathbf{F}(\mathbf{x},t)\Delta t, \tag{5.17}$$

in which Δt is the sampling period.

The process noise covariance matrix is given by

$$\mathbf{Q}(t) = \begin{bmatrix} \sigma_{dyn}^2 \mathbf{I}_{3\times 3} & \mathbf{0}_{3\times 3} & \mathbf{0}_{3\times 3} \\ \mathbf{0}_{3\times 3} & \sigma_{rm}^2 \mathbf{I}_{3\times 3} & \mathbf{0}_{3\times 3} \\ \mathbf{0}_{3\times 3} & \mathbf{0}_{3\times 3} & \sigma_{bm}^2 \mathbf{I}_{3\times 3} \end{bmatrix}, \tag{5.18}$$

in which σ_{dyn} is the process model noise, σ_{rm} is the residual magnetic dipole noise and σ_{bm} is the magnetometer bias noise, the uncertainty sources of the associated dynamics model. And the matrix that maps the noise covariance matrix to the state vector space is written as

$$\mathbf{G}(t) = \begin{bmatrix} \mathbf{0}_{3\times 3} & \mathbf{0}_{3\times 3} & \mathbf{0}_{3\times 3} \\ \mathbf{J}^{-1} & \mathbf{0}_{3\times 3} & \mathbf{0}_{3\times 3} \\ \mathbf{0}_{3\times 3} & \mathbf{I}_{3\times 3} & \mathbf{0}_{3\times 3} \\ \mathbf{0}_{3\times 3} & \mathbf{0}_{3\times 3} & \mathbf{I}_{3\times 3} \end{bmatrix}. \tag{5.19}$$

The equivalent discrete-time process noise covariance matrix is computed as

$$\mathbf{Q}_k = \mathbf{F}_k \mathbf{G}(t) \mathbf{Q}(t) \mathbf{G}^T(t) \mathbf{F}_k^T \Delta t, \tag{5.20}$$

in which Δt is the sampling period.

Regarding the measurement model, the first-order linearization is given by

$$\Delta\mathbf{y} = \mathbf{H}(\mathbf{x},t)\Delta\mathbf{x}, \tag{5.21}$$

in which the predicted observation vector is defined as

$$\Delta\mathbf{y} = 2 \left[\mathbf{B}_R\times \right] \Delta\boldsymbol{\varrho} + \Delta\mathbf{b}_m. \tag{5.22}$$

Therefore, the sensitivity matrix is written as

$$\mathbf{H}_k = \begin{bmatrix} 2\left[\mathbf{B}_R\times\right] & \mathbf{0}_{3\times3} & \mathbf{0}_{3\times3} & \mathbf{I}_{3\times3} \end{bmatrix}. \tag{5.23}$$

Following the workflow from the EKF algorithm, an estimated error-quaternion is obtained from its vector part as

$$\Delta\mathbf{q}(\Delta\boldsymbol{\varrho}) = \begin{bmatrix} \Delta\boldsymbol{\varrho} \\ \sqrt{1-\Delta\boldsymbol{\varrho}^2} \end{bmatrix}. \tag{5.24}$$

Finally, the global quaternion is updated and the next iteration is executed. The initial state vector for the EKF is given by

$$\hat{\mathbf{q}}_0 = \begin{bmatrix} 0.9133 & 0.1994 & -0.34558 & -0.0820 \end{bmatrix}^T, \tag{5.25a}$$

$$\hat{\boldsymbol{\omega}}_0 = \begin{bmatrix} -0.0030 & -0.0174 & 0.0003 \end{bmatrix}^T \quad [\text{rad/s}], \tag{5.25b}$$

$$\hat{\mathbf{m}}_{res,0} = \begin{bmatrix} 0.0081 & 0.0174 & 0.0052 \end{bmatrix}^T \quad [\text{Am}^2], \tag{5.25c}$$

$$\hat{\mathbf{b}}_{m,0} = \begin{bmatrix} -171.2992 & 35.7578 & 140.8970 \end{bmatrix}^T \quad [\text{nT}]. \tag{5.25d}$$

5.2.1 Process Noise Adaptation

For the attitude determination of AlfaCrux CubeSat, a **Q**-adaptation procedure will be considered in order to improve the estimation accuracy of the filter. This adaptive method is used for the identification of the process noise, which is composed of the attitude kinematics and dynamics uncertainty, the residual magnetic moment and magnetometer bias noises.

In this problem, the adaptive rule is described in Chapter 4, but considering an approximation presented in (MOHAMED; SCHWARZ, 1999). From the definition of state residual, one obtains

$$\Delta\mathbf{x}_k = \hat{\mathbf{x}}_k^+ - \hat{\mathbf{x}}_k^- = \mathbf{K}_k\boldsymbol{\upsilon}_k \tag{5.26}$$

Therefore, considering the equation for the **Q** matrix adaptation, the estimated process noise covariance matrix can be approximated by

$$\hat{\mathbf{Q}}_k \approx \mathbf{K}_k\mathbf{C}_{\upsilon_k}\mathbf{K}_k^T \tag{5.27}$$

in which the covariance of the sample innovation sequence is computed using a moving windows

of N samples and can be written as

$$\mathbf{C}_{v_k} = \sum_{i=1}^{N} \boldsymbol{v}_i \boldsymbol{v}_i^T. \tag{5.28}$$

Using such dynamics-based MEKF (BRENAG *et al.*, 2022), the estimation accuracy of the magnetic dipole moment is shown in Figure 5.44 for the standard filter and its adapted version with window length of 100 samples.

Figure 5.44. AlfaCrux's magnetic dipole moment estimation accuracy in the EKF (left) and in the Adaptive EKF (right).

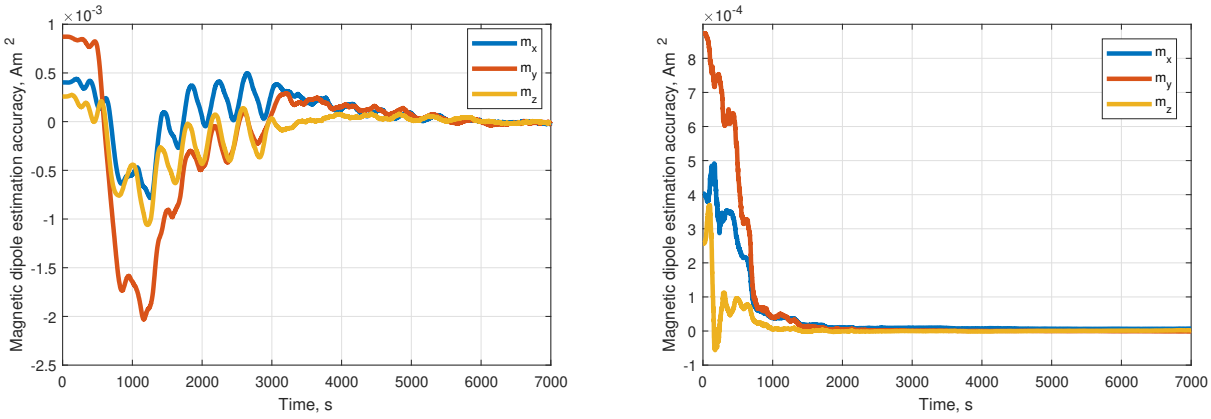

Source: Author.

The attitude angle estimation accuracy of the CubeSat is presented in Figure 5.45 for the standard filter and its adapted version.

Figure 5.45. AlfaCrux's attitude angle estimation accuracy in the EKF (left) and in the Adaptive EKF (right).

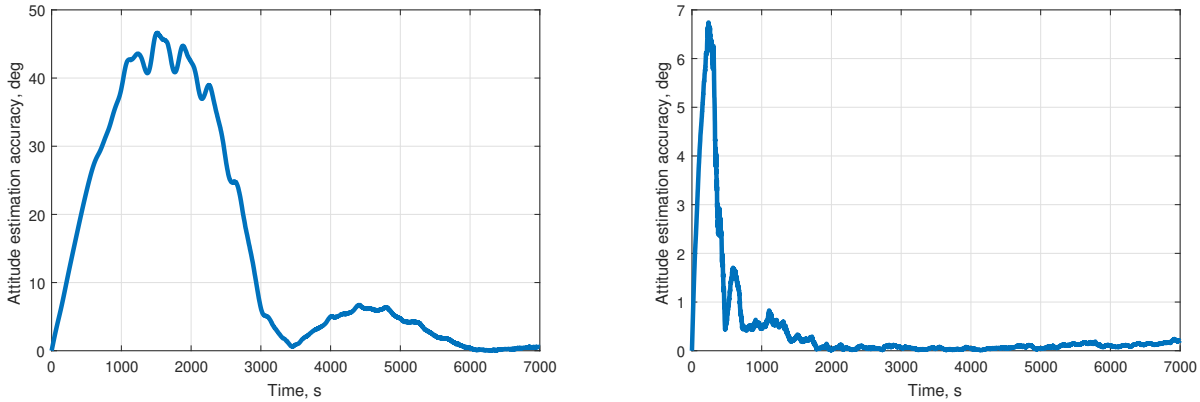

Source: Author.

The mean attitude angle error for the traditional filter is 14.8033°, while for the adaptive filter is 0.4312°. One can verify that the adaptation scheme provides a filtering process with better accuracy, once it tunes the covariance matrix based of the innovation. Besides, the

magnetic dipole estimation error converges faster than the standard filter, as the same happens to the attitude error. However, the second overshoot decreases slower for the adapted filter.

CHAPTER 6

CONCLUSIONS

The filtering algorithms presented an accuracy of less than ±1 degree, which was improved considering the process and measurement noise covariance matrices estimation in order to mitigate the errors caused by the disturbances effects and sensors unknown parameters. In adapting the attitude filter, the unknown or uncertain parameters from the sensors measurements, such as bias instability and noise statistics, could be derived from the innovations vector. For such cases, the error increase rate was around 10% from the nominal error. Without the adaptation mechanism the error when the disturbance was present was around 47%, which is considerable for hight precision platforms.

As first analysis, both the MEKF and USQUE filters are able to accommodate small increases in the noise level. As the statistics changes over time, both filters will lead to a higher error level. Therefore, the attitude estimation algorithm must consider adaptive parameters in order to keep the accuracy in a predictable interval. In real small satellite missions, the disturbance can degrade the performance of the related products. In cases of intense disturbances caused by the harsh space weather like the solar activities and cosmic radiation, the observations noise levels can increase to the point where the pointing error will be too large. The covariance matching can detect the disparity through the innovation moving window and the covariance matrices can be updated using analytical relations with the residuals.

One important aspect of the covariance matching adaptation technique is the size of the sliding window. If the sample set is to small, then both the measurement and process estimated covariance matrices may differ too much from their current values and the filter will diverge in case of abrupt variation in the sensor noise. in the same way, if the sample set length is large, then the filter may not be able to accommodate the disturbance due to the fact that the new covariance estimates will be closer to their current values.

Regarding the AlfaCrux attitude motion estimation, the adaptive filter showed its capability

to improve the estimator performance when the process noise matrix is identified using the innovations sequence. This CubeSat is a case in which there is no *a priori* information about the system, such as sensors noise statistics and measured inertia tensor, which was computed using CAD software. Therefore, the aforementioned adaptive procedure is an solution to the covariance matrix tuning problem.

For future works, there is the analysis of the optimal length of the sliding window in the covariance matching algorithm. Another topic is the study of disturbance or fault detection methods, such as the ξ^2 hypothesis test, so the adaptation will be executed only in specific scenarios. Also, there is the opportunity to investigate the joint of the covariance matching adaptation along with machine learning algorithms for sensor fault detection and isolation.

REFERENCES

ALKEN, P.; THÉBAULT, E.; BEGGAN, C. D.; AMIT, H.; AUBERT, J.; BAERENZUNG, J.; BONDAR, T. N.; BROWN, W. J.; CALIFF, S.; CHAMBODUT, A.; CHULLIAT, A.; COX, G. A.; FINLAY, C. C.; FOURNIER, A.; GILLET, N.; GRAYVER, A.; HAMMER, M. D.; HOLSCHNEIDER, M.; HUDER, L.; HULOT, G.; JAGER, T.; KLOSS, C.; KORTE, M.; KUANG, W.; KUVSHINOV, A.; LANGLAIS, B.; LÉGER, J.-M.; LESUR, V.; LIVERMORE, P. W.; LOWES, F. J.; MACMILLAN, S.; MAGNES, W.; MANDEA, M.; MARSAL, S.; MATZKA, J.; METMAN, M. C.; MINAMI, T.; MORSCHHAUSER, A.; MOUND, J. E.; NAIR, M.; NAKANO, S.; OLSEN, N.; PAVÓN-CARRASCO, F. J.; PETROV, V. G.; ROPP, G.; ROTHER, M.; SABAKA, T. J.; SANCHEZ, S.; SATURNINO, D.; SCHNEPF, N. R.; SHEN, X.; STOLLE, C.; TANGBORN, A.; TØFFNER-CLAUSEN, L.; TOH, H.; TORTA, J. M.; VARNER, J.; VERVELIDOU, F.; VIGNERON, P.; WARDINSKI, I.; WICHT, J.; WOODS, A.; YANG, Y.; ZEREN, Z.; ZHOU, B. International geomagnetic reference field: the thirteenth generation. *Earth, Planets and Space*, Springer Science and Business Media LLC, v. 73, n. 1, feb 2021. 21, 22

ASUNDI, S.; FITZ-COY, N.; LATCHMAN, H. Evaluation of Murrell's EKF-based attitude estimation algorithm for exploiting multiple attitude sensor configurations. *Sensors*, MDPI AG, v. 21, n. 19, p. 6450, sep 2021. 30

BAR-SHALOM, Y.; LI, X.-R.; KIRUBARAJAN, T. *Estimation with Applications to Tracking and Navigation*. [S.l.]: Wiley, 2002. 33, 35, 37, 53

BARONI, L. Kalman filter for attitude determination of a CubeSat using low-cost sensors. *Computational and Applied Mathematics*, Springer Science and Business Media LLC, v. 37, n. S1, p. 72–83, aug 2017. 31

BATTISTINI, S.; CAPPELLETTI, C.; GRAZIANI, F. Results of the attitude reconstruction for the unisat-6 microsatellite using in-orbit data. *Acta Astronautica*, v. 127, p. 87–94, 2016. ISSN 0094-5765. Disponível em: <https://www.sciencedirect.com/science/article/pii/S0094576516300017>. 5, 46

BHANDERI, D. Modeling Earth albedo currents on sun sensors for improved vector observation. In: . [S.l.]: American Institute of Aeronautics and Astronautics, 2006. ISBN 978-1-62410-046-8. 26

BHANDERI, D.; BAK, T. Modeling Earth albedo for satellites in earth orbit. In: . [S.l.]: American Institute of Aeronautics and Astronautics, 2005. ISBN 978-1-62410-056-7. 25, 26

BORGES, R. A.; SANTOS, A. C. dos; SILVA, W. R.; AGUAYO, L.; BORGES, G. A.; KARAM, M. M.; SOUSA, R. B. de; GARCíA, B. F.-A.; BOTELHO, V. M. de S.; FERNáNDEZ-CARRILLO, J. M.; AGRA, J. M. L.; AGELET, F. A.; BORGES, J. V. Q. S.; OLIVEIRA, A. C. A. de; MELLO, B. T. de; AVELINO, Y. da C. F.; MODESTO, V. F.; BRENAG, E. C. The AlfaCrux CubeSat mission description and early results. *Applied Sciences*, v. 12, p. 9764, 9 2022. ISSN 2076-3417. 3, 7, 61, 82

BRENAG, E. C.; ARRUDA, M. L.; MELLO, B. T. de; BORGES, R. A.; OVCHINNIKOV, M.; IVANOV, D. AlfaCrux CubeSat magnetic dipole determination and attitude motion estimation using magnetometer measurements only. In: *Proceedings of the 74th International Astronautical Congress*. [S.l.]: International Astronautical Federation (IAF), 2023. 8, 83, 84

BRENAG, E. C.; MELLO, B. T. de; ARRUDA, M. L.; BORGES, R. A.; IVANOV, D.; MONAKHOVA, U.; MASHTAKOV, Y.; OVCHINNIKOV, M. Magnetic parameters estimation and attitude motion reconstruction using in-flight magnetometer measurements of the AlfaCrux CubeSat. In: *Proceedings of the Joint 5th IAA Latin American CubeSat Workshop and 3rd IAA Latin American Symposium on Small Satellites*. [S.l.]: International Academy of Astronautics, 2022. 7, 83, 84, 89

CHAGAS, R. A. J.; MARQUES, W. J. de S.; CARVALHO, T. A. M. de; OLIVEIRA, P. A. da S.; HOTT, G. M. C. A self-calibration algorithm for satellite sensors based on vector observations. *Aerospace Science and Technology*, Elsevier BV, v. 114, p. 106759, jul 2021. 5

CHENG, Y.; CRASSIDIS, J. Particle filtering for sequential spacecraft attitude estimation. In: . [S.l.]: American Institute of Aeronautics and Astronautics, 2004. ISBN 978-1-62410-073-4. 5

CHIELLA, A. C. B.; TEIXEIRA, B. O. S.; PEREIRA, G. A. S. Quaternion-based robust attitude estimation using an adaptive unscented Kalman filter. *Sensors*, MDPI AG, v. 19, n. 10, p. 2372, may 2019. 6, 51, 52

CILDEN-GULER, D.; RAITOHARJU, M.; PICHE, R.; HAJIYEV, C. Nanosatellite attitude estimation using Kalman-type filters with non-gaussian noise. *Aerospace Science and Technology*, Elsevier BV, v. 92, p. 66–76, sep 2019. 6

CILDEN-GULER, D.; SCHAUB, H.; HAJIYEV, C.; KAYMAZ, Z. Attitude estimation with albedo interference on sun sensor measurements. *Journal of Spacecraft and Rockets*, American Institute of Aeronautics and Astronautics (AIAA), v. 58, n. 1, p. 148–163, jan 2021. 25

CRASSIDIS, J. L.; JUNKINS, J. L. *Optimal Estimation of Dynamic Systems*. 2. ed. [S.l.]: Chapman and Hall/CRC, 2012. ISBN 9780429105609. 34, 37, 38

CRASSIDIS, J. L.; MARKLEY, F. L. Unscented filtering for spacecraft attitude estimation. *Journal of Guidance, Control, and Dynamics*, v. 26, p. 536–542, 7 2003. ISSN 0731-5090. 15, 45

CRASSIDIS, J. L.; MARKLEY, F. L.; CHENG, Y. Survey of nonlinear attitude estimation methods. *Journal of Guidance, Control, and Dynamics*, v. 30, p. 12–28, 1 2007. ISSN 0731-5090. 4, 14, 31

DUNÍK, J.; STRAKA, O.; KOST, O.; HAVLÍK, J. Noise covariance matrices in state-space models: A survey and comparison of estimation methods-part i. *International Journal of Adaptive Control and Signal Processing*, Wiley, v. 31, n. 11, p. 1505–1543, may 2017. 51, 52

ESIT, M.; YAKUPOGLU, S.; SOKEN, H. E. Attitude filtering for nanosatellites: A comparison of different approaches under model uncertainties. *Advances in Space Research*, Elsevier BV, v. 68, n. 6, p. 2551–2564, sep 2021. 4

FARRENKOPF, R. L. Analytic steady-state accuracy solutions for two common spacecraft attitude estimators. *Journal of Guidance, Control, and Dynamics*, American Institute of Aeronautics and Astronautics (AIAA), v. 1, n. 4, p. 282–284, jul 1978. 39, 42

GAO, Z.; CECATI, C.; DING, S. X. A survey of fault diagnosis and fault-tolerant techniques—part i: Fault diagnosis with model-based and signal-based approaches. *IEEE Transactions on Industrial Electronics*, Institute of Electrical and Electronics Engineers (IEEE), v. 62, n. 6, p. 3757–3767, jun 2015. 51, 52

GARCIA, R.; PARDAL, P.; KUGA, H.; ZANARDI, M. Nonlinear filtering for sequential spacecraft attitude estimation with real data: Cubature Kalman filter, unscented Kalman filter and extended Kalman filter. *Advances in Space Research*, Elsevier BV, v. 63, n. 2, p. 1038–1050, jan 2019. 5

GUIMARãES, F. C.; SILVA, R. C. da; LOIOLA, J. V. L. de; BORGES, G. A.; BORGES, R. A.; BATTISTINI, S.; CAPPELLETTI, C. Aplicação do filtro de Kalman para a determinação de atitude de plataforma de testes de pequenos satélites. In: SBA. *Proceedings of the XIII Simpósio Brasileiro de Automação Inteligente*. [S.l.]: Sociedade Brasileira de Automática, 2017. 5

HAJIYEV, C.; SOKEN, H. E. *Fault Tolerant Attitude Estimation for Small Satellites*. [S.l.]: CRC Press, 2020. ISBN 9781351248839. 6, 20, 28, 29, 30, 52, 54, 56, 57, 58, 59, 81

HAJIYEV, C.; SOKEN, H. E.; CILDEN-GULER, D. Nontraditional attitude filtering with simultaneous process and measurement covariance adaptation. *Journal of Aerospace Engineering*, American Society of Civil Engineers (ASCE), v. 32, n. 5, sep 2019. 6

HOOTS, F. R.; ROEHRICH, R. L. *Spacetrack Report #3: Models for Propagation of NORAD Element Sets*. U.S. Air Force Aerospace Defense Command. Office of Astrodynamics, 1980. Peterson AFB, Colorado Springs, CO. 21

IVANOV, D.; OVCHINNIKOV, M.; IVLEV, N.; KARPENKO, S. Analytical study of microsatellite attitude determination algorithms. *Acta Astronautica*, Elsevier BV, v. 116, p. 339–348, nov 2015. 4

IVANOV, D.; OVCHINNIKOV, M.; PENKOV, V.; ROLDUGIN, D.; DORONIN, D.; OVCHINNIKOV, A. Advanced numerical study of the three-axis magnetic attitude control and determination with uncertainties. *Acta Astronautica*, Elsevier BV, v. 132, p. 103–110, mar 2017. 86, 87

IVANOV, D.; OVCHINNIKOV, M.; ROLDUGIN, D. Three-axis attitude determination using magnetorquers. *Journal of Guidance, Control, and Dynamics*, American Institute of Aeronautics and Astronautics (AIAA), v. 41, n. 11, p. 2455–2462, nov 2018. 19

IVANOV, D.; ROLDUGIN, D.; TKACHEV, S.; OVCHINNIKOV, M.; ZHARKIKH, R.; KUDRYAVTSEV, A.; BYCHEK, M. Attitude motion and sensor bias estimation onboard the SiriusSat-1 nanosatellite using magnetometer only. *Acta Astronautica*, v. 188, p. 295–307, 11 2021. ISSN 00945765. 5, 83, 86

JULIER, S. J.; UHLMANN, J. K. New extension of the Kalman filter to nonlinear systems. In: KADAR, I. (Ed.). [S.l.]: SPIE, 1997. v. 3068, p. 182. 44, 45

KAILATH, T. An innovations approach to least-squares estimation–part i: Linear filtering in additive white noise. *IEEE Transactions on Automatic Control*, Institute of Electrical and Electronics Engineers (IEEE), v. 13, n. 6, p. 646–655, dec 1968. 53

KALMAN, R. E. A new approach to linear filtering and prediction problems. *Journal of Basic Engineering*, ASME International, v. 82, n. 1, p. 35–45, mar 1960. 34, 36

KONTAXOGLOU, A.; TSUTSUMI, S.; KHAN, S.; NAKASUKA, S. Towards a digital twin enabled multifidelity framework for small satellites. In: *PHM Society European Conference*. [S.l.]: PHM Society, 2021. (Proceedings of the European Conference of the PHM Society 2021, 1), p. 211–220. 82

LEFEBVRE, T.; BRUYNINCKX, H.; SCHULLER, J. D. Comment on "a new method for the nonlinear transformation of means and covariances in filters and estimators"[with authors' reply]. *IEEE Transactions on Automatic Control*, Institute of Electrical and Electronics Engineers (IEEE), v. 47, n. 8, p. 1406–1409, aug 2002. 58

LEFFERTS, E.; MARKLEY, F.; SHUSTER, M. Kalman filtering for spacecraft attitude estimation. *Journal of Guidance, Control, and Dynamics*, American Institute of Aeronautics and Astronautics (AIAA), v. 5, n. 5, p. 417–429, sep 1982. 37, 39

MARKLEY, F. L. Attitude error representations for Kalman filtering. *Journal of Guidance, Control, and Dynamics*, American Institute of Aeronautics and Astronautics (AIAA), v. 26, n. 2, p. 311–317, mar 2003. 39, 46, 47

MARKLEY, F. L.; CRASSIDIS, J.; CHENG, Y. Nonlinear attitude filtering methods. In: . [S.l.]: American Institute of Aeronautics and Astronautics, 2005. ISBN 978-1-62410-056-7. 39

MARKLEY, F. L.; CRASSIDIS, J. L. *Fundamentals of Spacecraft Attitude Determination and Control*. [S.l.]: Springer New York, 2014. ISBN 978-1-4939-0801-1. 4, 9, 11, 12, 13, 14, 15, 16, 17, 18, 19, 20, 27, 28, 29, 30, 40, 41, 42, 62

MARKLEY, F. L.; REYNOLDS, R. G. Analytic steady-state accuracy of a spacecraft attitude estimator. *Journal of Guidance, Control, and Dynamics*, American Institute of Aeronautics and Astronautics (AIAA), v. 23, n. 6, p. 1065–1067, nov 2000. 42

MAYBECK, P. S. *Stochastic models, estimation and control*. [S.l.]: Academic Press, 1979. ISBN 0124807011. 50, 55

MEEUS, J. H. *Astronomical algorithms*. [S.l.]: Willmann-Bell, 1991. 429 p. ISBN 0943396352. 21, 24

MEHRA, R. On the identification of variances and adaptive Kalman filtering. *IEEE Transactions on Automatic Control*, Institute of Electrical and Electronics Engineers (IEEE), v. 15, n. 2, p. 175–184, apr 1970. 52, 53

MEHRA, R. Approaches to adaptive filtering. *IEEE Transactions on Automatic Control*, Institute of Electrical and Electronics Engineers (IEEE), v. 17, n. 5, p. 693–698, oct 1972. 50, 52, 55

MELLO, B. T. de; BORGES, R. A.; BATTISTINI, S. Attitude reconstruction of the AlfaCrux CubeSat using onboard sensors and solar panels in-orbit data. In: *Proceedings of the Joint 5th IAA Latin American CubeSat Workshop and 3rd IAA Latin American Symposium on Small Satellites*. [S.l.]: International Adademy of Astronautics, 2022. 7, 83, 84

MESQUITA, B. D. R. de; KUGA, H. K.; CARRARA, V. Estimation and attitude control in CONASAT's nominal operation mode: An approach for SDRE filter and PID control. *IEEE Latin America Transactions*, Institute of Electrical and Electronics Engineers (IEEE), v. 15, n. 5, p. 835–842, may 2017. 5

MOHAMED, A. H.; SCHWARZ, K. P. Adaptive Kalman filtering for INS/GPS. *Journal of Geodesy*, Springer Science and Business Media LLC, v. 73, n. 4, p. 193–203, may 1999. 55, 56, 57, 58, 59, 88

MYERS, K.; TAPLEY, B. Adaptive sequential estimation with unknown noise statistics. *IEEE Transactions on Automatic Control*, Institute of Electrical and Electronics Engineers (IEEE), v. 21, n. 4, p. 520–523, aug 1976. 50, 52

NARASIMHAPPA, M.; MAHINDRAKAR, A. D.; GUIZILINI, V. C.; TERRA, M. H.; SABAT, S. L. MEMS-based IMU drift minimization: Sage Husa adaptive robust Kalman filtering. *IEEE Sensors Journal*, Institute of Electrical and Electronics Engineers (IEEE), v. 20, n. 1, p. 250–260, jan 2020. 6, 50, 51

OVCHINNIKOV, M.; IVANOV, D. Approach to study satellite attitude determination algorithms. *Acta Astronautica*, Elsevier BV, v. 98, p. 133–137, may 2014. 4

SAGE, A. P.; HUSA, G. W. Adaptive filtering with unknown prior statistics. *Proceedings of Joint Automatic Control Conference*, p. 760–769, 1969. 50, 52

SCHAUB, H.; JUNKINS, J. L. Stereographic orientation parameters for attitude dynamics: A generalization of the Rodrigues parameters. *Journal of the Astronautical Sciences*, v. 44, n. 1, p. 1–19, 1996. 14

SHUSTER, M. D. Kalman filtering of spacecraft attitude and the QUEST model. *Journal of the Astronautical Sciences*, v. 38, n. 3, p. 377–393, set. 1990. 31

SHUSTER, M. D. Survey of attitude representations. *Journal of the Astronautical Sciences*, v. 41, n. 4, p. 439–517, out. 1993. Disponível em: <https://ui.adsabs.harvard.edu/abs/1993JAnSc..41..439S>. 13, 14, 15

SILVA, W.; GARCIA, R.; SANTILLI, G.; KUGA, H.; ZANARDI, M.; PARDAL, P. Rao-Blackwellized particle filter for the CBERS-4 attitude and gyros bias estimation. *Acta Astronautica*, Elsevier BV, v. 193, p. 679–690, apr 2022. 5

SOKEN, H. E.; HACIZADE, C. Tuning the attitude filter: A comparison of intuitive and adaptive approaches. In: *2019 9th International Conference on Recent Advances in Space Technologies (RAST)*. [S.l.]: IEEE, 2019. 4, 50

SOKEN, H. E.; HAJIYEV, C. REKF and RUKF for pico satellite attitude estimation in the presence of measurement faults. *Journal of Systems Engineering and Electronics*, Institute of Electrical and Electronics Engineers (IEEE), v. 25, n. 2, p. 288–297, apr 2014. 6

SOKEN, H. E.; SAKAI, S. ichiro. Adaptive tuning of the unscented Kalman filter for satellite attitude estimation. *Journal of Aerospace Engineering*, American Society of Civil Engineers (ASCE), v. 28, n. 3, may 2015. 6

SOKEN, H. E.; SAKAI, S. ichiro. Attitude estimation and magnetometer calibration using reconfigurable TRIAD+filtering approach. *Aerospace Science and Technology*, Elsevier BV, v. 99, p. 105754, apr 2020. 5

STORN, R.; PRICE, K. Differential evolution – a simple and efficient heuristic for global optimization over continuous spaces. *Journal of Global Optimization*, Springer Science and Business Media LLC, v. 11, n. 4, p. 341–359, 1997. 84

URBAN, S. E.; SEIDELMANN, P. K. *Explanatory supplement to the Astronomical almanac.* [S.l.]: University Science Books, 2013. 676 p. ISBN 9781891389856. 24

VALLADO, D.; CRAWFORD, P.; HUJSAK, R.; KELSO, T. Revisiting spacetrack report #3. In: *AIAA/AAS Astrodynamics Specialist Conference and Exhibit.* [S.l.]: American Institute of Aeronautics and Astronautics, 2006. 21

VALLADO, D. A.; WERTZ, J. *Fundamentals of Astrodynamics and Applications.* 4th. ed. [S.l.]: Microcosm Press, 2013. 1106 p. (Space technology library). ISBN 9781881883180. 9, 10, 11, 21, 24, 25

WERTZ, J. R. (Ed.). *Spacecraft Attitude Determination and Control.* [S.l.]: Springer Netherlands, 1978. 17, 22, 23

WESTON, S.; YOST, B. *State-of-the-Art: Small Spacecraft Technology.* NASA Small Spacecraft Systems Virtual Institute and Ames Research Center, 2023. NASA/TP—20220018058. 1, 4